2015

Nano-Scale Investigation of Mechanical Characteristics of Main Phases of Hydrated Cement Paste

Shahin Hajilar
shajilar@engin.umass.edu

NANO-SCALE INVESTIGATION OF MECHANICAL CHARACTERISTICS OF MAIN PHASES OF HYDRATED CEMENT PASTE

A Thesis Presented

by

SHAHIN HAJILAR

Submitted to the Graduate School of the

University of Massachusetts Amherst in partial fulfillment

of the requirements for the

MASTER OF SCIENCE IN CIVIL ENGINEERING

February 2015

Civil and Environmental Engineering

Structural Engineering and Mechanics

NANO-SCALE INVESTIGATION OF MECHANICAL CHARACTERISTICS OF MAIN PHASES OF HYDRATED CEMENT PASTE

A Thesis Presented

by

SHAHIN HAJILAR

Approved as to style and content by:

_____
Behrouz Shafei, Chair

_____
Alice Alipour, Member

_____
David M. Ford, Member

_____
Richard N. Palmer, Department Head
Civil and Environmental Engineering

ACKNOWLEDGMENTS

I would like to thank all those who have helped me along the way to finishing this Master's degree program. Including everyone would require several pages of text, so a summary will have to do.

First and foremost, I would like to thank my advisor, Dr. Behrouz Shafei, who always gave me useful suggestions and orientation, and always encouraged me to challenge the deeper exploration throughout my research project at University of Massachusetts Amherst. Additionally, the perspective and commentary provided by my thesis committee members, Dr. Alice Alipour and Dr. David M. Ford, are gratefully acknowledged.

I would like to thank my parents and siblings for their endless support that was crucial to my success. Knowing that they are proud of my academic accomplishments is one of my biggest inspirations.

I would be remiss if I did not give a big thank to the graduate students with whom I worked on a daily basis: Dena, Ameh, Rose, Mark, Alex, Omer and David. The time here was accentuated by my relationships with each of you.

Lastly, special thanks go to all my instructors and all staff (Jodi Ozdarski, Kelly Ives, Jennifer Pease, and others) in the Department of Civil and Environmental Engineering of University of Massachusetts Amherst.

ABSTRACT

NANO-SCALE INVESTIGATION OF MECHANICAL CHARACTERISTICS OF MAIN PHASES OF HYDRATED CEMENT PASTE

FEBRUARY 2015

SHAHIN HAJILAR, B.S., UNIVERSITY OF TEHRAN

M.S.C.E., UNIVERSITY OF MASSACHUSETTS AMHERST

Directed by: Behrouz Shafei

Hydrated cement paste (HCP), which is present in various cement-based materials, includes a number of constituents with distinct nano-structures. To understand the mechanical characteristics of the HCP at the nano-scale, a comprehensive set of crystalline structures that represent the main HCP constituents is developed for Molecular Dynamics (MD) simulations. The elastic properties of the HCP phases are calculated using the static methods. The accuracy of estimated values is verified by comparing them with the results from experimental tests and other atomistic simulation methods. The outcome of MD simulations is extended to predict the elastic properties of the C-S-H gel by rescaling the values calculated for the individual crystalline structures. To take into account the contribution of porosity, a detailed microporomechanics study is conducted on low- and high-density types of C-S-H. The obtained results indicate that MD simulations are capable of capturing the elastic properties of the C-S-H gel. This is further verified by comparing the rescaled values with the predictions from nanoindentation tests.

To investigate the mechanical strength and performance of the HCP under external loads, the atomic structures of the main HCP crystals are generated at the nano-scale in the current study. Through an extensive set of MD simulations, the mechanical behavior of the HCP crystals is examined under uniaxial tensile strains. From the stress-strain curves obtained in the three

orthogonal directions, elastic and plastic responses of the HCP crystals are determined. A comprehensive chemical bond and structural damage analysis is also performed to characterize the failure mechanisms of the HCP crystals under high tensile strains. The outcome of this study provides detailed information about the nonlinear behavior, plastic deformation, and structural failure of the HCP phases and similar atomic structures.

TABLE OF CONTENTS

LIST OF TABLES

LIST OF FIGURES

CHAPTER 1

INTRODUCTION

1.1 Objectives

Cement-based materials, such as mortar and concrete, are widely used in the construction of civil infrastructure components. This is mainly due to the availability of raw materials, fire resistance, cost advantages, and ease of being formed into a variety of shapes and sizes. Among the cement-based materials, concrete is the most common construction material throughout the world. As of 2006, the annual production of concrete was estimated about 7.5 billion cubic meters, more than one cubic meter for every person who lives on Earth [1]. Because of the significant usage of concrete, any important findings on the structure and properties of this material may result in major improvements to the environment and human life.

Concrete is a composite material, which consists of water, fine and coarse aggregates, and a binder called cement. Cement is the most important constituent of concrete which reacts with water to form a binding material known as hydrated cement paste (HCP). The U.S. annual consumption of cement in 2013 reached about 80 million metric tons while it is anticipated to hit 183 million metric tons in 2030 reflecting 43% increase compared to the past peak level in 2005 [2]. This indicates that the need to cement products will constantly increase in the coming years. What exacerbates the situation is the major contribution of cement industry in the global greenhouse effect. Since cement is produced at high temperature (up to 2700 ˚F), cement manufacturing leads to high carbon dioxide (CO_2) emission. This is why cement industry is known as one of the most prominent contributors to the global warming by producing 5-10% of global man-made CO_2 emissions. While according to the Portland Cement Association (PCA) forecast [2], the use of cement in civil constructions will be tremendously growing in future,

increasing the service life of concrete structures can be recognized as a solution to address the CO_2 emissions problem.

It is known that the service life of concrete structures can be enhanced by improving the strength and durability of concrete which highly depend on the binding properties of cement. This can be justified by taking into account the fact that the HCP is not as strong as aggregates in terms of variety of mechanical performance measures. A number of research efforts have been conducted to understand the main properties of cementitious materials. These efforts include both experimental and numerical studies, most of which have been carried out at the macro-scale to improve the serviceability and performance of concrete structures. Despite the wealth of knowledge currently available, there is still a gap in the literature concerning the main properties of the HCP as the most important component of cement-based materials. Considering the fact that hydrated cement binds the aggregates together and directly contributes to the structural characteristics of concrete as a composite material, an in-depth study of the HCP phases in smaller scales (i.e., micro- and nano-scale) provides invaluable information about the key mechanical properties of concrete and identifies appropriate methods to improve them. Therefore, the main objective of this study is to characterize the mechanical properties of the HCP in both elastic and plastic regimes.

Elastic behavior is an important aspect of any engineering design. Structures from airplane, bridges, and buildings to microelectronic components are typically designed for elastic deformation. On the other hand, plastic behavior is also important to be evaluated as it provides invaluable information about the onset of permanent deformation and material failure. This thesis is dedicated to characterize the mechanical behavior of the HCP phases under external loads. The outcome of this research will help increase the performance of concrete structures which results in a significant reduction in the use of cement. If engineers can reduce CO_2 emissions by only 10%, one-fifth of the Kyoto Protocol goal of 5.2% reduction in CO_2 emissions can be achieved.

1.2 Hydrated Cement Paste (HCP)

The HCP is formed as a rigid phase following the chemical reactions between the Portland cement and water. This phase is found to be a highly complex composite made of several crystals, each of which contributes to the mechanical strength and performance of concrete. The cement paste hydration products can be categorized into four major groups: i) calcium silicate hydrates (C-S-H), ii) calcium hydroxide (portlandite), iii) calcium aluminate monosulphate hydrates (AFm), and iv) calcium aluminate trisulphate hydrates (AFt). According to Mehta and Manmohan [3], the C-S-H constitutes 50-60% of the total volume of the solid HCP. This percentage changes to 20-25% for the portlandite and 15-20% for the AFm and AFt combined. Among the hydration products, the C-S-H has an amorphous nanostructure, which is difficult to be characterized. There are, however, few crystals that can mimic the structure of the C-S-H. Tobermorite 9, 11, and 14 Å as well as jennite are the crystals frequently used in the literature to investigate the structural and mechanical properties of the C-S-H. On the other hand, ettringite and monosulphoaluminate have been identified as the most common phases of the AFt and AFm structures, respectively.

1.3 Need for Atomistic Simulation

The classical theories of continuum mechanics have been the basis for most computational tools of engineering. In the continuum mechanics, the basic assumption is that matter can be divided indefinitely without a change of material property. Since many of engineering problems cannot be solved analytically, several numerical methods, such as finite element method (FEM), finite volume method (FVM) and finite difference method (FDM) have been established based on the theories of continuum mechanics to solve the governing partial differential equations numerically. In these methods, the domain is discretized into integration points and it is expected that increasing the number of integration points would result in more

accurate solution of the problem. These methods have been widely used to solve various engineering problems at macro-scale.

Over the last decades, however, it was realized that the study of the nano-scale (or atomistic) behavior is essential to understand how various materials fail under external loads. Considering elastic deformation and fracture for example, many disciplines in this area is linked with a notion of "chemical bond" which implies the significance of understanding atomistic processes to describe deformation and failure of materials. Contrary to continuum problems, no spatial discretization is required in atomistic modeling as each atom is considered to be an individual particle, which cannot be further divided. Since atomistic models contain extremely large number of particles, they normally cannot be solved analytically. Therefore, numerical simulation is performed to model the motion of each atom over the simulation time span. This is called atomistic simulation, in which a step-by-step integration is carried out numerically to progress the simulation time. The collective behavior of atoms reveals how material undergoes deformation. Atomistic simulation is capable of solving the dynamical evolution of both equilibrium and non-equilibrium processes.

1.4 Outline

Chapter 2 focuses on the formation and structure of the main constituents of the HCP. For each individual HCP phase, one/several crystal(s) that reasonably represents the chemical and physical properties of the corresponding phase is introduced. This study examines a complete range of crystalline structures present in the HCP, including portlandite, tobermorite 9, 11, 14 Å, jennite, ettringite, kuzelite, and hydrogarnet. This chapter provides the initial models for the MD simulations.

Chapter 3 discusses atomistic simulation methods with a special focus on the MD method. The MD method is known as one of the most powerful atomistic simulation method, through which the equilibrium thermodynamic properties of a system are calculated by tracking the atoms that exist in the system during a certain period of time. In this research, a detailed study is presented on how the capabilities of MD simulations can be used to determine the elastic properties of the main constituents of the HCP.

Chapter 4 describes how to characterize the elastic properties of HCP crystals. In this chapter, using a thermodynamical view of physical process of elastic deformation, the stress-strain relationship at the nano-scale is obtained. The mechanical properties (i.e., bulk, shear and Young's modulus, and Poisson's ratio) of the HCP crystals are calculated from the stress-strain relationships. To evaluate the precision of simulations, the MD results are compared with an extensive set of experimental and simulation data published in the literature for each of the HCP phases. While this study captures the elastic properties of all the C-S-H components at the nano-scale, a major difference is observed between the values obtained for the individual C-S-H components compared to the ones suggested for the whole C-S-H gel. This difference can be understood by considering the intrinsic nano-porosity present in the C-S-H gel. Hence, a separate microporomechanical study is performed to relate the corresponding elastic properties. This is achieved by utilizing the Self-Consistent (SC) and Mori-Tanaka (MT) homogenization models, which take into account the contribution of both solid phase and pore structure of the C-S-H. The accuracy of estimates is verified by the data obtained directly from the nanoindentation experiments conducted on the C-S-H gel.

Chapter 5 presents the research on characterizing the mechanical response of the HCP phases under external loads using MD simulations. The crystalline structures of tobermorite 9, 11 and 14 Å, jennite, hydrogarnet, ettringite, and kuzelite are constructed at the atomic scale. Subsequently, uniaxial tensile strains are applied in the x, y and z directions of the simulation cells

and the stress-strain data are recorded. From the stress-strain curves, the mechanical properties of the HCP crystalline structures are fully characterized. A comprehensive bond analysis is performed to find the correlation between the chemical bond stretching and the stress-strain curves. A separate structural damage analysis is also conducted to investigate the damaged molecular structure of the HCP crystals in the direction of straining. The failure mechanism for each crystalline structure elongated in the three orthogonal directions is identified and discussed in detail. This study provides an in-depth understanding of the mechanical behavior of the HCP crystals, which are recognized as the basic building blocks of ordinary cement paste. It is expected that the presented results directly contribute to designing a new generation of cements with improved strength and stiffness properties.

Finally, the work presented in the previous chapters is concluded and the future research directions related to this study are discussed. The outcome of this research provides reliable atomistic models, which are critical to investigate the mechanical behavior of the major constituents of cement-based materials at different scales.

CHAPTER 2

CONSTITUENTS OF HYDRATED CEMENT PASTE

In cement chemistry, the term “hydration” refers to the numerous chemical reactions, physical changes, and thermodynamical processes that take place when cement powder is mixed with water. The cement powder typically contains a wide range of components, each of which has different impurities and reaction rates. Concerning Portland cement for example, these components include tricalcium silicate (C_3S), dicalcium silicate (C_3S), tricalcium aluminate (C_3A), and aluminoferrite (C_4AF). In cement-based materials, the cement components get involved in different chemical reactions during the hydration process and as a result, various HCP products are formed. The structure of the HCP contains the hydration products that coexist with unhydrated cement components, which may persist after the hydration. Below is a brief overview of the hydration reactions of the cement components.

2.1 Hydration Reactions of the Cement Components

Although from a technical point of view it may appear to be simple when a certain portion of Portland cement is mixed with given water amount, the hydration process has still not been fully understood [4, 5, 6, 7]. The primary reason for this situation is that the hydration reactions are affected by many factors, including the composition of the cement powder, water to cement ratio (w/c), degree of hydration, and curing temperature. However, in order to reduce the large number of variables associated with the hydration processes, the hydration of cement is frequently studied separately for each component of cement powder.

2.1.1 Tricalcium Silicate (Alite)

Alite (C_3S) is the main component of Portland cement, which constitutes 70% of the total weight. Furthermore, the hydration of alite is the main cause of setting and development of early strength. Alite reacts very fast with water due to the high Ca content and the presence of an oxide ion in its lattice. While the total hydration process of alite may take up to 1 year, about 70% of it reacts in 28 days. The hydration reaction of alite can be written as:

$$2C_3S + 6H \rightarrow C_3S_2H_3 + 3CH \tag{2.1}$$

where C, S, and H represent calcium oxide (CaO), silicon dioxide (SiO_2), and water (H_2O), respectively. The products of the alite's hydration, i.e., C-S-H gel and CH (also known as portlandite), are the core components of the HCP and the main contributors to its mechanical properties. It should be noted that the stoichiometry of the C-S-H gel is not fixed and the $C_3S_2H_3$ is one of the possible products generated during the hydration reactions of alite.

2.1.2 Dicalcium Silicate (Belite)

Belite (C_2S) is the second important component present in Portland cement. Compared to alite, it has a lower reactivity and, therefore, contributes in supplementary strength. The hydration reaction of belite is comparable to that of alite in terms of final products, i.e., C-S-H gel and portlandite. The only difference is that less portlandite is formed.

$$2C_2S + 4H \rightarrow C_3S_2H_3 + CH \tag{2.2}$$

The above reaction is so slow that only 30% of belite reacts with water in 28 days and the reaction will be incomplete even after a year [8].

2.1.3 Tricalcium Aluminate (Celite)

Celite (C_3A) is the third significant component of Portland cement. The reaction of celite with water, known as flash setting is very fast, during which a large amount of heat is released causing the paste to set within few minutes after mixing. The flash setting is not desired as it affects the rheology of the paste at early ages, reduces the workability of the paste, and prevents the homogeneity of the mix. Celite reacts with water according to the reaction below:

$$C_3A + 21H \rightarrow C_4AH_{19} + C_2AH_8 \rightarrow 2C_3AH_6 + 15H \tag{2.3}$$

where A is aluminum oxide (Al_2O_3). The first products are unstable calcium hydroaluminates which rapidly evolves to hydrogarnet (C_3AH_6) [9]. To prevent flash setting, retardants such as gypsum ($C\bar{S}H_2$) are added to Portland cement. Gypsum is highly soluble and releases calcium and sulfate ions into the pore solution. The presence of sulfate ions causes celite to undergo the following reaction which produces mineral ettringite ($C_6A\bar{S}_3H_{32}$).

$$C_3A + 3C\bar{S}H_2 + 26H \rightarrow C_6A\bar{S}_3H_{32} \tag{2.4}$$

where $\bar{S}$ is sulfur trioxide (SO_3). Since nowadays all Portland cements contain gypsum, Equation 2.4 is the governing hydration reaction for celite. However, small amounts of hydrogarnet, which is the main product in Equation 2.3, can often be found in cement paste. If gypsum is completely consumed before Celite, the concentration of sulfate ions decreases drastically, Celite starts consuming ettringite, and different solid phases with fewer sulfates are formed. As a result of such reactions, monosulphoaluminate ($C_4A\bar{S}H_{12}$) is produced as:

$$2C_3A + C_6A\bar{S}_3H_{32} + 4H \rightarrow 3C_4A\bar{S}H_{12} \tag{2.5}$$

2.1.4 Aluminoferrite (Ferrite)

The aluminoferrite phase (C_4AF) is formed when aluminum atoms enter to the structure of C_2F which is frequently called ferrite in cement chemistry. The hydration of ferrite is very similar but slower than that of celite. The only difference is that some of the aluminum atoms in the reaction products are substituted by iron atoms.

$$C_4AF + 3.C\bar{S}H_2 + 21.H \rightarrow C_6(A,F)\bar{S}_3H_{32} + (F,A)H_3 \quad (2.6)$$

$$C_4AF + C_6(A,F)\bar{S}_3H_{32} + 7.H \rightarrow 3.C_4(A,F)\bar{S}H_{12} + (F,A)H_3 \quad (2.7)$$

where F is iron (III) oxide (Fe_2O_3), (A, F) refers to aluminum with variable substitution of iron and (F, A) indicates iron with variable substitution of aluminum. The $(F,A)H_3$ is an amorphous phase formed in small amounts. The other hydration products are ettringite and monosulphoaluminate with a partial substitution of aluminum by iron. In cement chemistry these phases are often called AFt and AFm phases, respectively, where the "t" stands for trisulphate, and the "m" refers to monosulphate.

2.1.5 Sulfate Attack

As discussed above, most Portland cements do not contain enough sulfate-rich sources (e.g., gypsum) to fully hydrate celite and ferrite via reactions 2.4 and 2.6 to form ettringite. Once gypsum content is depleted, ettringite becomes unstable and starts reacting with the remaining celite and ferrite to form monosulphoaluminate. Therefore, in mature HCP, it is common to find little or no ettringite. However, if a new source of sulfate ions become available (from ground water, sea water, or soil); it will be thermodynamically favorable to form ettringite again, just as it was initially, through the consumption of the existing monosulphoaluminate. This reaction can be represented as follows:

$$C_4A\bar{S}H_{12} + 2C\bar{S}H_2 + 16H \rightarrow C_6A\bar{S}_3H_{32} \quad (2.8)$$

In this case, since the replacing ettringite occupies a larger volume than the original monosulphoaluminate, expansive stresses are created, which may cause undesirable cracking and deterioration of concrete [10, 11]. The hydration products of the abovementioned reactions are among the most important HCP phases which are considered for the mechanical properties calculations.

2.2 Hydration Products

Based on the hydration reactions discussed in Section 2.1, the products of the reaction between cement components and water are the C-S-H gel, portlandite, AFt and AFm phases, and hydrogarnet. While the first two are the hydration products of alite and belite, the third is formed when a sulfate-rich source is available in the presence of celite/ferrite. The forth is produced from the consumption of the unstable AFt phase when the sulfate-rich source depletes. The last is formed in small amounts when celite is put into contact with water. This section provides an overview of the main HCP crystals used in the current study to calculate the elastic properties of the HCP constituents.

2.2.1 C-S-H Gel

The calcium silicate hydrates (C-S-H) gel has the largest volume contribution to the hydrated cement pastes and is, thus, the main phase responsible for the mechanical properties. The C-S-H gel, which is the result of reactions between the silicate phases of cement and water, can be considered as an amorphous material with variable stoichiometry (i.e., $C_aS_bH_c$). Investigation of the microstructure of the C-S-H dates back to the beginning of the twentieth century, when Michaelis [12] introduced the colloidal nature of C-S-H. The first model that

systematically studied the formation of the C-S-H products was the colloidal model proposed by Powers and Brownyard [13]. This model considered the hydration reaction products as colloidal structures and called them "cement gel". Feldman and Sereda [14] later proposed the layered model for the C-S-H with the assumption that the C-S-H solid particles are composed of non-ordered layers that tend to group together. Based on the colloidal and layered models, a hybrid model was developed by Jennings et al. [15, 16]. In this model, which was called CM-I, the solid particles were considered as spherical building blocks (radius: ~1.2 nm, density: ~2.8 g/cm^3) that form bigger structures called "globule" (radius: ~3 nm and variable density). The level that the globules are packed can be tight or loose, which creates Low Density (LD) or High Density (HD) C-S-H gels, respectively. Jennings [17] proposed the CM-II model as a refinement to the former model. In the new model, while the concept of LD and HD gels is kept, the nature of globules was modified such that the basic building blocks are omitted and, therefore, globules are taken as the basic particles. In this case, the globules are the platelets of ~ 4.2 nm thick. Although the recent model predicts the nanostructure of the C-S-H very well, it is not able to provide detailed information about the solid particles. As a matter of fact, the atomic structure of the C-S-H is still not entirely clear despite the efforts made by a number of researchers, including Diamon et al. [18], Yu et al. [19], Allen and Thomas [20], Jennings et al. [21], and Richardson [22].

The C-S-H gel is composed of calcium layers jointed to the silicate chains that follow a dreierkette pattern repeated every three tetrahedra. The interlayer space of the C-S-H structure is occupied by various cations and water molecules. The composition of the C-S-H can be characterized by the C/S (CaO to SiO_2) ratio, which is typically in the range of 1.2 to 2.1 for an ordinary hydrated Portland cement paste [23, 24]. While the C-S-H gel is found to have a disordered nano-structure in general, some short-range orders can still be identified in it. This has initiated a series of studies that compare the actual structure of the C-S-H with some crystalline phases. Among 30 different crystalline calcium silicate hydrates reported in the literature, the

tobermorite family and jennite have shown several similarities to the C-S-H gel [22]. The analogy between the C-S-H gel and tobermorite is first proposed by Bernal et al. [25]. The X-ray diffraction studies on hydrated C_3S paste showed that the formed C-S-H is much more amorphous than the C-S-H (I) and C-S-H (II) prepared in dilute suspensions with low and high C/S ratios, respectively. The C-S-H (I) is an ill crystalline product which has a fibrous structure with dreierkette silicate chains similar to that of tobermorite 14 Å [8]. Due to their structural similarity, tobermorite has been predominately used as the basic structure to model the C-S-H phase. However, the C/S ratio of tobermorite minerals (~ 0.6-0.83) is lower than that found for the C-S-H gel. On the other hand, under certain special conditions and water excess, a secondary poorly crystalline structure with a higher C/S ratio (~2) is formed, which is called C-S-H (II). X-ray powder diffraction tests showed structural similarities between the C-S-H (II) and jennite [8]. In summary, mainly due to the omission of the bridging silicate group in their structures, the C-S-H (I) and (II) are known as the imperfect structures of fully crystalline tobermorite 14 Å and jennite, respectively.

Starting with the dreierkette silicate chains similarities, various C-S-H models have been proposed in the literature which fall into two main categories of T/Ch and T/J. The main difference between these two categories is the approach proposed to account for the higher C/S ratio in C-S-H gel. The first category, which is called T/CH models [26, 27, 28], mainly consists of tobermorite structures interstratified with layers of portlandite. The second group, on the other hand, is known as T/J models and consists of jennite structures intermixed with tobermorite [29]. The more comprehensive models that have been recently developed incorporate both T/CH and T/J models [22, 30, 31].

2.2.1.1 Tobermorites

The family of tobermorite minerals has been predominantly studied in the literature as they are very similar structurally to the C-S-H formed after the hydration of Portland cement. To this date, a few members of this family has been characterized, including tobermorite 9Å (a.k.a., riversideite), tobermorite 11Å, and tobermorite 14Å (a.k.a., plombierite) [32, 33]. The notation of 9, 11, and 14Å indicates the characteristic basal spacing, which is a function of the degrees of hydration. By going through a progressive dehydration process, tobermorite 11 Å and later tobermorite 9 Å are produced from tobermorite 14 Å, which has the highest water content in the tobermorite group.

The tobermorite minerals contain sheet-like calcium oxide layers ribbed on both sides by the linear silicate chains of the dreierkette form. Through this configuration, the silicate tetrahedra coordinate themselves with respect to the calcium atoms and water molecules that exist in the interlayer space. It should be noted that the structure of tobermorite is repeated after every three tetrahedra. Two of the three tetrahedra share O-O edges with the central Ca-O part of the layer, whereas the third one bridges the other two tetrahedra at the pyramidal apex of the calcium polyhedron [30]. All tobermorites have relatively similar structural features and their interlayer is perpendicular to the c axis. The only difference is that in tobermorite 11 Å, the layers are connected by bridging tetrahedra while there is no interlayer Ca polyhedral.

This study investigates the atomistic model of all the three tobermorites introduced earlier. Tobermorite 9 Å with the chemical constitution of $Ca_5Si_6O_{16}(OH)_2$ has a significant structural similarity to the fibrous structure of the C-S-H. It has a triclinic unit cell with $C\bar{1}$ space group. The C/S ratio of tobermorite 9 Å is 0.8 and its structure contains the calcium layers that are much closer to each other in comparison with the other members of the tobermorite family. Tobermorite 11 Å, which is more hydrated than tobermorite 9 Å, has a chemical constitution ranging from $Ca_5Si_6O_{17}.5H_2O$ to $Ca_4Si_6O_{15}.5H_2O$. It has a monoclinic polytype unit cell with

$B11m$ space group. The C/S ratio of tobermorite 11 Å in this study is 0.66. Tobermorite 14 Å is the most hydrated phase of the tobermorite group and has the chemical composition of $Ca_5Si_6O_{16}(OH)_2.7H_2O$. This tobermorite is a natural crystal, which can be found in different parts of the world. Tobermorite 14 Å has a monoclinic unit cell with $B11b$ space group and its C/S ratio is 0.83. Figures 2-1 through 2-3 show the crystalline structures of tobermorite 9, 11, and 14Å, respectively.

2.2.1.2 Jennite

Jennite is a rare mineral that can be found in nature or synthesized hydrothermally. The chemical constitution of jennite is $Ca_9Si_6O_{18}(OH)_6.8H_2O$ and it has dreierkette silicate chains similar to tobermorite [34]. The crystal of jennite, however, is different from the tobermorite crystals as the bridging tetrahedra in the silicate chains of jennite are additionally connected to the calcium oxide layer (Figure 2-4). Furthermore, unlike the tobermorite family that have the calcium atoms linked to the oxygen atoms of the silicate chains, only half of the calcium atoms in jennite are bonded to the oxygen atoms and the rest are connected to the hydroxyl groups. Jennite has a triclinic unit cell with $P\bar{1}$ space group and density of 2.325 g/cm^3. The C/S ratio of jennite is 1.5, which is greater than the entire tobermorite family.

2.2.2 Portlandite

Portlandite (CH) is the mineral name of crystalline calcium hydroxide, $Ca(OH)_2$, formed during the curing of concrete. Portlandite constitutes up to ~25% of the total paste volume. As discussed earlier, the hydration process of alite and belite produces both C-S-H and calcium hydroxide. The crystal structure of calcium hydroxide is well characterized in the literature [35, 36]. Portlandite has a simple layered structure, in which calcium atoms are octahedrally coordinated to the hydroxyl groups (Figure 2-5). Portlandite dehydrates to calcium oxide at the

temperature of approximately 400 °C. The space group of the portlandite's crystal is $P\bar{3}m1$ with a trigonal shape.

2.2.3 Ettringite

Ettringite ($C_6A\bar{S}H_{32}$) is the most prominent representative of the AFt phase. During the early stages of the hydration of Portland cement, ettringite is formed as a result of the reaction of water and tricalcium aluminate (C_3A) in the presence of a calcium sulfate source like gypsum. Gypsum is typically added to Portland cement to prevent rapid setting while improving strength. This reaction is called early ettringite formation (EEF). After all the available gypsum clinker is depleted, the continuous reaction of water and C_3A consumes ettringite and forms a secondary product called monosulphoaluminate with a lower sulfate content compared to ettringite. Despite the formation of monosulphoaluminate, it should be noted that a considerable amount of ettringite crystals still exists in the mature HCP and contributes to its mechanical characteristics. Ettringite may also be formed in the mature HCP through two other processes known as sulfate attack and delayed ettringite formation (DEF). Sulfate ions penetrating to the concrete from the outside environment (e.g., sulfate-rich water and soil) react with calcium hydroxide and monosulphoaluminate, two other phases of the HCP, to form new ettringite crystals. Furthermore, if the HCP is exposed to a temperature higher than 70° C, monosulphoaluminate releases aluminum and sulfate ions. The aluminum ions are likely to enter into the structure of the C-S-H gel. Therefore, when the temperature decreases again, the Al^{3+}/SO_4^{2-} ratio lowers and ettringite is formed. The latter process of the ettringite formation can cause expansion and consequently cracking of the HCP.

Ettringite has a rod-like or needle-shape morphology with the chemical composition of $Ca_6[Al(OH)_6]_2(SO_4)_3.26H_2O$. The structure of the ettringite crystal has been fully characterized in the literature [37, 38]. A distinct aspect of this crystal is the existence of an

extensive network of hydrogen bonds along a central column of aluminum and calcium polyhedra (Figure 2-6). The aluminum atoms are each six-fold octahedrally coordinated with six hydroxyl groups. The calcium atoms, on the other hand, are each eight-fold coordinated with four hydroxyl groups and four water molecules. The excess charge of the columns is neutralized with the sulphate ions that exist in the channels between them. Ettringite has a trigonal unit cell with a space group of $P31c$ and a density of 1.8 g/cm^3.

2.2.4 Kuzelite

The layered structure of AFm is derived from that of calcium hydroxide, but with one-third of the calcium ions replaced by trivalent ions (e.g., Al^{3+} and Fe^{3+}). In this structure, the resulting positive charge imbalance is compensated by anions (e.g., SO_4^{2-}, CO_3^{2-}, OH^-, and Cl^-) and the remaining interlayer space is filled with water molecules. Monosulphoaluminate (SO_4-AFm) is the most common phase of AFm with a higher Al/Ca ratio in comparison to ettringite. In the early stage of the hydration process of Portland cement, when the sulfate source is consumed and the alumina content decreases, ettringite is dissolved and monosulphoaluminate ($C_4A\bar{S}H_{12}$) is formed. On the other hand, by the sulfate attack, when the alumina content increases, monosulphoaluminate is dissolved and new ettringite is formed. Therefore, the monosulphoaluminate phase in the HCP is highly linked to the ettringite content. The water content in monosulphoaluminate is uncertain ranging from 12 to 18 [8]. While the atomic structure of monosulphoaluminate with low water content has not been characterized yet, the structure of monosulphoaluminate with 18 water molecules in the interlayer space has been found to have a natural analogue called kuzelite. The crystalline structure of kuzelite has been fully characterized by [39]. The main layer of kuzelite consists of the brucite-like cations of $[Ca_2Al(OH)_6]^+$. The calcium ions approach the H_2O molecule of the interlayer and become 7-coordinated. Furthermore, two possible positions of SO_4 are replaced by two molecules of water

in every other cell, which makes the remaining part of the interlayer disordered (Figure 2-7). Kuzelite with the chemical composition of $[Ca_2Al(OH)_6]^+.[0.5SO_4.3H_2O]^-$ has a trigonal unit cell, a space group of $R\bar{3}$, and a density of 2 g/cm^3.

2.2.5 Hydrogarnet

Hydrogrossular is a calcium aluminium garnet series, $Ca_3Al_2(SiO_4)_{3-X}(OH)_{4X}$, with variable stoichiometry where $0 \leq X \leq 3$. Hydrogarnet is the Si-free end member (X = 3) of the hydrogrossular series. In hydrogarnet structure the Si^{4+} is missing from the tetrahedral sites. The charge balance, however, is maintained by bonding a H^+ to each of the four oxygen atoms surrounding the vacant site. In other words, the structure of hydrogarnet results from the isomorphic replacement of $(SiO_4)^{4-}$ by $(OH)_4{}^{4-}$.

Hydrogarnet (C_3AH_6) is formed as a hydration product of celite (C_3A) and ferrite (C_4AF). The contribution of hydrogarnet is typically less than 2% of the total weight of the HCP and it can be mainly found in the older pastes made of calcium aluminate cements or warm cured Portland cements [8, 40]. The crystalline structure of synthetic hydrogarnet has been characterized by Lager et al. [41] using Neutron and X-ray diffraction tests. The chemical constitution of hydrogarnet is $Ca_3Al_2(OH)_{12}$ and its cubic unit cell has a space group of $Ia\bar{3}d$ (Figure 2-8).

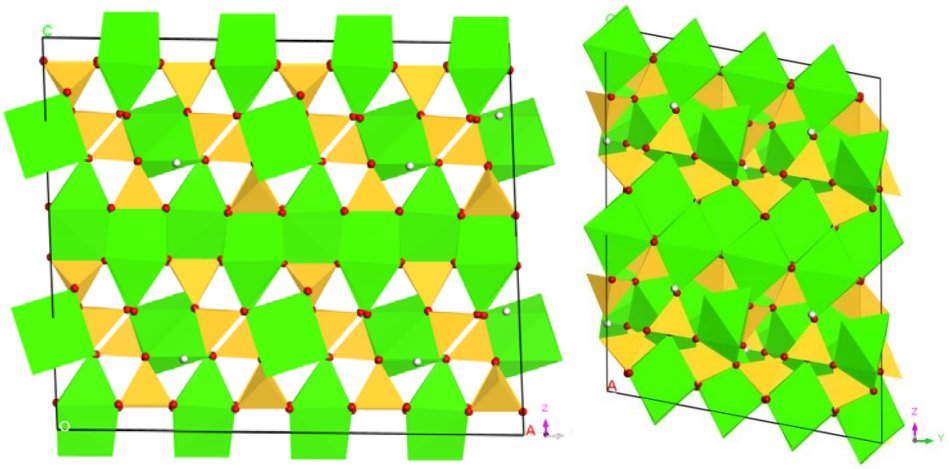

Figure 2-1 Two views of the 2a×2b×2c supercell of tobermorite 9 Å
(Green: Ca; Orange: Si; Red: O; and White: H)

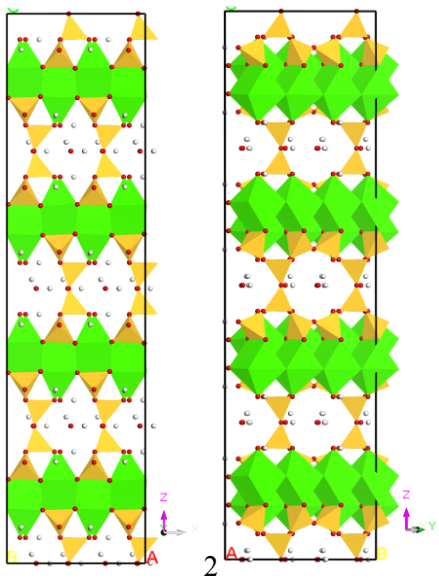

Figure 2-2 Two views of the 2a×2b×2c supercell of tobermorite 11 Å
(Green: Ca; Orange: Si; Red: O; and White: H)

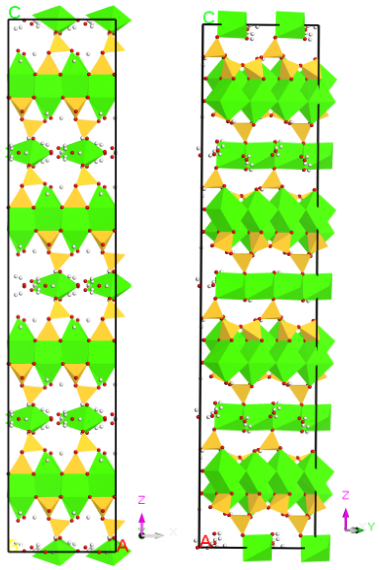

Figure 2-3 Two views of the 2a×2b×2c supercell of tobermorite 14 Å
(Green: Ca; Orange: Si; Red: O; and White: H)

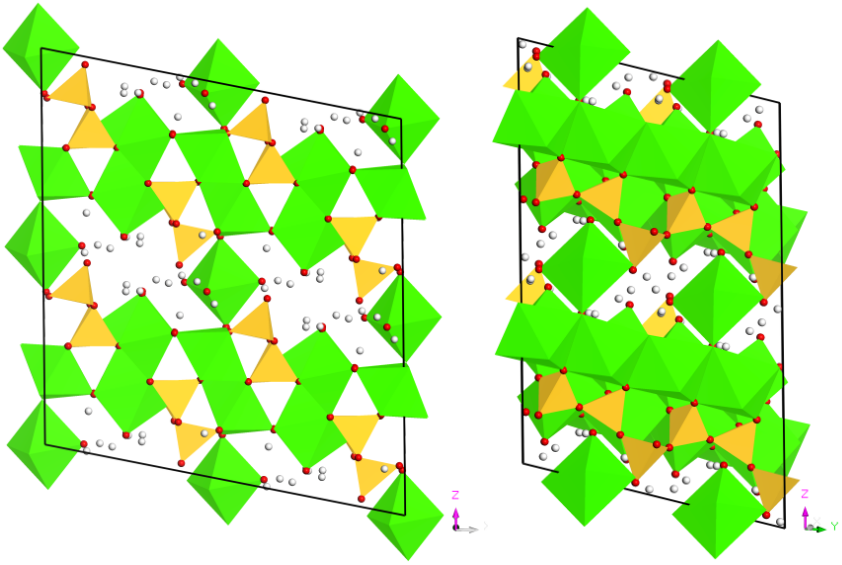

Figure 2-4 Two views of the 2a×2b×2c supercell of jennite
(Green: Ca; Orange: Si; Red: O; and White: H)

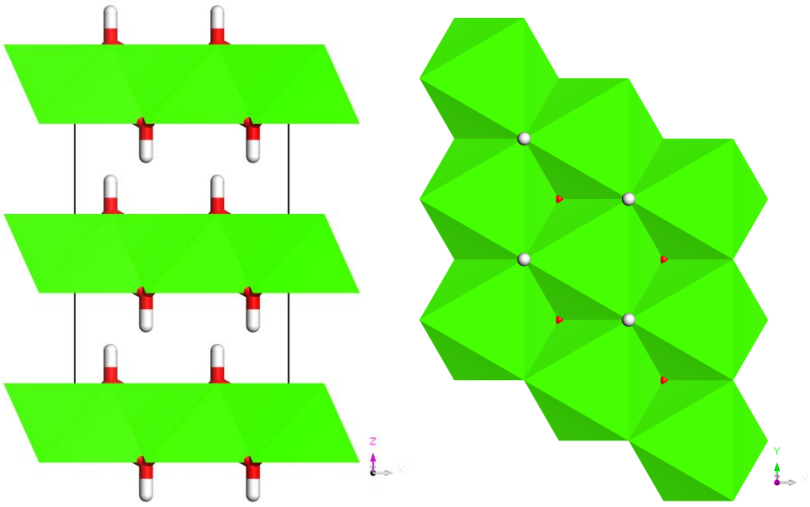

Figure 2-5 The layered structure of portlandite (left) and hexagonal coordination of calcium atoms to the hydroxyl groups (right) (Green: Ca; Red: O; and White: H)

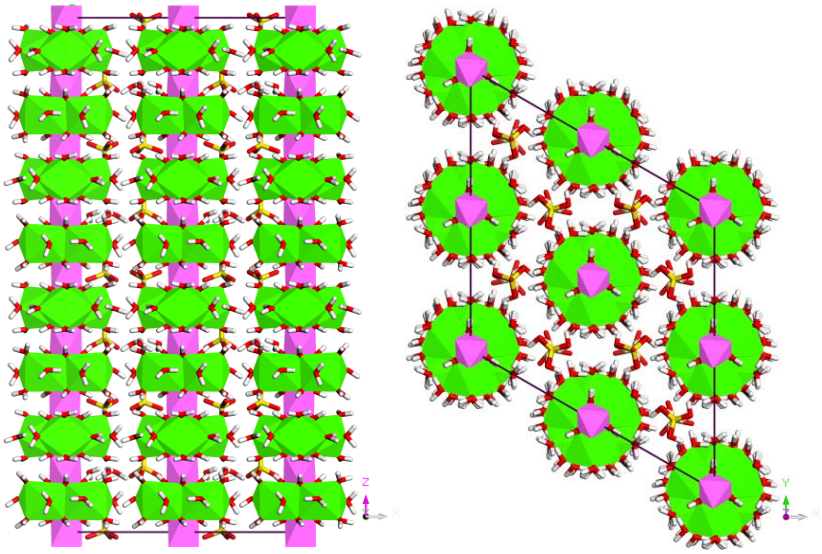

Figure 2-6 The column-like arrangement of the aluminum and calcium polyhedra (left) and top view of ettringite (right) (Green: Ca; Pink: Al; Yellow: S; Red: O; and White: H)

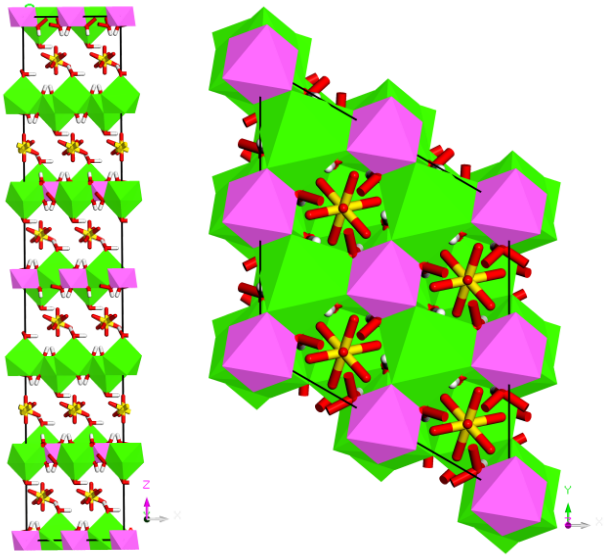

Figure 2-7 Two views of the 2a×2b×2c supercell of kuzelite
(Green: Ca; Pink: Al; Yellow: S; Red: O; and White: H)

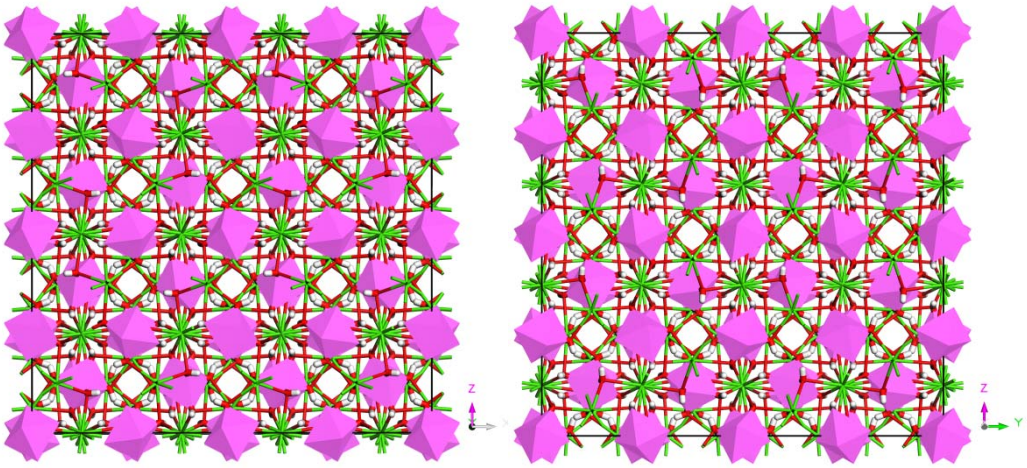

Figure 2-8 Two views of the 2a×2b×2c supercell of hydrogarnet
(Green: Ca; Pink: Al; Red: O; and White: H)

CHAPTER 3

OVERVIEW OF ATOMISTIC SIMULATION METHODS

While the concept of atom as the indivisible particle which composes matter dates back to ancient Greece and India, John Dalton in 1805 was the first who experimentally established the modern concept of atom as the basic unit of matter. However, the first successful model based on the application of the concept of atoms in describing a real system was conducted during the second half of the 19th century when Clausius, Maxwell, and Boltzman developed the kinetic theory of gases. The majority of systems and the interactions which govern them are too complicated to be evaluated analytically using models. With the advanced development in computer technology, large systems of equations can be solved numerically through atomistic simulations. Metropolis et al. in 1953 [42] proposed the first computational simulation of liquids at Los Alamos MANIAC using the modified Monte Carlo (MC) integration over configuration space. Following the successes in MC simulations, Molecular Dynamics (MD) was developed by Alder and Wainwright [43], and Rahman [44] in late 50s and early 60s respectively.

The MC and MD simulations rely on the classical models and equations; however, there are several other atomistic models such as ab-initio and Molecular Mechanics (MM) method, etc. which can be described by quantum mechanics. These atomistic simulations are chosen based on their potential for solving specific problems. Since the MD method is capable of predicting structural, mechanical, and chemical behavior of materials through the solution of the Newton's equation of motion, it is found well-suited for the purposes of this study. The main objective of this chapter is to provide the background required for the MD simulations conducted throughout this study to predict the mechanical characteristics of the HCP phases.

3.1 Introductory Statistical Mechanics

Statistical mechanics is a branch of mathematical physics, which studies the average behavior of a mechanical system with an uncertain state using the probability theory [45]. The conversion of microscopic description (coordinates, velocities, potential energy, kinetic energy, etc.) to macroscopic observables (temperature, pressure, internal energy, stress tensor, strain tensor, etc.) is all carried out in the realm of statistical mechanics. In statistical mechanics, the Ergodic theorem is the approach employed to calculate the macroscopic properties from the molecular properties. Before stating the theorem, the concept of an ensemble of systems must be first introduced.

3.1.1 Method of Ensembles

An ensemble is a very large collection of M systems, each of which represents a replica of the thermodynamic system under study in the sense that the variables characterizing the real system are the same for each member of the ensemble [46]. For example, consider a system of N particles of single component with the total volume of V immersed in a large heat bath at the temperature of T. The assigned properties are sufficient to determine the thermodynamic state of the system. In this case, the ensemble consists of M systems constructed to duplicate the thermodynamics state (N, V, T) of the original system. Table 3-1 summarizes the four widely used ensembles defined for the most important thermodynamical environments.

3.1.2 Ergodic Theorem

The Ergodic theorem states that for a system at the equilibrium, the time average of a system property, A, in the thermodynamic system of interest is equivalent to the ensemble average of A in the limit as $M \longrightarrow \infty$.

$$\langle A \rangle_{time} = \lim_{M \to \infty} \langle A \rangle_{ensemble} \tag{3.1}$$

The symbol ⟨ ⟩ denotes the average variable. In a classical system, any system state can be uniquely defined from the position ($\boldsymbol{r}$) and linear momentum ($\boldsymbol{p}$) of all particles existing in the system. The ensemble average of a property A is calculated as:

$$\langle A \rangle_{ensemble} = \iint A(\boldsymbol{r}, \boldsymbol{p}) \rho(\boldsymbol{r}, \boldsymbol{p}) d\boldsymbol{r}\, d\boldsymbol{p} \tag{3.2}$$

where $\boldsymbol{r} = \{r_x{}^i, r_y{}^i, r_z{}^i\}$ and $\boldsymbol{p} = \{p_x{}^i, p_y{}^i, p_z{}^i\}$ for i=1,2…,N. $\rho(\boldsymbol{r}, \boldsymbol{p})$ is the probability density distribution can be calculated as:

$$\rho(\boldsymbol{r}, \boldsymbol{p}) = \frac{1}{Q} exp\left(-\frac{H(\boldsymbol{r}, \boldsymbol{p})}{k_B T}\right) \tag{3.3}$$

in which Q is called partion function which sums over states and obtained from:

$$Q = \iint exp\left(-\frac{H(\boldsymbol{r}, \boldsymbol{p})}{k_B T}\right) d\boldsymbol{r} d\boldsymbol{p} \tag{3.4}$$

where k_B is the Boltzmann's constant (1.380662e-23 J/K), $H(\boldsymbol{r}, \boldsymbol{p})$ is the Hamiltonian.

The time average of a system property A can be calculated by:

$$\langle A \rangle_{time} = \frac{1}{M} \sum_{i=1}^{\boldsymbol{M}} A(\boldsymbol{r}, \boldsymbol{p}, t_i) \tag{3.5}$$

where M is the number of measurements taken.

While the Monte Carlo technique generates trajectories in the constraint of an ensemble average the Molecular Dynamics method generates those over time. According to the Ergodic theorem, both viewpoints are equal [47]. For example, in order to measure the pressure in the (*N, V, E*) system discussed earlier, the force exerted on the wall of the system should be calculated. In

the time average viewpoint, all the evolution of the system over time should be taken into account. In this case, force is a function of time, thus, the time average of force over a period of time needs to be calculated. On the other hand, at any instant of time, the calculated pressure is different in different systems of an ensemble; therefore, the ensemble average of pressure is the average over the instantaneous values of the pressure [46].

3.2 Monte Carlo Techniques

As mentioned earlier, Monte Carlo (MC) techniques take the advantage of ensemble averaging in generating trajectories. This can be achieved by a sequence of random samples obtained from a probability distribution. The Metropolis-Hastings algorithm is one of the well-known methods of generating random samples from multi-dimensional distributions especially when the number of dimensions is high [42, 48]. The procedure starts with an initial state (*A*) and initial energy, *H(A)*. Then a loop is run to generate new states (*B*) from the previous ones until the convergence of the desired property is achieved. The acceptance or rejection of new configuration is in accordance to an energy criterion. To do this, for example a random number $o < p < 1$ is first drawn. The new configuration is then acceptable if

$$p < exp\left[-\frac{H(B) - H(A)}{k_B T}\right] \tag{3.6}$$

Many MC algorithms use the same procedure to advance a system to a new configuration. Therefore, the move from former state towards the new state is arbitrary, which makes this method simple and widely applicable. In the end, the ensemble average of property *A* can be calculated by:

$$\langle A \rangle = \frac{1}{N_A}\sum_{i=1}^{N_A} A(i) \tag{3.7}$$

where N_A is the number of iterations. One of the drawbacks of this method is that additional knowledge about how the system evolves is required to generate new states. MC can be typically used only for equilibrium processes. Concerning fracture phenomena for example, MC does not provide information about how system goes from an unstable state to a stable state while molecular dynamics can naturally describe the atomic bond breaking processes. Furthermore, in contrast to MC, molecular dynamics method provides detailed information about the full dynamical trajectories while MC does not generate actual trajectories in time [47].

3.3 Molecular Dynamics Method

The Molecular Dynamics (MD) method plays a progressively important role in atomistic simulations conducted in many areas of science and engineering. Through a MD simulation, the time evolution of trajectories, positions, and velocities of atoms are calculated by measuring the interatomic forces. The MD method has been used in the current study to predict the elastic properties of the main constituents of the HCP. For this purpose, three stages of analysis are performed: i) *initialization*, (ii) *equilibration*, and iii) *production*. In the initialization stage, a variety of parameters including simulation cell properties, atomic coordinates, atomic mass, bond connectivity between atoms, partial charge of atoms, and boundary conditions are defined. While the initial coordinates of atoms are specified based on the density of system under study at the specified thermodynamic state of simulation, the initial velocities are drawn randomly from a Maxwell-Boltzmann distribution. To evaluate the interatomic interactions, the system forces must be determined at each step of simulation. This cannot be achieved without introducing a forcefield (potential) that properly estimates the nature of forces interacting among different atoms of the specific material. Based on the application and material of interest, the choice of forcefield is left to the discretion of user.

3.3.1 Forcefields

Interaction between dissimilar particles is formulated through the concept of interatomic potential called forcefield. Numerous forcefields with different applications have been proposed in the literature. Each forcefield often consists of several terms that can be divided into two main categories of bonded and non-bonded terms. The parameters of forcefield terms are adopted for certain range of atom types either by experimental methods such as nuclear magnetic resonance (NMR) or from ab initio quantum mechanics calculations. While the choice of forcefield is the most prominent issue in forcefield-based atomistic simulations, there is no universal guideline available in the literature to select a specific forcefield, especially for HCP phases. To study the effects of forcefields on the estimated mechanical properties of the HCP phases, the available forcefields, including COMPASS, Universal, Dreiding, and ClayFF, are investigated in the current study. A brief description of each forcefield along with the functional form of its potential energy is discussed in this section.

3.3.1.1 COMPASS

The condensed-phase optimized molecular potentials for atomic simulation studies (COMPASS) is an ab initio forcefield optimized and tested for simulating crystals, polymers, and inorganic materials, such as metals, metal oxides, and metal halides. The potential energy of COMPASS is given by [49]:

$$E^{\mathrm{COMPASS}} = \left(E_{\mathrm{b}} + E_{\theta} + E_{\phi} + E_{\chi} + E_{\mathrm{bb}} + E_{\mathrm{b}\theta} + E_{\mathrm{b}\phi} + E_{\theta\phi} + E_{\theta\theta} + E_{\theta\theta\phi}\right) + \left(E_{\mathrm{col}} + E_{\mathrm{vdW}}\right) \quad (3.8)$$

The terms in Equation 3.8 can be divided into the two main categories of bonded and non-bonded terms. The bonded terms represent the energy that corresponds to the internal coordinates of bond (b), angle (θ), torsion angle (ϕ), and out-of-plane angle (χ). Furthermore, the

cross-coupling terms are included to represent the combination of two internal coordinates. As for non-bonded terms, the Coulombic function (E_{col}) for electrostatic interactions and the Lenard-Jones 9-6 function (E_{vdW}) for van der Waals interactions are included.

3.3.1.2 Universal

Universal forcefield (UFF) is used for main-group inorganics and metal complexes. As it fully covers the periodic table, UFF is useful in modeling the materials with atoms for which other alternative forcefields are not available. The UFF potential function is a superposition of various two-body, three-body, and four-body interactions expressed as a summation of bonded (valance) and non-bonded interactions [50]. The first four terms in Equation 3.9 are the valance interactions while the last two terms represent the non-bonded interactions:

$$E^{\mathrm{UFF}} = (E_{\mathrm{R}} + E_{\theta} + E_{\phi} + E_{\omega}) + (E_{\mathrm{vdw}} + E_{\mathrm{es}}) \tag{3.9}$$

where E_{R} is the bond stretching energy, which is described either as a harmonic oscillator or with the Morose function; E_{θ} is the bond angle bending energy described with a cosine Fourier expansion of the bond angle (θ); E_{ϕ} is the energy associated with dihedral angle torsion described with a cosine Fourier expansion of the torsion angle (ϕ) for two bonds *i*-*j* and *k*-*l* connected with a bond *j*-*k*; and E_{ω} is the inversion energy term described by a cosine Fourier expansion for the atom *i* connected to the three other atoms of *j*, *k* and *l*. In the UFF, the Lennard-Jones 6-12 and Columbic functions are used for the non- bonded van der Waals (E_{vdw}) and electrostatic (E_{es}) interactions, respectively.

3.3.1.3 Dreiding

Dreiding forcefield has been widely used for various main-group inorganics. The potential energy in Dreiding is formulated as a superposition of bonded (valance) and non-bonded

interactions where the former is determined based on the bonds of the atomic structure and the latter is calculated as a function of distance between atoms [51]. In Equation 3.10, the first four terms are considered as valance interactions while the last three terms represent the non-bonded interactions:

$$E^{\text{Dreiding}} = (E_{\text{B}} + E_{\text{A}} + E_{\text{T}} + E_{\text{I}}) + \left(E_{\text{vdw}} + E_{\text{Q}} + E_{\text{hb}}\right) \tag{3.10}$$

where E_{B} is the bond stretch interaction energy described either as a harmonic oscillator or with the Morose function similar to UFF; E_{A} is the three-body bond angle bending energy term, which has a harmonic cosine form for two bonds *i-j* and *j-k* sharing a common atom *j*; E_{T} is the dihedral angle torsion energy term for two bonds *i-j* and *k-l* connected via a common bond *j-k*; and E_{I} is the inversion energy term for the atom *i* bonded to the three other atoms of *j*, *k*, and *l*. Concerning non-bonded energy terms, van der Waals interactions (E_{vdw}) are described either by the Lennard-Jones 12-6 or an exponential function. The electrostatic interactions (E_{Q}) in Dreiding is calculated using the Columbic function while the hydrogen bonding potential is captured by the E_{hb} energy term.

3.3.1.4 ClayFF

The ClayFF forcefield has been specifically developed to simulate the ion-ion and ion-water interactions of oxide and hydroxide phases that exist in cementitious materials [52]. The total potential energy in ClayFF is obtained from the summation of electrostatic (E_{coul}), short-range (E_{vdw}), bond stretch (E_{bond}), and angle bend (E_{angle}) interactions:

$$E^{\text{ClayFF}} = E_{\text{coul}} + E_{\text{vdw}} + E_{\text{bond}} + E_{\text{angle}} \tag{3.11}$$

It should be noted that for bonded intermolecular interactions, i.e., bond stretch and angle bend interactions, the electrostatic and short-range interactions are excluded. The electrostatic

interactions are represented by the Coulombic functional form, where the energy of the interaction is inversely proportional to the distance of separation, r_{ij}, between atom *i* and *j*. The Ewald summation method is used to properly calculate the long-range Coulombic interactions. The short-range interactions, often named as van der Waals interactions, are represented by the conventional Lennard-Jones (12-6) function, which includes the short-range repulsion associated with the increase in energy as two atoms approach each other and the attractive dispersion energy. The bond stretch energy is considered between oxygen and hydrogen atoms of either a hydroxyl or a water molecule and is described by a simple harmonic term. To improve the vibrational motion of hydroxyl groups, an angle bend (three-body) term is introduced in the form of a simple harmonic relationship.

3.3.2 Energy Minimization

After the initialization stage, an energy minimization is conducted on the system. The goal in energy minimization is to obtain the most stable structural configuration by varying the atomic positions. It should be noted that the energy minimization is carried out at zero temperature in which the kinetic energy is zero. Hence, only the potential energy is minimized. To perform energy minimization a variety of algorithms exist. Newton-Raphson, steepest descent, conjugate gradient and Quasi-Newton are among the widely used energy minimization methods. The Newton-Raphson method is a good choice for small molecules; however, when a structure is far from the minimum energy where the energy surface is anharmonic, the optimization may become unstable. Furthermore, as the Hessian matrix terms are difficult to derive, this method is computationally costly for molecular modeling. Unlike the Newton-Raphson method, the steepest descent method can be employed when configuration is far from the minimum energy. The conjugate gradient method is the best choice for large models. However, similar to the Newton-Raphson method the conjugate gradient method can also be unstable when configuration is far

from local minima. Therefore, in this case it is often beneficial to use the steepest descent method for the first 10-100 steps of the optimization. The Quasi-Newton method follows the basic idea of the conjugate gradient method within the Newton-Raphson framework to direct the optimization along a more efficient pathway. In this study, to optimize the geometry of the atomistic models, the smart algorithm, which is a cascade of the steepest descent, adjusted basis set Newton-Raphson (ABNR), and Quasi-Newton method is employed.

After the initialization and energy minimization stages are completed, the new atomic coordinates are used for the equilibration stage. Through the equilibration stage, the interaction between a pairs of atoms (F_{ij}) is determined by the negative gradient of the total potential energy (*U)*, which includes all the bonded and non-bonded interactions, with respect to the separation distance (r_{ij}):

$$F_{ij} = -\frac{\partial U}{\partial r_{ij}} \tag{3.12}$$

The net force acting on an atom *i* (F_i) is then calculated by summing up the interactions between atom *i* and the surrounding atoms *j*. The acceleration of atom *i* (a_i) with the mass of m_i is then calculated using the Newton's equation of motion ($a_i = \frac{F_i}{m_i}$). Finally the new coordinates and velocities can be obtained by numerical integration of the equation of motion.

3.3.3 Integrating the Equations of Motion

The Newton's second law is the fundamental equation governing the molecular motion. In the MD simulation process, the Newton's equation of motion must be integrated. The Verlet, leapfrog and velocity Verlet algorithms are the most well-known finite difference schemes used to integrate the equation of motion. In these methods the idea is to develop new coordinates and velocities from the old ones for a particle *i*.

3.3.3.1 Verlet Algorithm

The Verlet algorithm [53] is the most well-known numerical technique to integrate the Newton's equation of motion. This method is a simple central difference scheme that will be discussed below. Suppose the Taylor expansion of the position vector r_i:

$$r_i(t \pm \Delta t) = r_i(t) \pm v_i(t)\Delta t + \frac{1}{2}a_i(t)(\Delta t)^2 \tag{3.13}$$

where Δt is the size of time step and $r_i(t)$, $v_i(t)$, and $a_i(t)$ are the position, velocity and acceleration vector of the i-th atom at time t, respectively. Adding $r_i(t + \Delta t)$ to $r_i(t - \Delta t)$ yields

$$r_i(t + \Delta t) = 2r_i(t) - r_i(t - \Delta t) + a_i(t)(\Delta t)^2 \tag{3.14}$$

Equation 3.14 provides a direct link between the new and old positions, and accelerations. The velocity vectors are, then, estimated as:

$$v_i(t) = \frac{r_i(t+\Delta t) - r_i(t-\Delta t)}{2\Delta t} \tag{3.15}$$

3.3.3.2 Leapfrog Algorithm

In the leapfrog algorithm, the positions and velocities are updated at interleaved time points. The new position is obtained at integer time steps while the velocity is updated at integer-plus-a-half time steps. Hence, they are called "leapfrog" from one another. Equations 3.16 and 3.17 show how the updated positions and velocities are calculated, respectively.

$$r_i(t + \Delta t) = r_i(t) + v_i\left(t + \frac{1}{2}\Delta t\right)\Delta t \tag{3.16}$$

$$v_i\left(t + \frac{1}{2}\Delta t\right) = v_i\left(t - \frac{1}{2}\Delta t\right) + a_i(t)\Delta t \tag{3.17}$$

3.3.3.3 Velocity Verlet Algorithm

This method is a variant of Verlet algorithm, which is similar to the leapfrog algorithm except that the new positions and velocities are updated at the value of time step. In the velocity Verlet algorithm the equations for updating positions and velocities are:

$$r_{\mathrm{i}}(t+\Delta t) = r_{\mathrm{i}}(t) + v_{\mathrm{i}}(t)\Delta t + \frac{1}{2}a_{\mathrm{i}}(t)(\Delta t)^2 \tag{3.18}$$

$$v_i(t+\Delta t) = v_i(t) + \frac{a_i(t) + a_i(t+\Delta t)}{2}\Delta t \tag{3.19}$$

3.4 Modifying Equation of Motion

When the Newton's equation of motion is integrated using the algorithms introduced earlier, the resulting thermodynamical ensemble is *NVE* where the number of particles (*N*), the total volume (*V*) and the total energy (*E*) of the system remains constant during the MD simulation. To obtain other thermodynamical ensembles, the equation of motion should be modified. In constant-temperature dynamics (e.g., canonical ensemble), the temperature of the system is maintained near the target value. Berendsen, Nose dynamics, Andersen and Nose-Hoover-Langevin dynamics methods are among the most well-known thermostats that control temperature of system. Similarly, the pressure of the system is controlled using barostats in constant-pressure dynamics (e.g., isobaric-isothermal ensemble). Parrinello-Rahman, Berendsen, and Andersen methods are among the most commonly used barostats.

The equilibration stage can be summarized as the following: based on the energy optimized coordinates and assigned velocities, the forces between atoms are calculated using the chosen forcefield; the Newton's equations of motion are integrated over the time step to compute new atomic positions and velocities. This step-by-step procedure continues until the system reaches the thermodynamic equilibrium. Finally, in the production stage, another MD simulation

is performed to record the trajectories. The desired output parameters are extracted after the trajectory data are analyzed. In summary, the general procedure of an MD simulation follows the steps given in Figure 3-1.

Table 3-1 Choices of thermodynamical ensembles

Ensemble	Ensemble Name	Thermodynamic Environment
NVE	Microcanonical ensemble	An isolated system
NVT	Canonical ensemble	A closed, isothermal system
μVT	Grand canonical ensemble	An open, isothermal system
NPT	Isobaric-isothermal ensemble	A closed, isobaric, isothermal system
***μ* is chemical potential, *P* is the pressure of system**		

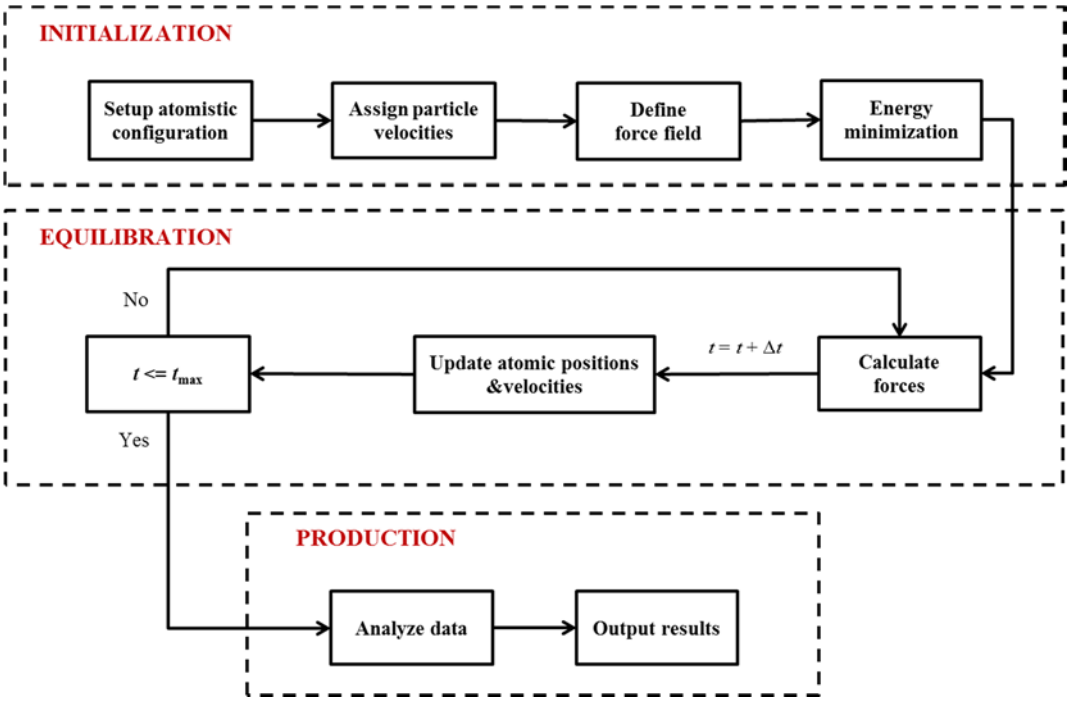

Figure 3-1 Numerical scheme of MD simulation

CHAPTER 4

PREDICTION OF ELASTIC PROPERTIES

The elastic properties of the HCP phases are investigated at the nano-scale based on the concept of the interatomic bonds and forces. If two atoms that share a bond are subjected to an external tensile force, the bond length increases, which is opposed by internal attractive forces. Conversely, when an external compressive force decreases the bond length between the two atoms, internal repulsive forces act to move them apart. The existence of such attractive and repulsive forces indicates that the equilibrium condition is the only condition in which the external forces are completely balanced by the internal forces. It should be noted that if the applied external force reaches certain thresholds, the bond between the atoms may break, which results in plastic deformation, i.e., permanent changes in the atomic structure. This, however, is not the case if the external force remains in the elastic range. This is called elastic behavior, which means that atomic structure tends to return to its initial shape after being deformed. In the elastic range, the interatomic force is proportional to the change in the bond length and, can be studied through the relation between stress and strain tensors.

A body which is subjected to external forces is in a state of stress. Stress is a second-order tensor with nine components, σ_{ij}:

$$\begin{bmatrix} \sigma_{11} & \sigma_{12} & \sigma_{13} \\ \sigma_{21} & \sigma_{22} & \sigma_{23} \\ \sigma_{31} & \sigma_{32} & \sigma_{33} \end{bmatrix} \tag{4.1}$$

In an atomistic simulation the stress components can be obtained using the so-called virial expression.

$$\sigma_{ij} = \frac{1}{V_0}\left[\left(-\sum_{\alpha} m_\alpha v_{\alpha,i} v_{\alpha,j}\right) + \left(\frac{1}{2}\sum_{\alpha,\beta,\alpha\neq\beta} \frac{\partial\phi(r)}{\partial r}\frac{r_i}{r} r_j\Big|_{r=r_{\alpha\beta}}\right)\right] \tag{4.2}$$

where V_0 refers to the undeformed system volume. In the first term of the above equation, which is also known as the kinetic term, m_α is the mass of atom α, and $v_{\alpha,i}$ is the projection of the velocity vector of atom α along the coordinate i. The second term of Equation 4.2 is the force contribution in stress components where $\phi(r)$ is the potential energy, r_i denotes the projection of the interatomic distance vector r along the coordinate i, and the indices α, β is the atom numbers considered in the calculation. It has been shown that the kinetic term is not equivalent to the mechanical Cauchy stress [47]. Therefore, in elastic properties calculations only the force part should be considered excluding the kinetic term. This measure is referred to as the Zhou's virial stress. Once external forces are applied to a body, the relative positions of atoms within the body change, which results in a geometric deformation that can be quantified via the strain tensor:

$$\begin{bmatrix} \varepsilon_{11} & \varepsilon_{12} & \varepsilon_{13} \\ \varepsilon_{21} & \varepsilon_{22} & \varepsilon_{23} \\ \varepsilon_{31} & \varepsilon_{32} & \varepsilon_{33} \end{bmatrix} \tag{4.3}$$

where ε_{ij} are the strain components.

4.1 Stress-Strain Relationship

How are the stresses and strains related to one another? The answer to this key question is addressed by the thermodynamical view of the physical process of elastic deformation [47]. The first law of thermodynamics states that the energy of an isolated system, *U*, is conserved. This implies that the change in the internal energy of a closed system is equal to the amount of heat (Q) supplied to the system by its surrounding, plus the work (W) done on the system by its surroundings. Therefore, the first law of thermodynamics is formulates as:

$$\Delta U = W + Q \tag{4.4}$$

The work done on the system by its surroundings can be calculated by:

$$W = xF_e \tag{4.5}$$

where x is the deformation, and F_e is the applied force. From the first law of thermodynamics the change in the internal energy can be written by:

$$\frac{\partial U}{\partial t} = \frac{\partial W}{\partial t} + \frac{\partial Q}{\partial t} = \dot{x}F_e + \frac{\partial Q}{\partial t} \tag{4.6}$$

The second law of thermodynamics, however, states that the entropy (*S*) of an isolated system never decreases.

$$\frac{\partial S}{\partial t} \geq \frac{1}{T}\frac{\partial Q}{\partial t} \tag{4.7}$$

This implies that the change in entropy cannot be smaller than the entropy provided to the system in the form of heat. Dissipation (*D*) is introduced as a result of irreversible processes that take place in thermodynamic systems. The dissipation rate can then be obtained from the difference between the left and right side in Equation 4.7.

$$\frac{\partial D}{\partial t} = T\frac{\partial S}{\partial t} - \frac{\partial Q}{\partial t} \geq 0 \tag{4.8}$$

Now solving Equation 4.6 for $\frac{\partial Q}{\partial t}$ and plugging into Equation 4.8 yields

$$\frac{\partial D}{\partial t} = \dot{x}F_e - \frac{\partial}{\partial t}(U - TS) \geq 0 \tag{4.9}$$

The quantity $A = U - TS$ is called Helmholtz free energy, which implies the maximum internal capacity of the system to do work on its surroundings. By definition, all deformations in the elastic region are reversible, which means no dissipation exists. Hence,

$$\dot{x}F_e - \frac{\partial A}{\partial t} = 0 \tag{4.10}$$

Expanding $\frac{\partial A}{\partial t}$ in Equation 4.10:

$$\dot{x}F_e - \frac{\partial A}{\partial x}\frac{\partial x}{\partial t} = \dot{x}\left(F_e - \frac{\partial A}{\partial x}\right) = 0 \tag{4.11}$$

Since Equation 4.11 is valid for any deformation rate, thus, the applied force is the first derivative of the Helmholtz free energy with respect to deformation:

$$F_e = \frac{\partial A}{\partial x} \tag{4.12}$$

To characterize material properties independent of the size of the body, Equation 4.12 can be renormalized by dividing both sides of it by the volume of the undeformed body. The undeformed volume of a prism, V_0, can be expressed by AL, where A is the cross-sectional area and L is the length of body.

$$\frac{F_e}{A} = \frac{1}{V_0}\frac{\partial A}{\frac{\partial x}{L}} \tag{4.13}$$

Noting that $\frac{F_e}{A}$ and $\frac{\partial x}{L}$ is the definition of stress, σ, and strain, ε, respectively, therefore,

$$\sigma = \frac{1}{V_0}\frac{\partial A}{\partial \varepsilon} \tag{4.14}$$

Equation 4.13 can be written in tensor notation:

$$\sigma_{ij} = \frac{1}{V_0}\frac{\partial A}{\partial \varepsilon_{ij}} \tag{4.15}$$

Each of the stress and strain tensors is a second-order tensor related by the fourth-order tensor called elasticity tensor. The components of the elasticity tensor are known as elasticity tensor coefficients $\left(C_{ijkl}\right)$ and can be defined via the generalized Hooke's law.

$$C_{ijkl} = \left.\frac{\partial \sigma_{ij}}{\partial \varepsilon_{kl}}\right|_T = \left.\frac{1}{V_0}\frac{\partial^2 A}{\partial \varepsilon_{ij}\partial \varepsilon_{kl}}\right|_T \tag{4.16}$$

This indicates that the elastic stiffness matrix and the elastic properties calculated based of which are highly influenced by the Helmholtz free energy. The free energy of crystalline materials (e.g., metals and ceramics) at moderate temperature is mainly controlled by the internal

energy (U) [47, 54]. Therefore, in the HCP phases under consideration, the entropic term (-TS) can be neglected. In this study the elasticity tensor coefficients, often called elastic constants, are calculated using the static method which neglects the contribution of the entropic term on deformation. Therefore, Equation 4.16 can be rewritten as

$$C_{ijkl} = \left.\frac{\partial \sigma_{ij}}{\partial \varepsilon_{kl}}\right|_T = \left.\frac{\partial^2 \Psi}{\partial \varepsilon_{ij} \partial \varepsilon_{kl}}\right|_T \tag{4.17}$$

where $\Psi = \frac{U}{V_0}$ is the strain energy density defined as the energy stored by a system undergoing deformation [54]. Through this approach, the MD equilibrated simulation cell of each HCP components is subjected to twelve strains, three uniaxial tension/compression pairs and three pure shear pairs, in such a way that each time only one component of the strain tensor is non-zero (e.g., $\varepsilon = 0.003$ in this study). After each deformation, an energy minimization is conducted to restore the state of mechanical equilibrium. The elastic constants can then be calculated by solving Equation 4.16 numerically using a finite different scheme.

Since the stress and strain tensors are both symmetric, it is more convenient to represent them in a vector format, which is also known as the Voigt vector notation, and relate them with an elasticity matrix, which is 6×6 with 21 independent elastic constants (C_{ij}). For small deformations Equation 4.17 can be expressed by the generalized Hooke's law.

$$\sigma_i = C_{ij} \varepsilon_j \tag{4.18}$$

It should be noted that in this notation, the elasticity matrix is no longer a tensor since it does not obey the required transformation rules any more. The elastic properties of material are characterized using the elastic constants.

4.2 Calculation of Mechanical Properties

Elasticity matrix enables one to calculate the elastic properties of materials. In most cases, 21 independent elastic constants exist which describes the relation between stress and strain. However, in few materials, the number of independent constants is significantly reduced. Depending on the number of independent elastic constants needed to form the elasticity matrix, materials can be divided into the two general categories of isotropic and anisotropic materials.

4.2.1 Isotropic Materials

In isotropic materials, the stress-strain relationships do not depend on the direction of the applied loads. The elastic properties of an isotropic material can be fully determined by specifying only two independent coefficients. The elasticity matrix of an isotropic material can be written as:

$$\begin{bmatrix} \lambda+2\mu & \lambda & \lambda & 0 & 0 & 0 \\ \lambda & \lambda+2\mu & \lambda & 0 & 0 & 0 \\ \lambda & \lambda & \lambda+2\mu & 0 & 0 & 0 \\ 0 & 0 & 0 & \mu & 0 & 0 \\ 0 & 0 & 0 & 0 & \mu & 0 \\ 0 & 0 & 0 & 0 & 0 & \mu \end{bmatrix} \tag{4.19}$$

where λ and μ are the Lamé constants. The other elastic properties can also be calculated from:

$$K = \lambda + \frac{2}{3}\mu \tag{4.20}$$

$$G = \mu \tag{4.21}$$

$$E = \mu\left(\frac{3\lambda+2\mu}{\lambda+\mu}\right) \tag{4.22}$$

$$\nu = \frac{\lambda}{2(\mu+\lambda)} \tag{4.23}$$

where K, G, and E are the bulk, shear and Young's modulus, respectively, and ν is the Poisson's ratio.

4.2.2 Anisotropic Elasticity

In anisotropic materials, mechanical behavior depends on the direction of the applied load. Hence, contrary to isotropic materials, a more detailed investigation is necessary as there are more than two independent elastic constants. Averaging the elastic constants is a suitable approach to characterize the elastic properties of anisotropic materials. Following is an introduction to two common averaging schemes widely used for anisotropic materials.

4.2.2.1 Molinari Approximation

This approach is based on probability distributions and statistical moments mostly used for polycrystals [55]. According to the Molinari approximation the bulk (K) and shear (G) moduli can be calculated by Equations 4.24 and 4.25, respectively.

$$K = \frac{C_{33}(C_{11} + C_{12}) - 2{C_{13}}^2}{C_{11} + 2C_{33} + C_{12} - 4C_{13}} \tag{4.24}$$

$$G = \frac{3}{2}\left(\frac{C_{33}(C_{11} + C_{12}) - 2{C_{13}}^2}{2C_{11} + C_{33} + 2C_{12} + 4C_{13}}\right) \tag{4.25}$$

4.2.2.2 Voigt-Reuss-Hill Approximation

Voigt [56] proposed to find the average of stresses at all possible lattice orientations under a given strain while Reuss [57] suggested calculating the average of strains under a given stress instead. Equations 4.26 and 4.27 represent the bulk and shear modulus in the Voigt

definition, respectively. The same moduli in the Reuss definition are shown in Equations 4.28 and 4.29.

$$K_{\mathrm{V}} = \frac{1}{9}[C_{11} + C_{22} + C_{33} + 2(C_{12} + C_{13} + C_{23})] \tag{4.26}$$

$$G_{\mathrm{V}} = \frac{1}{15}[C_{11} + C_{22} + C_{33} + 3(C_{44} + C_{55} + C_{66}) - (C_{12} + C_{13} + C_{23})] \tag{4.27}$$

$$K_{\mathrm{R}} = [S_{11} + S_{22} + S_{33} + 2(S_{12} + S_{13} + S_{23})]^{-1} \tag{4.28}$$

$$G_{\mathrm{R}} = 15[4(S_{11} + S_{22} + S_{33} - S_{12} - S_{13} - S_{23}) + 3(S_{44} + S_{55} + S_{66})]^{-1} \tag{4.29}$$

where the subscripts *V* and *R* denote the Voigt and the Reuss notation and S_{ij} represents the components of the elastic compliance matrix obtained from the inverse of the elasticity matrix. Hill [58] showed that the actual shear and bulk modulus typically lie between the values estimated by Voigt and Reuss. Hence, the arithmetic mean of Voigt and Reuss values known as Voigt-Reuss-Hill (VRH) approximation can be expressed as:

$$K_{\mathrm{VRH}} = \frac{K_{\mathrm{V}} + K_{\mathrm{R}}}{2} \tag{4.30}$$

$$G_{\mathrm{VRH}} = \frac{G_{\mathrm{V}} + G_{\mathrm{R}}}{2} \tag{4.31}$$

The Molinari and VRH approximations require 4 and 9 out of 21 independent elastic constants, respectively. In each scheme, the neglected elastic constants are assumed to be zero, which is not the case for the crystals under study. In other words, the approximation scheme that includes more elastic constants leads to a higher accuracy in elastic properties estimation. Therefore, in this study, the VRH approximation is employed to characterize the elastic properties of the HCP phases. Once the VRH shear and bulk moduli are calculated, the average Young's modulus (*E*) and Poisson's ratio (*v*) for each crystalline phase can be calculated using the standard equations developed for isotropic materials:

$$E = \frac{9G_{VRH}}{3 + G_{VRH}/K_{VRH}} \tag{4.32}$$

$$\nu = \frac{3 - 2G_{VRH}/K_{VRH}}{6 + 2G_{VRH}/K_{VRH}} \tag{4.33}$$

4.3 Elastic Properties of HCP Phases

In the current study, MD simulations are performed on the main phases of the HCP. For this purpose, the crystalline structure of each phase is first constructed based on the most recent crystallographic data provided in Chapter 2. For each crystalline phase, simulation supercells are generated in three sizes of 1a×1b×1c, 2a×2b×2c, and 3a×3b×3c, in the *x*, *y*, and *z* direction, respectively. A three-dimensional periodic boundary condition [59] is assigned to each of the supercells before the simulation begins. The interactions among atoms are formulated using the COMPASS forcefield. To optimize the geometry of the atomistic models, an algorithm that combines the steepest descent, Quasi-Newton, and adjusted basis set Newton-Raphson (ABNR) methods is employed. In this study, the non-bonded energies are calculated by the Ewald summation method with the repulsive cut-off distance of 6 Å. The convergence of the analyses is verified by setting the Ewald accuracy equal to 0.0001 Kcal/mol. Following the geometry optimization, MD simulations are performed under the Gibbs (a.k.a., *NPT*) ensemble, which provides an isothermal, isobaric, and closed system, where the number of atoms (*N*), pressure (*P*), and temperature (*T*) are kept constant. The analysis time step is assumed equal to 1 fs (femtosecond, 10^{-15} s). The temperature and pressure of system is controlled using the Nose thermostat and the Berendsen barostat to meet the requirement of the desired room temperature (298 ˚K) and air pressure (1 atm or 0.0001 GPa). To ensure that the thermodynamic equilibrium is achieved in each simulation, a total analysis time of up to 200 ps (picosecond, 10^{-12} s) is considered while the convergence of a variety of parameters (e.g., total energy and its components, temperature, and pressure) is closely monitored.

The relaxed crystallographic lattice parameters of the phases under consideration have been summarized in Table 4-1. It has been found that the difference between the relaxed unit-cell parameters and the ones obtained from the experimental tests is always less than 4%. This shows that the selected forcefield is capable of reproducing the unit cell and the atomic arrangement of the main constituents of the HCP. It should be noted that since the Berendsen barostat is employed for the elastic properties calculations, the α, β, and γ angles are fixed and not allowed to change while the crystalline structures are relaxed. The MD relaxed structures are then used for the elastic properties calculations.

Based on the procedure introduced in the previous section, the elastic properties of all the relaxed crystalline structures of the main phases of the HCP have been obtained from MD simulations. This section summarizes the calculated elastic properties and provides a detailed comparison between the obtained results and the ones reported in the literature.

4.3.1 Portlandite

Among the phases under consideration, portlandite has the simplest crystalline structure and a number of simulation and experimental studies have been conducted to derive its elastic properties. In the category of numerical efforts, Laugesen [60] employed an ab initio method and estimated the bulk and shear modulus equal to 31.54 and 18.30 GPa, respectively. Manzano et al. [61] used the MM methods and obtained 31.10 and 13.40 GPa for the same parameters. The current study, which is based on MD simulations, calculates the bulk and shear modulus equal to 33.59 and 21.95 GPa, respectively. While the MD results are approximately 19% different from the ab initio and MM results, it is found that the estimates obtained from the experimental tests are much closer to the MD results compared to the other two methods. Brillouin spectroscopy [62, 63], compression of crystals in a diamond cell [64], and test of compacted powder samples of different porosities [65, 66] are the major experimental studies on portlandite. Based on the

previous Brillouin spectroscopy [62] and the compressive tests [64], Monteiro and Chang [67] calculated the Voigt, Reuss, Hill and Hashin-Shtrikman upper and lower bounds for the Young's modulus and Poisson's ratio of portlandite. Among all simulation efforts carried out on portlandite, MD simulations provide the most promising results as the percentage of difference between the most recent Brillouin spectroscopy estimates [63] and the ones obtained from MD simulations is less than 6% in all the four elastic properties reported in Table 4-2.

4.3.2 Crystalline Calcium Silicate Hydrates

The state of the knowledge about the atomic structure of the C-S-H gel has been obtained from the structural comparisons of the gel with the fully crystalline structures present in it. Tobermorite family and jennite belong to a wide family of crystalline calcium silicate hydrates. Due to the structural similarities with the C-S-H gel, these natural minerals have been widely used to model the C-S-H phase of HCP. The elastic properties of the tobermorite family, including tobermorite 9, 11, and 14 Å, are obtained from the MD simulations (Tables 4-3 through 4-5). To verify the accuracy of estimates, the comparisons are made with the results provided by three other studies: Manzano [68], Shahsavari et al. [69], and Dharmawardhana et al. [70]. In the listed studies, Manzano et al. (2009) used the MM methods; Shahsavari et al. (2009) employed the first-principles calculations using density functional theory (DFT) and GGA exchange correlation functionals; and Dharmawardhana et al. (2013) benefited from DFT based ab initio analyses. Pellenq et al. [71] also performed a classical potential energy minimization to characterize the Voigt and Reuss elastic properties of tobermorite 14 Å.

A review of results obtained from the MD method indicates that the percentage of difference is always less than 10%. This clearly highlights the capabilities of the conducted MD simulations in predicting the main elastic properties of the tobermorite family. Contrary to the simulation efforts, the experimental study on the tobermorite family is limited to Oh et al. [72].

This study utilizes high-pressure synchrotron XRD tests to determine the bulk modulus of tobermorite 14 Å. Among the studies listed for tobermorite 14 Å, the MD method proves to provide the closest estimation to the range of 47 ± 4 GPa given by Oh et al. [72] for the bulk modulus.

The MD results obtained for the crystalline structure of jennite are summarized in Table 4-6. Similar to the tobermorite family, Manzano [68], Shahsavari et al. [69], and Dharmawardhana et al. [70] are the main studies that utilize different atomistic simulation methods to investigate the elastic properties of jennite. A range of 31.83 to 62.65 GPa and 21.96 to 35.02 GPa has been given by the listed studies for the bulk and shear modulus of jennite, respectively. Based on the provided range, the estimates obtained from MD simulations can be considered acceptable as they are specifically very close to the most recent ab initio results reported by Dharmawardhana et al. [70].

Although there is an excellent agreement between the MD results and those obtained previously from ab initio, MM, and the XRD tests, the obtained elastic properties of the C-S-H crystals can be justified using the physic-chemistry parameters of these crystals. As the bond nature in all the simulated C-S-H crystals is similar, it is expected that the denser structures present the higher elastic properties in terms of bulk, shear, and Young's moduli. Moreover, as the W/Ca a ratio (W stands for the number of water molecules and Ca stands for the number of Ca ions in the unit cell) increases, the elastic properties of the crystal decrease. This is because the interlayer water molecules cover the Columbic interactions such that layers cannot affect the neighboring layers. The trends of these aspects for the main crystalline present in the C-S-H gel are shown well in Figures 4-1 and 4-2. Tobermorite 9 Å which is the densest phase with no water molecules in its structure, is therefore, the stiffest phase, whereas tobermorite 14 Å which has the least mass density and largest W/Ca a ratio has the least average elastic properties. Among the C-S-H phases, tobermorite 11 Å behaves slightly different compared with the other phases.

Tobermorite 11 Å is the only phase having double silica chains. In the double silica chains, the bridging Si atoms are surrounded by three silicon atoms where two of which are from interlayer while the third one is from either the upper or lower layer. The silicon arrangement creates strong 3D ion-covalent Si-O-Si bonds which link the adjacent layers in the interlayer direction. Thus, this strong 3D bond makes a closed network which can absorb a large number of water molecules without affecting the elastic behavior. Contrary to density and W/Ca ratio, the C/S ratio is found to have minimal effect on the mechanical properties of the C-S-H crystals. It should be noted that these relationships might not necessarily be linear as other structural factors might affect the elastic properties of crystalline phases.

4.3.3 Other hydration products

In addition to the portlandite and C-S-H components (i.e., tobermorite family and jennite), the elastic properties of ettringite, kuzelite, and hydrogarnet are calculated to provide a comprehensive MD study that includes the other phases of the HCP as well. The fact, however, is that there are very few atomistic simulation or experimental studies available in the literature on these three crystalline structures. As for ettringite, the elastic properties obtained from MD simulations can be compared only with the MM results reported by Manzano [68] and Brillouin spectroscopy predictions provided in Speziale et al. [73]. It can be understood from Table 4-7 that all the four elastic properties from MD simulations are in a better agreement with the experimental results of Speziale et al. [73] compared to the MM results reported by Manzano [68].

Finally, Tables 4-8 and 4-9 provide the elastic properties of kuzelite and hydrogarnet, respectively. While there is no experimental result available for the elastic properties of these two crystals, the atomistic simulation efforts are limited to the MM analyses conducted by Manzano [68]. A comparison between the MD and MM results indicates that the predicted values are fairly

close to each other for most of the elastic parameters. In the absence of experimental tests, the recommendation made by Haecker et al. [74] is also used to verify the accuracy of estimates. According to Haecker et al. [74], the mechanical properties of those cement paste crystals that have not been experimentally determined must be within the range of those that are already known. Based on this statement, the elastic properties of kuzelite and hydrogarnet should match the range of values suggested for the other crystalline structures of the HCP. This is verified by a comprehensive review of Tables 4-2 through 4-9.

4.4 Microporomechanical Properties of C-S-H

According to the hybrid model proposed by Jennings [15, 16, 17], the C-S-H gel at the micro-scale can be considered as a multiphase porous material, which contains dissimilar randomly distributed constituents in addition to the pores. Since each constituent of the C-S-H gel (i.e., tobermorites and jennite) has distinct structural characteristics, a separate effort is required to relate the mechanical properties of the C-S-H gel to the ones obtained for the individual constituents in the previous section. This can be achieved by taking into account the contribution of porosity through microporomechanical equations. For this purpose, the elastic properties of the C-S-H gel can be calculated using homogenization models. These models are able to rescale the properties of the individual crystalline phases of the C-S-H to those of the C-S-H itself considering a number of parameters that represent the solid phases and gel porosity. Depending on the size, shape, type, and inclusion distribution of composite materials, various homogenization models are available in the literature. Among them, two models of Self-Consistent (SC) and Mori-Tanaka (MT) have been proven to be appropriate for cement-based materials.

4.4.1 Self-Consistent Model

The Self-Consistent (SC) model estimates the average elastic properties of a multiphase porous material based on the mechanical properties of the spherical solid particles intermixed with the pores. This model was originally proposed for aggregate crystalline structures [75, 76] and later improved by Hill [77]. To obtain the bulk and shear modulus of the C-S-H gel using this model, the following two equations must be solved simultaneously:

$$K_{\mathrm{CSH}} = \frac{1}{\frac{1-\emptyset}{K_{\mathrm{solid}} + 4/3G_{\mathrm{CSH}}} + \frac{\emptyset}{4/3G_{\mathrm{CSH}}}} - \frac{4}{3G_{\mathrm{CSH}}} \tag{4.34}$$

$$\frac{(1-\emptyset)K_{\mathrm{solid}}}{K_{\mathrm{solid}} + 4/3G_{\mathrm{CSH}}} + \frac{5\emptyset\, G_{\mathrm{solid}}}{G_{\mathrm{CSH}} - G_{\mathrm{solid}}} + 2 = 0 \tag{4.35}$$

where $\emptyset$ is the gel porosity and the K_{solid} and G_{solid} are the bulk and shear modulus of the solid phase, respectively.

4.4.2 Mori-Tanaka Model

The Mori-Tanaka (MT) model was originally proposed to calculate the elasticity of a solid matrix with misfitting pore inclusions [78]. Benvensite [79] extended this model to composite materials with an inclusion phase, which consists of randomly or aligned ellipsoidal particles. According to this model, the effective bulk and shear modulus of the C-S-H gel can be estimated using the below equations:

$$K_{\mathrm{CSH}} = K_{\mathrm{solid}} \frac{4\, G_{\mathrm{solid}}(1-\emptyset)}{3K_{\mathrm{solid}}\emptyset + 4G_{\mathrm{solid}}} \tag{4.36}$$

$$G_{\mathrm{CSH}} = G_{\mathrm{solid}} \frac{(1-\emptyset)(8G_{\mathrm{solid}} + 9K_{\mathrm{solid}})}{6\emptyset(2G_{\mathrm{solid}} + K_{\mathrm{solid}}) + 8G_{\mathrm{solid}} + 9K_{\mathrm{solid}}} \tag{4.37}$$

The bulk and shear modulus calculated using the introduced homogenization models can be used to estimate the Young's modulus and Poisson's ratio of the C-S-H gel following Equations 4.32 and 4.33. While the K_{solid} and G_{solid} of various C-S-H constituents have been listed in Tables 4-2 through 4-5, the gel porosity, $\emptyset$, must be determined prior to utilizing the two models. Based on a comprehensive review of the gel porosity and packing density factors reported in the literature for the C-S-H (e.g., [80, 81, 21]), the porosity of the LD and HD types of the C-S-H gel has been assumed equal to 0.35 and 0.25, respectively. Figures 4-3 and 4-4 show how the elastic properties of the individual constituents of the C-S-H obtained from MD simulations can be related to the C-S-H gel itself. The effect of porosity on the strength of the C-S-H gel is evident considering the major drops observed in the Young's modulus of the C-S-H constituents originally calculated based on the VRH equations without considering the porosity. To verify the accuracy of estimates updated by microporomechanical equations, the final results are compared with the nanoindentation experiments conducted on the LD and HD C-S-H gels (e.g., [82, 83, 81, 84, 80, 21, 85]). Table 4-10 summarizes the Young's modulus of the C-S-H gel obtained from the nano-indentation studies. Considering the fact that the elastic properties reported by the listed studies are not necessarily consistent, their mean values (i.e., 20 and 30 GPa) are chosen for comparison purposes. From Figures 4-3 and 4-4, it can be seen that for all the four crystalline constituents of the C-S-H (i.e., tobermorite 9, 11 and 14 Å, and jennite), the Young's modulus is estimated closer to the experimental results using the SC model compared to the MT one. While a similar statement may not be entirely accurate for the Poisson's ratio, it can be noticed that the percentage of difference between the predicted Poisson's ratios is minimal. A review of results obtained for both LD and HD cases also indicates that tobermorite 14 Å and jennite can better mimic the expected mechanical properties of the C-S-H gel. As the C-S-H gel is known to resemble tobermorite 14 Å at an early stage and jennite later on, this confirms the earlier hypotheses that tobermorite 14 Å and jennite crystals are among the best C-S-H gel analogous [29].

Table 4-1 Comparison between the crystallographic lattice parameters of the HCP phases obtained from the experimental test and MD relaxation

Species		a (Å)	b (Å)	c (Å)	α (deg.)	β (deg.)	γ (deg.)
Portlandite	[35]	3.5853	3.5853	4.895	90	90	120
	MD	3.693	3.693	5.045	90	90	120
Tobermorite 9 Å	[32]	11.156	7.303	9.566	101.08	92.83	89.98
	MD	11.354	7.432	9.734	101.08	92.83	89.98
Tobermorite 11 Å	[32]	6.735	7.385	22.487	90	90	123.25
	MD	6.746	7.397	22.525	90	90	123.25
Tobermorite 14 Å	[33]	6.735	7.425	27.987	90	90	123.25
	MD	6.635	7.315	27.573	90	90	123.25
Jennite	[34]	10.576	7.265	10.931	101.30	96.98	109.65
	MD	9.777	6.716	10.105	101.30	96.98	109.65
Ettringite	[38]	11.167	11.167	21.354	90	90	120
	MD	10.217	10.217	19.537	90	90	120
Kuzelite	[39]	5.7586	5.7586	26.7946	90	90	120
	MD	5.7518	5.7518	26.7632	90	90	120
Hydrogarnet	[41]	12.565	12.565	12.565	90	90	90
	MD	12.760	12.760	12.760	90	90	90

Table 4-2 Elastic properties of portlandite

	MD	Other Methods
K (GPa)	33.59	31.1[a], 31.6 ± 0.3[b], 31.54[d], 39.65[e], 37.8[f]
G (GPa)	21.95	13.4[a], 20.9 ± 0.3[b], 18.3[d], 16.36[e]
E (GPa)	54.08	35.2[a], 51.4 ± 0.9[b], 40.3[c], 39.77-44.22[e], 48[g], 35.2[h]
ν	0.23	0.31[a], 0.23 ± 0.01[b], 0.305-0.325[e]

[a] **Manzano et al.** [61]
[b] **Speziale et al.** [63]
[c] **Constantinides and Ulm** [81]
[d] **Laugesen** [60]
[e] **Monteiro and Chang** [67]
[f] **Maede and Jeanloz** [64]
[g] **Wittmann** [66]
[h] **Beaudoin** [65]

Table 4-3 Elastic properties of tobermorite 9 Å

	MD	Other Methods
K (GPa)	70.88	78.09[a], 68.95[b], 71.42[c]
G (GPa)	45.64	43.18[a], 37.44[b], 37.18[c]
E (GPa)	112.72	109.39[a], 95.11[b], 95.06[c]
ν	0.23	0.27[a,b]

[a] **Dharmawardhana et al.** [70]
[b] **Manzano** [68]
[c] **Shahsavari et al.** [69]

Table 4-4 Elastic properties of tobermorite 11 Å

	MD	Other Methods
K (GPa)	64.40	77.19[a], 73.57[b], 66.65[c]
G (GPa)	35.24	40.42[a], 29.19[b], 32.03[c]
E (GPa)	89.40	103.25[a], 77.34[b], 82.82[c]
ν	0.27	0.28[a], 0.32[b]

[a] **Dharmawardhana et al.** [70]
[b] **Manzano** [68]
[c] **Shahsavari et al.** [69]

Table 4-5 Elastic properties of tobermorite 14 Å

	MD	Other Methods
K (GPa)	55.74	56.42[a], 47 ± 4[b], 44.80[c], 35.91[d], 20.7-35.4[e], 38.6[f]
G (GPa)	26.67	31.65[a], 19.00[c], 20.61[d], 2.78-5.08[e], 22.5[f]
E (GPa)	69.01	80.00[a], 49.94[c], 51.90[d], 63.5[e], 56.5[f]
ν	0.29	0.26[a], 0.31[c], 0.25-0.26[e]

[a] **Dharmawardhana et al.** [70]
[b] **Oh et al.** [72]
[c] **Manzano et al.** [61]
[d] **Shahsavari et al.** [69]
[e] **Pellenq et al.** [71]
[f] **Richardson and Groves** [23]

Table 4-6 Elastic properties of jennite

	MD	Other Methods
K (GPa)	64.09	62.65[a], 40.20[b], 31.83[c], 32.0[d]
G (GPa)	31.31	35.02[a], 22.10[b], 21.96[c], 19.9[d]
E (GPa)	80.77	88.56[a], 56.03[b], 53.55[c], 49.5[d]
ν	0.29	0.2752[a], 0.27[b]

[a] **Dharmawardhana et al.** [70]
[b] **Manzano et al.** [61]
[c] **Shahsavari et al.** [69]
[d] **Richardson and Groves** [23]

Table 4-7 Elastic properties of ettringite

	MD	Other Methods
K (GPa)	30.18	28.4[a], 27.3 ± 0.9[b]
G (GPa)	11.10	6.7[a], 9.5 ± 0.8[b]
E (GPa)	29.67	18.6[a], 25.0 ± 2[b]
ν	0.34	0.39[a], 0.34 ± 0.02[b]

[a] **Manzano** [68]
[b] **Speziale et al.** [73]

Table 4-8 Elastic properties of kuzelite

	MD	Other Method
K (GPa)	39.30	22.8[a]
G (GPa)	11.78	11.5[a]
E (GPa)	32.14	29.1[a]
ν	0.36	0.27[a]

[a] **Manzano** [68]

Table 4-9 Elastic properties of hydrogarnet

	MD	Other Method
K (GPa)	32.97	41.2[a]
G (GPa)	22.46	21.7[a]
E (GPa)	54.90	55.5[a]
ν	0.22	0.35[a]

[a] **Manzano** [68]

Table 4-10 Summary of the Elastic properties of the C-S-H gel reported in the literature

Author(s)	C-S-H Type	Gel Porosity (∅)	E (GPa)
Acker [86]	LD	-	20
	HD	-	31.6
Constantinides and Ulm [83]	LD	-	21.7 ± 2.2
	HD	-	29.4 ± 2.4
Hughes and Trtik [82]	Inner CSH	-	22.97
	Outer CSH	-	25.74
Constantinides and Ulm [81]	LD	0.37 ± 0.01	18.2 ± 4.2
	HD	0.24 ± 0.02	29.1 ± 4.0
Mondal et al. [85]*	LS	-	22.89
	MS	-	31.16
	HS	-	41.45
Zhu et al. [84]	LD	-	23.4 ± 3.4
	HD	-	31.4 ± 2.1
Jennings et al. [21]	LD	0.36	18.1 ± 4.0
	HD	0.26	31.0 ± 4.0
Vandamme et al. [80]	LD	0.32 ± 0.04	22.5 ± 5.0
	HD	0.26 ± 0.02	30.4 ± 2.9
	UHD	0.17 ± 0.01	40.9 ± 7.7

* *The authors classified C-S-H into three categories (LS: Low Stiffness; MS: Medium Stiffness; HS: High Stiffness). The LS and MS C-S-H correspond to the LD and HD C-S-H of the other studies, respectively.*

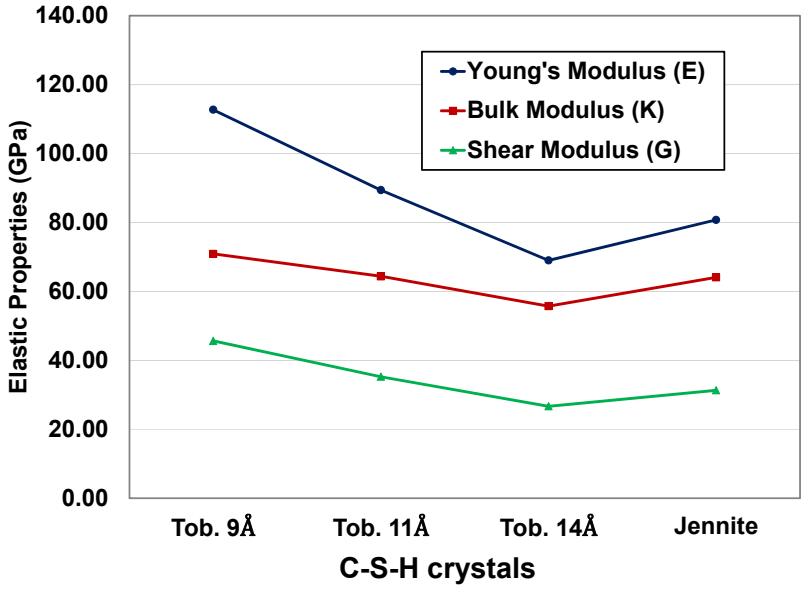

Figure 4-1 The elastic properties of the C-S-H components

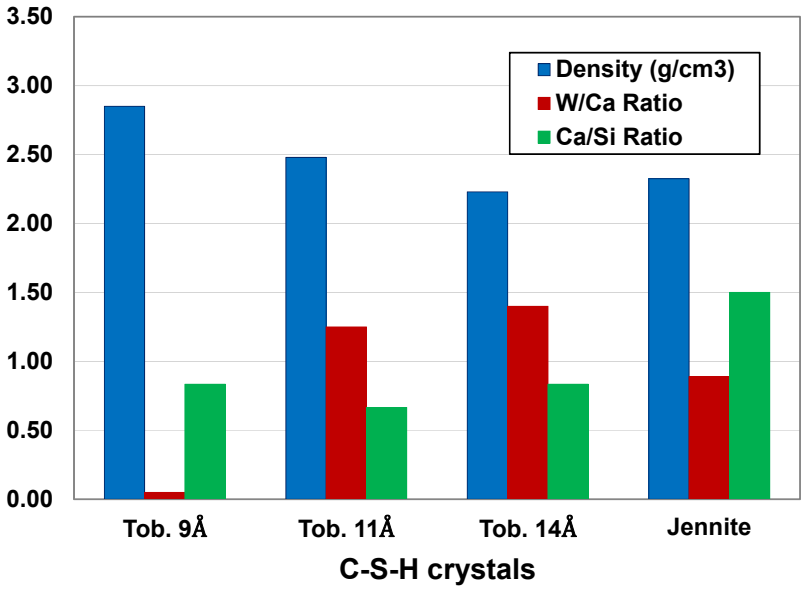

Figure 4-2 The physic-chemistry properties of the C-S-H components

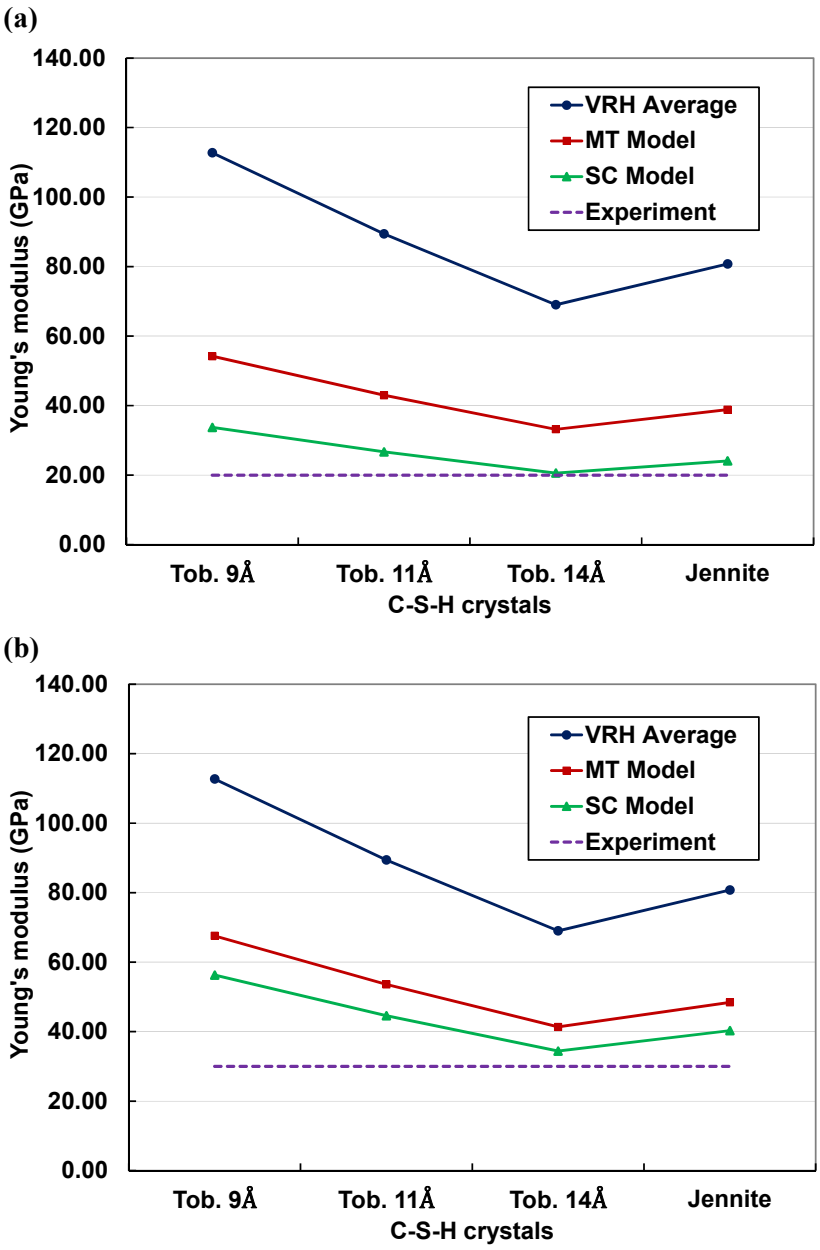

Figure 4-3 The Young's modulus of the (a) LD and (b) HD C-S-H gels estimated based on VRH equations, SC and MT models, and nanoindentation experiments

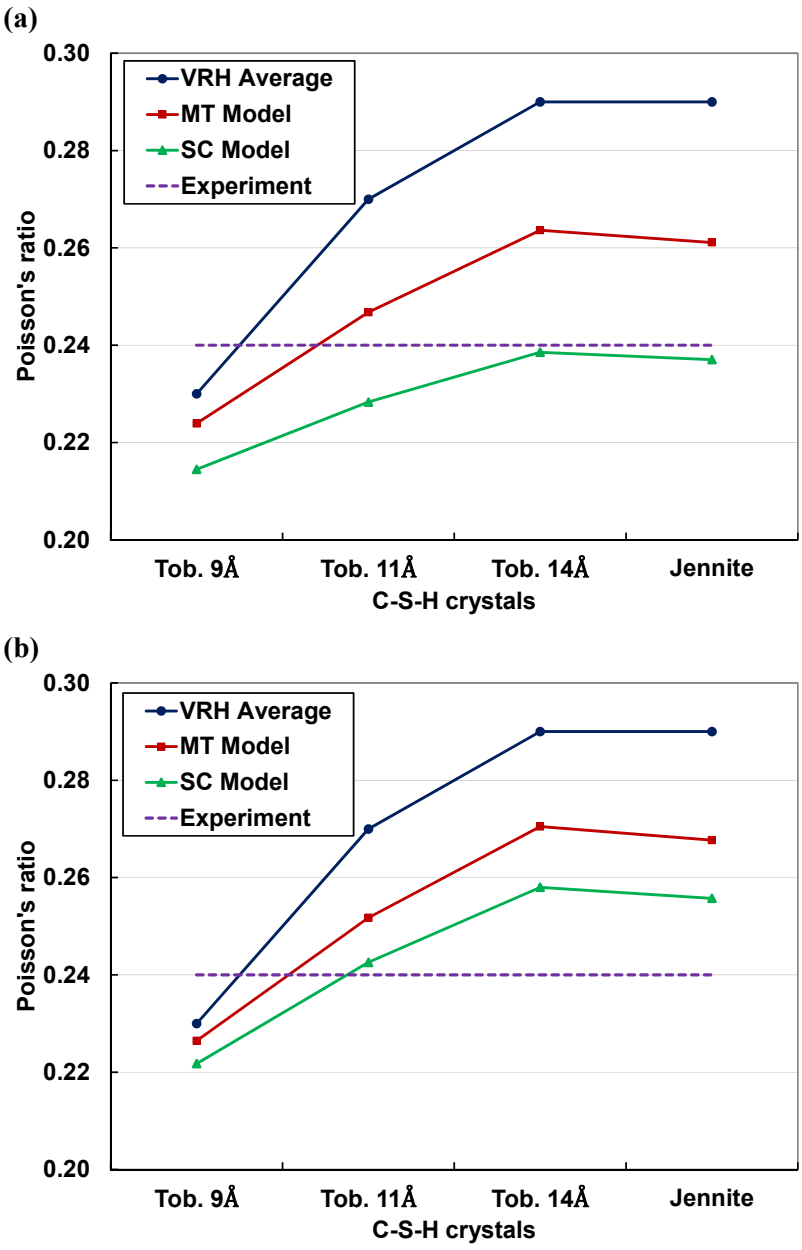

Figure 4-4 The Poisson's ratio of the (a) LD and (b) HD C-S-H gel estimated based on VRH equations, SC and MT models, and nanoindentation experiments

CHAPTER 5

CHARACTERIZATION OF STRESS-STRAIN BEHAVIOR

Although the macroscopic mechanical behavior of a material is an aggregate of characteristics unique to each length scale, in most cases the deformation within the constitutive building blocks play an important role in the overall behavior of material. Concerning hydrated cement paste for example, the development of creep and shrinkage is attributed to the deformation mechanisms of the C-S-H gel [87, 88]. Therefore, the mechanical characterization of materials at their building block scales is expected to provide a better insight about the correlation between the macroscopic mechanical behavior and the atomistic deformations. This chapter is focused on understanding the relation between the stress and strain induced in the HCP phases due to large atomistic deformations.

In the previous chapter, the elastic properties of crystalline phase of the HCP were characterized. To ensure an elastic response, the relaxed supercell of each HCP crystalline structure were subjected to very small deformations (e.g., 0.003 Å/Å). Although elastic property is an important aspect of engineering design, plastic behavior is also important to be evaluated as it provides invaluable information about the onset of permanent deformations and failure. As they are the best tool for engineers to interpret both elastic and plastic behavior of materials, the stress-strain diagrams are generated to characterize the mechanical behavior of the HCP phases under external loads. Similar to other materials, the stress-strain diagrams of the HCP phases at the nano-scale can be obtained by either experiments or simulations.

Determination of stress-strain behavior of single crystalline materials, like the individual HCP crystals, by experimental tests at the nano-scale is not an easy task. This is mainly due to the challenges involved with test data interpretation and ideal sample fabrication. For example, a nanoindentation experiment is capable of measuring nonlinear deformations. However, a priori

assumption of mechanical constitutive models to for example understand how material anisotropy evolves with loading is required to interpret the test data [89]. On the other hand, fabrication of such an ideal single crystal sample is a big challenge in experimental works. Perhaps it is due to the mentioned challenges that there is not any experimental work available in the literature to investigate the stress-strain behavior of the individual HCP crystals under external loads at the nano-scale. However, with recent advances in computational capabilities, it is now feasible to investigate the mechanical behavior of complex multi-atom crystals using large atomic models and atomistic simulation methods. Therefore, atomistic simulation is a valuable alternative tool to investigate the mechanical behavior of the HCP phases.

Atomistic simulation methods have been successfully employed to study the mechanical response of a wide range of materials, such as metals [90, 91], metallic glasses [92], silica glasses [93], biomaterials [94, 95, 96], and carbon nanotube [97, 98] under different loading conditions. However, for the mechanical behavior of cementitious materials, only two studies are available in the literature [99, 100]. Liu et al. [99] developed a first-principle-based reactive forcefield (ReaxFF) for a range of atoms including Ca, Al, H, O, and S. Using the developed ReaxFF, reactive molecular dynamics (RMD) simulations were carried out to understand the elastic, plastic, and failure response of the ettringite crystal at the atomic scale. Through the referenced study, the stress-strain curves were obtained for the uniaxial tension/compression in y- and z-direction. Manzano et al. [100] studied the mechanical response of the C-S-H gel under shear deformations. Two established models, tobermorite 14 Å and glassy C-S-H (gCSH) were used to simulate the ordered and disordered solid part of the C-S-H gel, respectively. Due to its denser structure, it was found that gCSH has higher elastic properties than tobermorite.

Considering the limited number of investigations available in the literature, there is an immediate need for a systematic study of the HCP phase's mechanical response under large deformations. To address this issue, the elastic, plastic, and failure behavior of all the HCP phases

are investigated at the nano-scale in this chapter. Since the MD method is based on the calculation of particle motions, it is well-suited to study the dynamics of forming permanent deformation, crack growth, and eventually fracture. However, because of the use of classical forcefields in this study, describing the chemical reactions within the fracture process is not provided. Therefore, one of the main assumptions in this study is rapid crack growth process which means cracks propagate with no interaction with the environment. Such an approach has been successfully applied to investigate the failure behavior of silica glass under tensile loading [93] as well as stress-strain behavior of polyethylene [101].

5.1 Relaxation Procedure

The MD simulations are conducted using the large-scale atomic/molecular massively parallel simulator (LAMMPS) package [102]. LAMMPS is an open-source program maintained and distributed by the researchers at the Sandia National Laboratories. The unitcells of the HCP crystals are constructed in LAMMPS using the latest crystallographic data available in the literature. The simulation supercells are generated from the unitcells of the HCP crystals extended in the three lattice directions. A three-dimensional periodic boundary condition [59] is assigned to each of the supercells before the simulation begins. Unlike the elastic properties characterization, the HCP crystals are subjected to large deformations for the stress-strain behavior study. Larger supercells are used to reduce the boundary effects and allow for greater degree of freedom for the structures such that the atomic displacements are not overly constrained by the periodic boundary conditions [95]. The supercells of tobermorite 9, 11, and 14 Å, jennite, hydrogarnet, ettringite, and kuzelite contain 4462, 8448, 9984, 4968, 4640, 4096, and 4770 atoms, respectively. It is notable that the large number of atoms used in this study ensures reliable simulation results from a statistical point of view. Using the ClayFF forcefield [52], the potential energy of each supercell is minimized at zero temperature to minimize the residual stresses. MD simulations are performed

in the isobaric-isothermal ensemble (*NPT*) for 10 ps at 300 ˚K and 0 atm with a time step of 0.5 fs. This provides a closed thermodynamics system, where the number of atoms (*N*), pressure (*P*), and temperature (*T*) are kept constant. During the MD simulations, the convergence of a variety of parameters (e.g., total energy and its components, temperature, and pressure) is closely monitored. During the equilibration stage, the long-range Coulombic interactions are calculated using the Ewald summation method with a cutoff radius of 12 Å. To ensure the thermodynamic equilibrium during the MD simulations, the convergence of a variety of parameters (e.g., total energy and its components, temperature, and pressure) is closely monitored. The procedure of minimizing the potential energy and reaching thermodynamic equilibrium is known as relaxing the atomic structure. To obtain a quantitative insight on the relaxed atomic structure of the HCP crystals, a Radial Distribution Function (RDF) analysis is performed. The RDF, $g_{\text{A-B}}(r)$, specifies the probability density function of finding the atom *B* at a distance *r* from the reference atom *A* averaged over the relaxed trajectories as expressed using the equation below:

$$g_{\text{A}-\text{B}}(r) = \frac{n_{\text{B}}}{4\pi r^2 dr} \Big/ \frac{N_{\text{B}}}{V_0} \tag{5.1}$$

where n_{B} is the number of *B* atoms located at a distance *r* from the atom *A* in a volume shell of thickness *dr*, N_{B} is the total number of *B* atoms in the system, and V_0 is the relaxed volume of the entire system. The outcome of the RDF analysis helps identify the chemical bond types present in the atomic structures of the HCP crystals. The mechanical characteristics of the HCP crystals under tensile strains are very much correlated to these chemical bonds that will be discussed in Section 5.3. The relaxed molecular structures of the HCP crystals are used for the stress-strain behavior characterization.

5.2 Uniaxial Tensile Straining

Contrary to conventional macro-scale experiments, it is often found more convenient to control strain rather than stress in atomistic simulations. The strain-control approach has been successfully applied to characterize the mechanical behavior of a wide range of materials [93, 94, 95, 99, 101]. To determine the stress-strain relationships in the HCP phases, the relaxed supercell of each phase is subjected to a range of uniaxial strains along one of the three orthogonal directions of *x*, *y* and *z*. During the gradual elongation, a constant strain rate of 10^{10} s^{-1} is applied to the supercell. The positions of atoms in the supercell are then fully relaxed to fit within new dimensions. To ensure capturing the Poisson's effect, the directions perpendicular to the one under external strain are allowed to relax anisotropically. This can be achieved by using the *NPT* equations of motion at zero pressure in the lateral directions. Along the straining direction, however, the pressure evolution is taken as internal stress. The straining process is repeated for all the three axes (*x*, *y* and *z*) and each time it continues until either a permanent failure occurs in the atomic structure or the target strain of 0.6 Å/Å is reached. The full set of stress and strain data of the HCP crystalline structures are used to generate the stress-strain curves for each straining direction. To better understand the obtained stress-strain curves, a comprehensive set of 1,000 strained structural configurations are recorded for further chemical bond and structural damage analysis. The Open Visualization Tool (OVITO) package is utilized to visualize the simulation results [103].

MD simulations provide valuable information about the dynamical trajectories that can be employed to explain the atomic bond breaking processes. As atomic bond breakage naturally reduces the strength, it is critical to investigate such processes thoroughly to understand the mechanical behavior of the HCP crystals, especially under the extreme strains. To this end, the average bond length is computed for all the bonds that exist in the supercells. The bonds that can potentially take up the applied strain are then identified through the constant monitoring of the

changes in the bond length. Such comprehensive bond analysis provides invaluable information about the bond types that resist against the applied strain. Moreover, the dynamical trajectories can be used to determine the causes of damage in the atomic structures of the HCP crystals under tensile strains. This is carried out by visualizing the atomic structures, and monitoring the changes in the position and orientation of atoms at each time step. The permanent changes in the atomic structures of the HCP crystals are identified and used to infer the damage formation processes. The outcome of chemical bond and structural damage analysis can be used to fully characterize the structural response and failure mechanisms of the HCP crystals under uniaxial tensile strains.

5.3 Stress-Strain Relationships

With the methodology described in Sections 5.1 and 5.2, the stress-strain curves of the HCP crystals are obtained and discussed in this section. The effect of the straining direction on the stress-strain curves of the HCP crystals is also investigated. Bond analysis is carried out to identify the chemical bonds that resist against tensile strains. Furthermore, the stress-strain behavior captured with the MD simulations is correlated to the evolution of damage in the atomic configuration of the HCP crystals during deformation. The outcome of the chemical bond and structural damage analysis is used to identify the failure mechanisms of the HCP crystals subjected to tensile strain in different directions. Characterization of mechanical properties of the HCP phases will be discussed in Section 5.4.

5.3.1 Tobermorite 11 and 14 Å

Figure 5-1 shows the total and partial radial distribution functions (RDFs) for the relaxed structures of the tobermorite 11 and 14 Å crystals. The RDFs clearly reveal that the tobermorite 11 and 14 Å crystals have similar structural features. It can be seen in this figure that the two distinct peaks in the total RDFs, which occur at ~ 1.6 and 2.7 Å, are originated from the covalent

Si-O and Ca-O bonds, respectively. The relaxed structures of tobermorite are used for the stress-strain characterization. The stress-strain curves of the tobermorite 11 and 14 Å structures under uniaxial tensile strains in the *x*, *y* and *z* directions are presented in Figure 5-2, which represents three sets of data corresponding to the calculated σ_{XX}, σ_{YY}, and σ_{ZZ} for each tobermorite structure. It can be observed from the stress-strain curves that the tobermorite structures show different mechanical behavior (in terms of strength, stiffness, and failure mechanisms) under different straining conditions. The initial portion of all the curves is approximately linear, which describes an elastic behavior as stress increases linearly with strain. Beyond the elastic portion, there is an onset of nonlinearity corresponding to the plastic behavior in which stress either instantaneously drops after the maximum stress is reached or increases slowly with increasing strain representing a hardening behavior followed by an abrupt drop to zero. The first case is called brittle behavior while the second one is referred to as a ductile behavior. The stress-strain behavior of tobermorite 11 and 14 Å in different directions is discussed in more detail below.

5.3.1.1 In *x* and *y* Directions

The stress-strain curves of tobermorite 11 and 14 Å show similar behavior under uniaxial tensile strains in the *x* direction, although the ultimate stress and the strain at failure for the two tobermorite structures are slightly different. The ultimate stress of tobermorite 11 Å is 2.4 GPa at the strain of 0.08. In Tobermorite 14 Å, the ultimate stress decreases to 2.3 GPa and occurs at the strain of 0.09. For both tobermorite structures, the drop in the stress-strain curve in the *x* direction can be mainly related to the breakage of the Ca-O bonds. As mentioned earlier, the calcium oxide layers in tobermorite structures are present in the *x*-*y* plane. Since the silicate tetrahedra chains are running along the *y* direction, the Si-O bonds have no major contribution to resisting the strain applied in the *x* direction. This fact can be confirmed from Figure 5-3, which shows the average Ca-O and Si-O bond length as a function of strain along the *x* direction. It can be observed in this

figure that the Ca-O plot has a shape similar to the stress-strain curves obtained for both tobermorite structures. On the other hand, the Si-O plots of tobermorite crystals remain relatively flat reflecting no significant changes in the Si-O bond length.

For tobermorite 11 and 14 Å under uniaxial strain in the *y* direction, the fracture mechanism is brittle. The stress increases with strain up to the strain of 0.11 and then significantly drops. This brittle-like behavior is found to be due to the breakage of the Ca-O as well as Si-O bonds. Figure 5-4 shows the average Ca-O and Si-O bond length as a function of applied strain in the *y* direction. The recorded bond length data show that the applied strain in the *y* direction results in a constant increase in the Ca-O and Si-O bonds until the strain of 0.11 is reached, where the bonds start breaking. This indicates that in the *y* direction, the stretching of both Ca-O and Si-O bonds directly contribute to the mechanical behavior of the tobermorite 11 and 14 Å structures. Figure 5-5 shows that the energy of the Si-O bond is larger than that of the Ca-O bond in the tobermorite 11 and 14 Å structures. This fact highlights that the Si-O bonds have a stronger resistance to the tensile strain. This is why both tobermorite structures have a higher mechanical strength in the *y* direction than the *x* one. Figure 5-2 confirms this conclusion as the ultimate strength of tobermorite structures in the *y* direction is approximately three times larger than that in the *x* direction.

Between the two tobermorite structures under tensile strain in the *y* direction, tobermorite 11 Å with the ultimate stress of 8.2 GPa shows a relatively higher strength compared to tobermorite 14 Å, which has the ultimate stress of 6.8 GPa. This difference in the ultimate strength can be justified by taking into account the fact that the ratio of number of silicon to calcium atoms increases from 1.20 in tobermorite 14 Å to 1.50 in tobermorite 11 Å crystals. Considering the similarities in the structural response of tobermorites, Figure 5-6 shows the progress of formation of damage to the structure of tobermorite 11 Å under tensile strains in the *y* direction. At lower strains, there are no noticeable changes in the tobermorite's molecular

structure and an elastic response is recorded. However, when strain increases, particularly after the yield stress is reached, there are major changes in the position of calcium ions and the orientation of silicon tetrahedra. This is mainly due to the breakage of the Ca-O and/or Si-O bonds, which creates low-density regions inside the tobermorite's atomic structures. Subsequently, the calcium silicate layers may crack leading to the formation of local voids. As the straining process continues, the local voids propagate and coalesce along the interlayer of the tobermorite's structure. The void coalescence reduces the capacity of tobermorites accommodating the tensile strains and eventually results in a failure.

5.3.1.2 In *z* Direction

Contrary to the *x* and *y* directions, the mechanical behavior of tobermorite 11 Å is not similar to tobermorite 14 Å in the *z* direction. For tobermorite 11 Å strained in the *z* direction, the tensile stress reaches its peak at the strain of 0.07 and drops abruptly to zero exhibiting a brittle failure. Among the three orthogonal directions, tobermorite 11 Å shows its least ductility in the *z* direction. This is mostly due to the weak network of hydrogen bonds present in the interlayer of tobermorite 11 Å. Figure 5-7 illustrates the average changes in the energy due to the bond stretch and angle bend of water molecules under the external strain along the *z* direction. As can be seen from this figure, the breakage of hydrogen bond network leads to an abrupt drop in the H-bond energy of tobermorite 11 Å at a strain of 0.07. This is in a complete agreement with the brittle behavior found in the stress-strain curve. One of the distinct structural features of tobermorite 11 Å is that the bridging silicate tetrahedra are covalently bonded on both sides of the interlayer. On the other hand, the calcium atoms are covalently connected to the oxygen bonds of the silicate chains. Figure 5-8 shows the average changes in the Ca-O and Si-O bond length as a function of the applied strain. The bond analysis indicates that in tobermorite 11 Å, both Ca-O and Si-O bonds contribute to resisting against the tensile strains applied in the *z* direction. Figure 5-9

demonstrates the damaged atomic structure of tobermorite 11 Å under tensile strain in the z direction. As can be observed in this figure, the segregation between the calcium clusters is the main failure mode in the z direction of tobermorite 11 Å.

For tobermorite 14 Å, a gradual onset of failure characterizes the stress-strain curve under uniaxial tensile strains in the *z* direction. In this direction, the tobermorite 14 Å structure appears to yield at a tensile stress of 0.7 GPa corresponding to a strain of 0.08, before reaching the maximum stress of 0.75 GPa when it exhibits softening. Comparing the range of stresses recorded in three orthogonal directions indicates that tobermorite 14 Å has the lowest load bearing capacity in the *z* direction. This is mostly due to the existence of weak hydrogen bonds and the blockage of calcium ions in the interlayer of tobermorite 14 Å. The interlayer water molecules shield the Coulombic interactions in such a way that the interlayer calcium ions cannot affect the neighboring layers. Therefore, the binding energy of them is lower than those existing in calcium oxide layers (Figure 5-10). This phenomenon, however, does not occur in tobermorite 11 Å because the bridging silicon atoms are surrounded by three other silicon atoms. Two of these three silicon atoms are in the interlayer while the third one belongs to either the upper or the lower layer. Such an arrangement creates strong three-dimensional ion-covalent Si-O-Si bonds, which link the adjacent layers through a closed network that absorbs a large number of water molecules without affecting the overall mechanical behavior. Contrary to tobermorite 11 Å, the bridging silicate tetrahedra are not bonded on either side of the tobermorite 14 Å interlayer. Hence, the chemical bonds are not able to contribute to resisting against the tensile strains in the *z* direction. Figure 5-8 confirms this conclusion as it shows that increasing the tensile strain in the *z* direction results in no major changes in the length of the Ca-O and Si-O bonds. Figure 5-11 demonstrates the progress of damage to the structure of tobermorite 14 Å under tensile strain in the *z* direction. As shown in this figure, when the failure strain is reached, the interlayer of

tobermorite 14 Å is segregated. This failure mechanism was expected considering the interlayer condition of tobermorite 14 Å.

5.3.2 Tobermorite 9 Å and Jennite

Figure 5-12 presents the total and partial RDFs of the relaxed crystalline structures of tobermorite 9 Å and jennite. The RDFs indicate that tobermorite 9 Å and jennite have very similar structural features. The total RDF curves fluctuate as the radius increases and they form a few peaks in the short and long ranges. The total RDF curves eventually tend to approach 1.0 as expected. Comparing the total and partial RDFs reveals that the two distinct peaks in the short range of the total RDFs, which occur at approximately 1.6 and 2.6 Å, are originated from the covalent Si-O and Ca-O bonds, respectively. The relaxed structures of tobermorite 9 Å and jennite are subjected to tensile strains in the *x*, *y* and *z* directions to obtain the stress-strain curves.

5.3.2.1 In *x* Direction

The stress-strain curves of tobermorite 9 Å and jennite subjected to uniaxial tensile strains in the *x* direction are presented in Figure 5-13. For tobermorite 9 Å, a brittle behavior characterizes the stress-strain curve. The tensile stress quickly reaches its maximum value at a strain of 0.06 Å/Å and then approaches to zero as strain increases. In contrast, the tensile stress in jennite increases until the strain of 0.13 Å/Å is reached and then reduces slowly with a constant slope. It is observed that the jennite crystalline structure cannot be stretched to fracture in the *x* direction even when the applied strain exceeds 0.60 Å/Å. This indicates that jennite, in the *x* direction, demonstrates a plastic behavior accommodating large axial deformations. The difference in the mechanical behavior of tobermorite 9 Å and jennite in the *x* direction can be further investigated using a detailed chemical bond and structural damage analysis.

Figure 5-14 shows the average Ca-O and Si-O bond lengths as a function of strain applied in the *x* direction of the tobermorite 9 Å and jennite structures. As can be seen in this figure, the strain at which the Ca-O bond breaks is 0.06 and 0.13 for tobermorite 9 Å and jennite, respectively. This is in a complete agreement with the stress-strain curves shown in Figure 5-13. Unlike the Ca-O bonds, the Si-O bond lengths show no changes as the strain increases. This can be justified based on the fact that the existing silicate tetrahedra run along the *y* direction in both tobermorite 9 Å and jennite crystals. Figure 5-15 demonstrates the structural changes of tobermorite 9 Å under the tensile strain in the *x* direction. At the elastic range, the calcium silicate layers are elongated in the *x* direction, which is mainly due to the breakage of the Ca-O bonds. This type of breakage creates low-density regions that propagate along the *z* direction and eventually form large voids. As the applied strain increases, the large voids are coalesced, two apparent fracture surfaces are created, and the structure completely collapses at the strains larger than 0.45 Å/Å. Such a fracture mechanism can fully support the brittle behavior observed in the stress-strain curve of tobermorite 9 Å in the *x* direction.

Concerning the jennite's atomic structure, it is found that the breakage of the Ca-O bonds creates similar low-density regions as were observed in tobermorite 9 Å. However, the low density regions in jennite do not tend to propagate in the *z* direction, and as a result, the large voids are never seen. The reason for this situation is the existence of a weak hydrogen bond network in the interlayer of the jennite structures, which do not resist against the contraction forces expected due to the Poisson's effect. This phenomenon does not occur in tobermorite 9 Å since there are no water molecules in the unit cell of tobermorite 9 Å. Considering that the algorithm used in this study allows for anisotropic relaxations of the simulation cell in the directions perpendicular to the direction of straining, the evaluation of the effects of hydrogen bonds on the lateral displacements has become possible.

Figure 5-16 shows the lateral strains (ε_Y and ε_Z) as a function of uniaxial strain in the *x* direction for the both tobermorite 9 Å and jennite crystalline structures. As can be seen in this figure, the maximum lateral strain in the *z* direction of jennite is ten times larger than that for tobermorite 9 Å. This indicates a major contraction in the *z* direction of the jennite structure as a result of the strain applied in the *x* direction. The significant shrinkage of the simulation cell in the *z* direction densifies the calcium silicate layers, which effectively prevent the void coalescence and consequent fracture. It is notable that for both tobermorite 9 Å and jennite, the magnitude of the lateral strain in the *y* direction is very small compared to that in the *z* direction. This is mainly due to the presence of strong silicate chains, which provide significant resistance against contraction. To visualize the formation and distribution of voids, the recently developed surface reconstruction method [104] is utilized for various uniaxial strains. For this purpose, a polyhedral mesh is constructed around the solid particles as can be seen in Figure 5-17 for the jennite's atomic structure. It can be clearly seen that the side length shrinks significantly in the *z* direction as the applied strain in the *x* direction increases. Furthermore, unlike tobermorite 9 Å, the small voids are formed and distributed randomly throughout the cross-section such that the void coalescence and fracture does not occur even at the 0.60 Å/Å strain level.

5.3.2.2 In *y* Direction

The stress-strain curves of tobermorite 9 Å and jennite under uniaxial tensile strain in the *y* direction are presented in Figure 5-18. In this direction, a brittle behavior characterizes the stress-strain curves of both crystalline structures. The tensile stress reaches its maximum value when the applied strain exceeds 0.10 Å/Å. It can be seen that the maximum tensile strengths of tobermorite 9 Å and jennite in the *y* direction are 9.4 and 5.2 GPa, respectively, which are approximately three times larger than the same quantities in the *x* direction. The tensile strength improvement in the *y* direction can be justified through a detailed bond analysis. Figure 5-19

demonstrates the average covalent Ca-O and Si-O bond lengths as a function of applied tensile strain in the *y* direction. The plots of bond length versus uniaxial strain are all very similar to the stress-strain plots shown in Figure 5-18. As can be seen in Figure 5-19, the Ca-O and Si-O bonds extends with the increase in the applied strain until they break catastrophically at a strain of 0.11 and 0.12 Å/Å for tobermorite 9 Å and jennite, respectively. Since the Si-O bond is stronger than the Ca-O bond, the combined contribution of the Si-O and Ca-O bonds naturally results in a larger tensile strength capacity in the *y* direction compared to that in the *x* direction.

The stress-strain curves and bond analysis reveals that although tobermorite 9 Å and jennite have similar type of mechanical behavior under the tensile strain in the *y* direction, the tensile strength of tobermorite 9 Å is almost twice as that of jennite. This significant difference in the tensile strengths can be justified by the fact that the Si/Ca ratio in the unit cell of tobermorite 9 Å is 1.20, while that ratio in the unit cell of jennite is only 0.67. This clearly highlights the role of Si-O bonds present in the molecular structure of tobermorite 9 Å to resist the applied tensile strain. The structural damage analysis can provide a more detailed insight on the physicochemistry of the process of damage formation in the *y* direction. Figure 5-20 displays the damaged structure of tobermorite 9 Å and jennite subjected to tensile strain in the *y* direction. It can be observed from this figure that both crystalline structures have experienced similar type of damage under the tensile strain in the *y* direction. At lower strains, in which an elastic response is recorded, there are no observable changes in the molecular structures of tobermorite 9 Å and jennite. However, when strain increases, particularly after the ultimate stress is reached, there are noticeable changes in the position of the calcium atoms and the orientation of the silicon tetrahedra. This is mainly due to the breakage of the Ca-O as well as Si-O bonds. A sequential breaking of the chemical bonds results in the formation of a few large voids. As the tensile strain further increases, the large voids coalesce, which leads to the segregation between the calcium

silicate layers. This situation majorly reduces the tensile strength of tobermorite 9 Å and jennite crystals and eventually causes structural failure.

5.3.2.3 In *z* Direction

Figure 5-21 presents the stress-strain curves of tobermorite 9 Å and jennite under uniaxial tensile strain in the *z* direction. For both tobermorite 9 Å and jennite, a brittle behavior characterizes the mechanical behavior in the *z* direction. In tobermorite 9 Å, the tensile stress gradually increases up to the ultimate stress of 2.3 GPa before a sudden failure occurs. For jennite in the *z* direction, the maximum tensile stress of 1.0 GPa takes place at a strain of 0.1 Å/Å before a drop to zero is observed. Figure 5-22 shows the lateral strains as a function of uniaxial tensile strain in the *z* direction. The obtained lateral strains are found well consistent with the stress-strain curves of tobermorite 9 Å and jennite. It is noted that the lateral strains are substantial in the *x* direction. In contrast, the lateral strains in the *y* direction are small in both crystalline structures mainly because of the strong silicate tetrahedra chains running along the *y* direction. This situation highlights the fact that the calcium polyhedra layers play an important role in resisting the tensile strain in the *z* direction. The structural damage analysis provides a more detailed insight in this regard.

As mentioned earlier, the atomic structures of tobermorite 9 Å and jennite have layers perpendicular to the *z* direction. The interlayer space of both tobermorite 9 Å and jennite is filled with calcium polyhedra. As can be seen in Figure 5-23, the segregation between the interlayer calcium clusters is the main cause of fracture in both tobermorite 9 Å and jennite under uniaxial tensile strain in the *z* direction. It is critical to note that jennite shows a weaker mechanical behavior in the *z* direction compared to tobermorite 9 Å. This is mostly due to the existence of the hydrogen bonds and the calcium polyhedra in the interlayer of jennite. The interlayer water molecules tend to block the Columbic interactions in such a way that the interlayer calcium ions

cannot interact with the neighboring layers. This situation adversely affects the tensile capacity of jennite in the *z* direction.

5.3.3 Hydrogarnet, Ettringite, and Kuzelite

In mature cement paste, a considerable amount of hydrogarnet, ettringite, and kuzelite exists that are formed at different stages of the hydration process of highly reactive tricalcium aluminate (C_3A) [8]. During the hydration process in cementitious materials, such as concrete and mortar, C_3A reacts with water rapidly, and as a result, calcium hydroaluminate phases, also known as hydrogarnet, is formed [9]. This reaction is not desired as hydrogarnet induces rapid stiffening and adversely affects the workability of cement paste. To avoid this situation, retardants such as gypsum are usually added to cement clinkers to help reduce the rate of the reaction of C_3A and water. Gypsum is highly soluble and releases calcium and sulfate ions into the pore solution. The presence of sulfate ions causes C_3A to undergo a different chemical reaction, which produces calcium trisulfoaluminate phases, also called mineral ettringite. If gypsum is completely consumed before C_3A, the concentration of sulfate ions decreases drastically, C_3A starts consuming ettringite, and different solid phases with fewer sulfates are formed. As a result of such reactions, kuzelite is produced [8]. However, if a new source of sulfate ions become available (from ground water, sea water, or soil), it will be thermodynamically favorable to form ettringite again, just as it was initially, through the consumption of the existing kuzelite [11]. In this case, since the replacing ettringite occupies a larger volume than the original kuzelite, expansive stresses are created, which may cause undesirable cracking and deterioration of cementitious materials [10]. Hence, the permeability of C_3A to water and its reactions with other chemical species during cement hydration results in the formation of the hydrated products, which affect the structural evolution and mechanical properties of the cement paste. To help settle the mechanical issues, it is essential to understand

the atomistic processes involved when each of the C_3A hydrated phases goes under mechanical loads. The stress-strain behavior of hydrogarnet, ettringite, and kuzelite is presented and discussed below.

5.3.3.1 Hydrogarnet

Hydrogarnet has a cubic unit cell with identical structural features in the three orthogonal directions. Because of the high symmetry present in the structure of hydrogarnet, the octahedral chains of $[Al(OH)_6]^{3-}$ and divalent Ca^{2+} are uniformly distributed in the x, y, and z directions. This indicates that the mechanical behavior of hydrogarnet does not depend on the direction of applied strain. The stress-strain behavior of hydrogarnet in response to uniaxial tensile strains is shown in Figure 5-24. It can be observed that the tensile stress increases with strain and reaches its maximum of 1.5 GPa at a strain of 0.08 Å/Å. After the ultimate stress is reached, tensile stress drops, which exhibits softening. This stress-strain behavior can be further investigated by monitoring the average change of bond length as the applied tensile strain increases.

Figure 5-25 shows the total and partial radial distribution functions (RDFs) of the relaxed structure of hydrogarnet. The two distinct peaks at 2.0 and 2.65 Å in the total RDF originate from covalent Al-O and Ca-O bonds, respectively. The Al-O and Ca-O bonds are found as the most prominent chemical bonds in the molecular structure of hydrogarnet and need to be considered for chemical bond analysis. Figure 5-26 demonstrates the average Ca-O and Al-O bond length as a function of applied tensile strain. The chemical bond-strain curves have a shape similar to the stress-strain curve of hydrogarnet. It can be observed from the figure that at lower strains the chemical bonds are stretched to take up the applied strain. They, then, suddenly break after reaching their peak length. This implies that the breakage of the Ca-O and Al-O bonds is responsible for mechanical failure of hydrogarnet.

5.3.3.2 Ettringite

Unlike hydrogarnet, the mechanical behavior of ettringite is noticeably dependent upon the direction of applied tensile strain. This is due to the fact that the structural features of ettringite in the *x*/*y* direction are different from those in the *z* direction. The stress-strain behavior of ettringite subjected to tensile strain in the *x*/*y* and *z* direction is presented in Figure 5-27. It can be observed that the stress-strain curves of ettringite in the *x*/*y* and *z* directions have relatively similar shape. The differences, however, are the magnitude of ultimate stress, ultimate strain, and the failure strain. In the *x*/*y* direction the ultimate stress of 2.5 GPa occurs at a strain of 0.13 Å/Å, and drops to zero at a strain of 0.27 Å/Å. On the other hand, the ultimate stress of 2.9 GPa occurs at a strain of 0.10 Å/Å in the *z* direction, which represents higher mechanical strength compared to that in the *x*/*y* direction. In this direction, the normal stress reaches zero at a strain of 0.18 Å/Å, which exhibits mechanical failure. The stress-strain behavior found in different directions can be further discussed using chemical bond analysis.

The total and partial RDFs of the relaxed structure of ettringite are presented in Figure 5-28. It can be observed that, neglecting the weak hydrogen bonds of water molecules and hydroxyl groups, i.e., the first distinct peak at ~ 1.0 Å of the total RDF, the S-O, Al-O, and Ca-O bonds are the most prominent chemical bonds in the structure of ettringite. The chemical bonds mentioned above are considered for chemical bond analysis. Figure 5-29 shows the average S-O, Al-O, and Ca-O bond lengths as a function of applied tensile strain in the *x*/*y* and *z* direction. It can be observed that the length of the covalent Al-O and Ca-O increases by increasing the applied tensile strain and drops to the equilibrium length at a strain of 0.27 and 0.18 Å/Å in the *x*/*y* and *z* direction, respectively. This behavior matches with the stress-strain curves obtained for ettringite. Unlike the Al-O and Ca-O bonds, the S-O bond length do not undergo a significant change in both strain directions reflecting the minimal contribution of the S-O bonds in resisting tensile strains.

Bond analysis helped identify the structural elements that resist against the applied tensile strain. However, a more detail investigation about the failure mechanism in different directions is still needed. This can be carried out by monitoring the damage process in the atomic structure of ettringite. Figure 5-30 shows the progress of the formation of damage to the structure of ettringite under tensile strains in the *z* direction. At lower strains, there are no noticeable changes in the ettringite's molecular structure and an elastic response is recorded. However, when strain increases, particularly after the yield stress is reached, there are major changes in the position of divalent calcium and trivalent aluminum ions. This is mainly due to the breakage of the Ca-O and Al-O bonds, which creates local voids inside the ettringite's atomic structures. As the straining process continues, the local voids propagate and coalesce, which form a large crack perpendicular to the direction of straining. The formed crack grows as the applied strain increases, which leads the C_3A columns to break into two halves. This makes the C_3A columns lose their original structural form after the molecular structure of ettringite is completely collapsed. In the *x*/*y* direction, the SO_4^{-2} groups and water molecules are located at the interstitials between the C_3A columns that provide structural stability to columnar conformation. Considering the similarities in the structural response of ettringite in the *x* and *y* directions, Figure 5-31 shows the progress of formation of damage to the structure of ettringite under tensile strains in the *x* direction. As can be seen in the figure, after the Al-H_2O and Ca-H_2O interactions are lost, the weak network of hydrogen bonds is broken. This results in a separation of the C_3A columns and forms a large crack along the *z* direction. As the straining process continues, the crack grows and the molecular structure of ettringite breaks into two halves that are pulled away from one another causing mechanical failure.

5.3.3.3 Kuzelite

Similar to ettringite, the mechanical behavior of kuzelite depends considerably on the direction of straining. Figure 5-32 shows the stress-train curves of kuzelite under tensile strain in the *x*/*y* and *z* directions. In the *x*/*y* direction, the ultimate stress of 1.6 GPa occurs at a strain of 0.05 Å/Å and the stress reaches to zero at a strain of 0.26 Å/Å. The ultimate stress of 2.8 GPa at a strain of 0.12 Å/Å indicates a higher mechanical strength in the *z* direction. In this direction, the tensile stress decreases as the applied strain increases until it reaches zero at a strain of 0.43 Å/Å. Neglecting hydrogen bonds, three major bond types, i.e., S-O, Al-O, and Ca-O bonds, are found from the total and partial RDFs of kuzelite as shown in Figure 5-33. The equilibrium length of the S-O, Al-O, and Ca-O bonds is 1.83, 2.00, and 2.65 Å, respectively. The chemical bonds mentioned above are considered for bond analysis. Figure 5-34 demonstrates the change in the length of the bonds distinguished from the RDFs of kuzelite as a function of applied tensile strain. It can be observed that for both *x*/*y* and *z* directions, the length of the Ca-O and Al-O increases as strain is increased while the S-O bond length remains relatively constant throughout the straining process. This implies that the Ca-O as well as Al-O bonds play a significant role in carrying tensile strains.

Kuzelite has a brucite-like layered structure, which consists of $[Ca_2Al(OH)_6]^+$ cations. The space between the layers is filled with the $\frac{1}{2}SO_4^{2-}.3H_2O$ groups that neutralize the charge of the system. As the bond analysis indicates, the S-O bonds do not contribute to resisting the tensile strain in *x*/*y* and *z* directions. Therefore, it can be concluded that the $[Ca_2Al(OH)_6]^+$ layers are responsible for mechanical behavior of kuzelite. Figure 5-35 shows the formation of damage in the structure of kuzelite in the *x*/*y* direction. The sequential breakage of the Ca-O and Al-O bonds results in the formation of local low-density regions. As the tensile strain increases, the low-density regions grow, coalesce, and eventually break the structure into two halves. This

significantly reduces the resistance against tensile strain and leads to a mechanical failure of the kuzelite structure. In the *z* direction, the Ca-O and Al-O bonds are stretched and form local voids in the $[Ca_2Al(OH)_6]^+$ layers (Figure 5-36). Strong Coulombic interactions between the $[Ca_2Al(OH)_6]^+$ layers and the sulfate groups, which provide structural stability in the *z* direction, resist against the applied tensile loads. This leads to higher ultimate tensile stress in the z direction compared to that in the *x*/*y* direction. Eventually after the applied tensile strain reaches a large value, the $[Ca_2Al(OH)_6]^+$ layer breaks into two halves and a mechanical failure occurs.

5.4 Characterization of Mechanical Properties

The stress-strain data obtained from MD simulations for the three orthogonal directions provide the information required to fully characterize the mechanical properties (e.g., Young's modulus, Poisson's ratio, and ultimate strength) of the HCP crystals. All the key mechanical properties can be extracted from the stress-strain curves presented in the previous section. Young's modulus (E) is a measure of material's stiffness, which can be quantified by the ratio of stress to strain along a specific axis as long as the Hooke's law holds. Ultimate strength (σ_U) is the maximum stress that a given material can withstand before it fails. Moreover, when a material is stretched in one direction, it tends to shrink in the other two directions perpendicular to the direction of elongation. Poisson's ratio (v) is the measure of this effect and can be defined by the negative gradient of the transverse to axial strain in the elastic regime. The Poisson's effect is captured in this study by allowing the supercells to relax anisotropically in lateral directions. The mechanical properties of the HCP crystals are presented and discussed below.

5.4.1 Tobermorite 11 and 14 Å

Table 5-1 summarizes the values of Young's modulus and ultimate strength of the tobermorite structures obtained from the stress-strain curves in the *x*, *y*, and *z* directions. It is

observed that in all the three orthogonal directions (i.e., *x*, *y* and *z*), tobermorite 11 Å has a higher stiffness than tobermorite 14 Å. The Young's modulus calculated from MD simulations ranges from 46.5 to 94.2 GPa and 9.5 to 74.7 GPa for the tobermorite 11 and 14 Å structures, respectively. Such a variation indicates the existence of a strong anisotropy in the mechanical properties of the tobermorite family.

To verify the accuracy of predictions, the values obtained for Young's modulus are compared with the values reported in the literature based on classical energy minimization [71, 68], ab initio [69, 70] and molecular dynamics [105] studies. While none of the previous studies has investigated the stress-strain behavior of tobermorites, their estimates of the Young's modulus are completely consistent with the average values calculated here based on the slope of the stress-strain curves. This is one of the important contributions of the current study as all the previous predictions of the Young's modulus had been obtained by averaging the elastic constants without taking into account the dependency of the elastic properties of tobermorites to the direction of straining. The ultimate strength of tobermorites under uniaxial tensile strains is also determined from the stress-strain curves. It is observed that both tobermorite structures have the highest tensile strength along the *y* direction. As discussed earlier, the stretching of both Ca-O and Si-O bonds is the main factor that results in a strong tensile resistance in the *y* direction.

The Poisson's ratios of the tobermorite structures for different strain and response directions are listed in Table 5-2. The range of the average Poisson's ratio of tobermorite 11 and 14 Å available in the literature is 0.27-0.32 and 0.25-0.31, respectively (Pellenq et al. [71]; Manzano [68]; Dharmawardhana et al. [70]; Hajilar and Shafei [105]). The Poisson's ratios extracted from the stress-strain curves are compared well with the literature. For tobermorite 11 and 14 Å, it is observed that the largest Poisson's ratios occur in the *z* direction and may reach up to 0.40 and 0.33, respectively. This is mainly because of the fact that the *z* direction is perpendicular to the hydrogen bonding network of the interlayer. Therefore, there is minimum

resistance to contraction. The situation, however, is different in the *x* and *y* directions as only small contractions are observed due to the existence of covalant Ca-O and Si-O bonds, which resist lateral deformations.

5.4.2 Tobermorite 9 Å and Jennite

In the absence of any experimental results, there are only four available atomistic simulation studies to evaluate the Young's modulus and Poisson's ratio of tobermorite 9 Å and jennite. Manzano [68] used the molecular mechanics (MM) method, Shahsavari et al. [69] and Dharmawardhana et al. [70] employed ab initio analyses, and Hajilar and Shafei [105] used MD simulations to estimate the elastic properties. It should be noted that the elastic properties reported in the previous studies were calculated from averaging the elastic constants. In the current study, however, the effect of straining direction is evaluated by characterizing the mechanical properties in the three orthogonal directions. Table 5-3 lists the Young's modulus and tensile strength of tobermorite 9 Å and jennite. The Young's modulus of tobermorite 9 Å and jennite varies from 16.02 to 104.33 GPa and from 12.56 to 56.45 GPa depending on the direction of interest. The Young's moduli obtained in this study from the MD simulations are highly consistent with the ones reported in the literature, especially in the strong direction. The ultimate tensile strengths of tobermorite 9 Å and jennite fall in the range of 2.3-9.4 and 1.0-5.2 GPa, respectively. There is no experimental test or simulation study available in the literature to compare the obtained ultimate stresses with.

Table 5-4 presents the Poisson's ratio of tobermorite 9 Å and jennite. As can be seen in this table, the Poisson's ratios calculated from MD simulations have a wide range, which indicates the sensitivity of them to the direction of straining. This is an important point as the average Poisson's ratios reported in the previous studies do not take into account the effect of straining direction. Moreover, it is observed that the largest Poisson's ratio may reach 0.50 in the

z direction in response to the tensile strains in the *x* direction. This can be attibuted to the fact that the *z* direction is perpendicular to the network of hydrogen bonds that exist in the interlayer. Therefore, there is only a minimum resistance to contraction in that direction. On the other hand, small contractions in the *y* direction can be justified with the presence of strong Ca-O and Si-O bonds.

5.4.3 Hydrogarnet, Ettringite, and Kuzelite

Table 5-5 summarizes the values of Young's modulus and ultimate strength of the hydrated phases of C_3A, i.e., hydrogarnet, ettringite, and kuzelite, obtained from the stress-strain curves. The Young's modulus of hydrogarnet does not depend on the direction of strain and is found equal to 27.1 GPa. The same parameter for ettringite and kuzelite ranges from 28.1 to 46.5 GPa and 29.9 to 30.4 GPa, respectively. To verify the accuracy of predictions, the values obtained for Young's modulus are compared with the values reported in the literature based on Brillouin spectroscopy [73], classical energy minimization [68], and molecular dynamics [106, 107] studies. While none of the previous studies has investigated the stress-strain behavior of hydrogarnet, ettringite, and kuzelite, their estimates of the Young's modulus are completely consistent with the average values calculated here based on the slope of the stress-strain curves. This is one of the important contributions of the current study as all the previous predictions of the Young's modulus had been obtained by averaging the elastic constants without taking into account the dependency of the elastic properties of the hydrated phases of C_3A to the direction of straining. The ultimate strength of the hydrated phases of C_3A under uniaxial tensile strains is also determined from the stress-strain curves. While the ultimate strength of hydrogarnet is independent of straining direction, it is observed that ettringite and kuzelite have their highest tensile strength along the *z* direction. As mentioned earlier, the stretching of Ca-O and Al-O bonds is the main factor that results in tensile strength of the hydrated phases of C_3A.

The Poisson's ratios of the hydrated phases of C_3A for different strains and response directions are listed in Table 5-6. The Poisson's ratios extracted from the stress-strain curves are compared well with the literature [73, 68, 106]. The Poisson's ratio of hydrogarnet is 0.30, while the same parameter for ettringite and kuzelite falls in the range of 0.21-0.44 and 0.25-0.34, respectively. Such a variation indicates the existence of a strong anisotropy in the mechanical properties of ettringite and kuzelite. For ettringite and kuzelite, it is observed that the largest Poisson's ratio may reach up to 0.44 and 0.34, respectively. Both crystals have positively charged features, C_3A columns in ettringite and $[Ca_2Al(OH)_6]^+$ layers in kuzelite, balanced by the SO_4^{2-} groups. Therefore, the cell parameters are expanded or contracted due to the strong Coulombic interactions.

Table 5-1 Mechanical properties of tobermorite 11 and 14 Å.

		x	y	z	Others
Tob. 11 Å	**E (GPa)**	46.5	94.2	65.4	89.4[a], 103.2[b], 77.3[c], 82.8[d]
	σ_U (GPa)	2.4	8.2	3.8	Not Available
Tob. 14 Å	**E (GPa)**	36.4	74.7	9.5	69.0[a], 80.0[b], 49.9[c], 51.9[d], 63.5[e]
	σ_U (GPa)	2.3	6.8	0.8	Not Available

[a] **Hajilar and Shafei** [105, 107]
[b] **Dharmawardhana et al.** [70]
[c] **Manzano** [68]
[d] **Shahsavari et al.** [69]
[e] **Pellenq et al.** [71]

Table 5-2 Poisson's ratio of tobermorite 11 and 14 Å.

		Tob. 11 Å			Tob. 14 Å		
		x	**y**	**z**	**x**	**y**	**z**
Strain Direction	**x**	-	0.14	0.08	-	0.16	0.28
	y	0.19	-	0.40	0.26	-	0.33
	z	0.07	0.28	-	0.09	0.02	-
Others		0.27[a], 0.28[b], 0.32[c]			0.29[a], 0.26[b], 0.31[c], 0.25-0.26[d]		

[a] **Hajilar and Shafei** [105, 107]
[b] **Dharmawardhana et al.** [70]
[c] **Manzano** [68]
[d] **Pellenq et al.** [71]

Table 5-3 Mechanical properties of tobermorite 9 Å and jennite.

		x	y	z	Others
Tob. 9 Å	**E (GPa)**	53.6	104.3	16.0	112.7[a], 109.4[b], 95.1[c], 95.1[d]
	σ_U (GPa)	2.9	9.4	2.3	Not Available
Jennite	**E (GPa)**	15.8	56.5	12.6	80.8[a], 88.6[b], 56.0[c], 53.6[d]
	σ_U (GPa)	1.5	5.2	1.0	Not Available

[a] **Hajilar and Shafei** [105, 107]
[b] **Dharmawardhana et al.** [70]
[c] **Manzano** [68]
[d] **Shahsavari et al.** [69]

Table 5-4 Poisson's ratio of tobermorite 9 Å and jennite.

		Tob. 9 Å			Jennite		
		x	**y**	**z**	**x**	**y**	**z**
Strain Direction	**x**	-	0.13	0.49	-	0.07	0.50
	y	0.23	-	0.18	0.24	-	0.35
	z	0.19	0.01	-	0.26	0.06	-
Others		0.23[a], 0.27[b,c]			0.29[a], 0.28[b], 0.27[c]		

[a] **Hajilar and Shafei** [105, 107]
[b] **Dharmawardhana et al.** [70]
[c] **Manzano** [68]

Table 5-5 Mechanical properties of hydrogarnet, ettringite, and kuzelite.

		x/y	z	Others
Hydrogarnet	**E (GPa)**	27.1		54.9[a], 55.5[b]
	σ_U (GPa)	1.5		Not Available
Ettringite	**E (GPa)**	28.1	46.5	29.7[a], 18.6[b], 25.0±2[c]
	σ_U (GPa)	2.5	2.9	Not Available
Kuzelite	**E (GPa)**	29.4	30.4	32.1[a], 29.1[b]
	σ_U (GPa)	1.6	2.8	Not Available

[a] **Hajilar and Shafei** [105, 107]
[b] **Manzano** [68]
[c] **Speziale et al.** [73]

Table 5-6 Poisson's ratio of hydrogarnet, ettringite, and kuzelite.

		Hydrogarnet		Ettringite		Kuzelite	
		y/x	**z**	**y/x**	**z**	**y/x**	**z**
Strain Direction	**x/y**	0.30	0.30	0.44	0.21	0.25	0.34
	z	0.30	-	0.42	-	0.29	-
Others		0.35[b]		0.34[a], 0.39[b], 0.34±0.02[c]		0.36[a], 0.27[b]	

[a] **Hajilar and Shafei** [106, 107]
[b] **Manzano** [68]
[c] **Speziale et al.** [73]

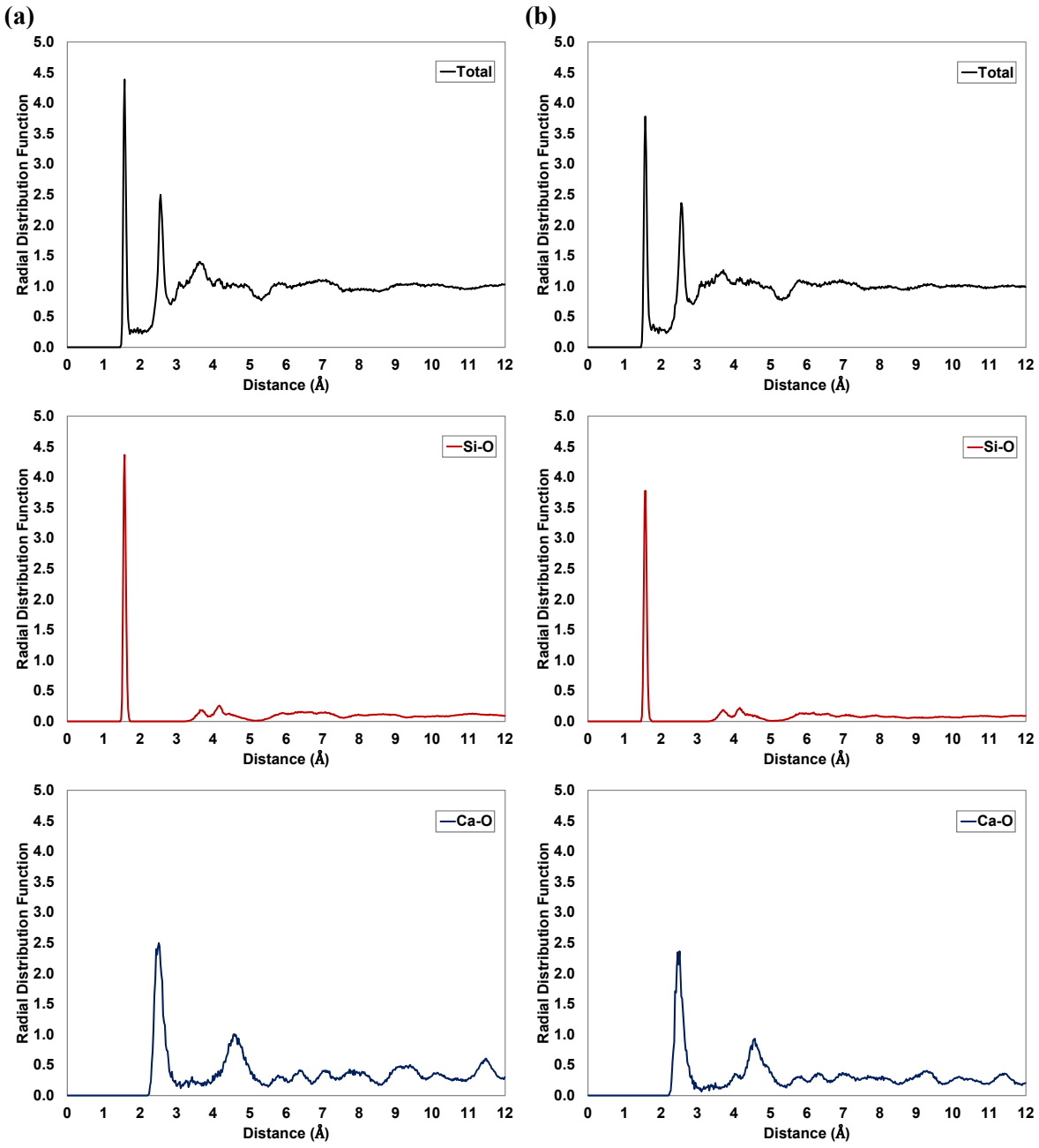

Figure 5-1 Total and partial radial distribution functions of (a) tobermorite 11 Å and (b) tobermorite 14 Å.

(a)

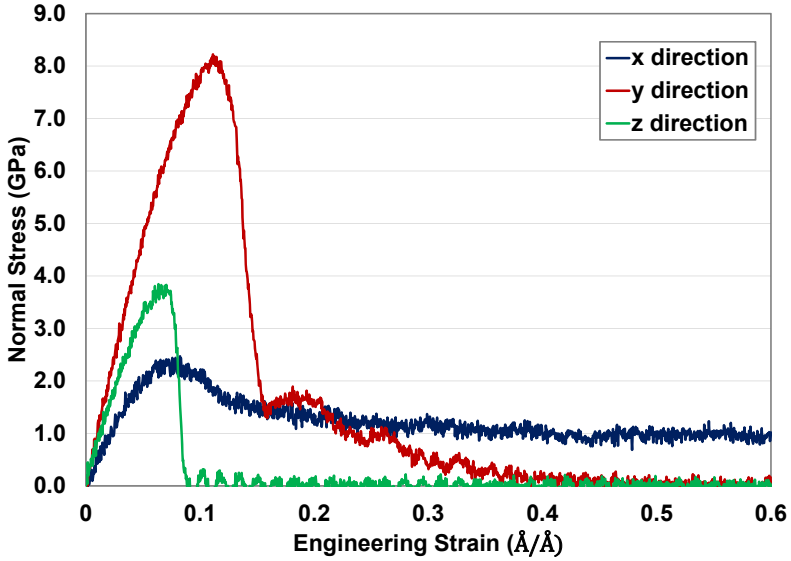

(b)

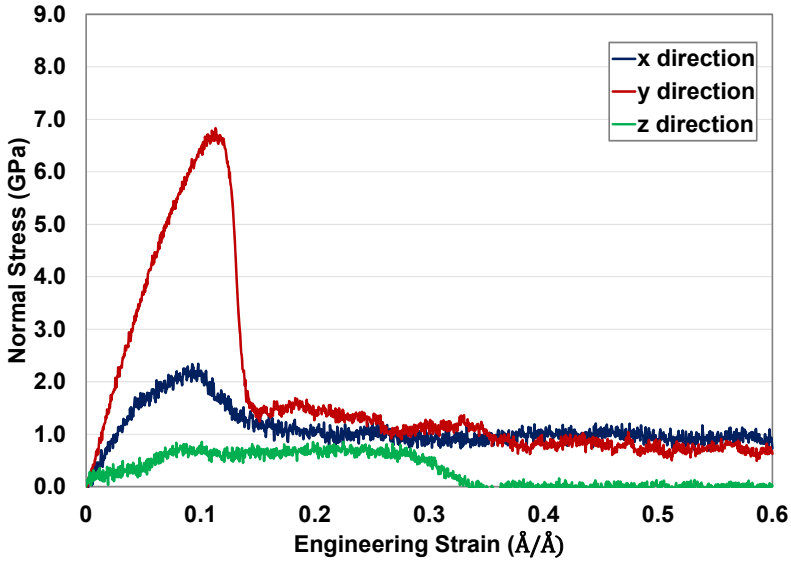

Figure 5-2 Stress-strain curves of (a) tobermorite 11 Å and (b) tobermorite 14 Å under uniaxial tensile strain along the *x*, *y*, and *z* direction.

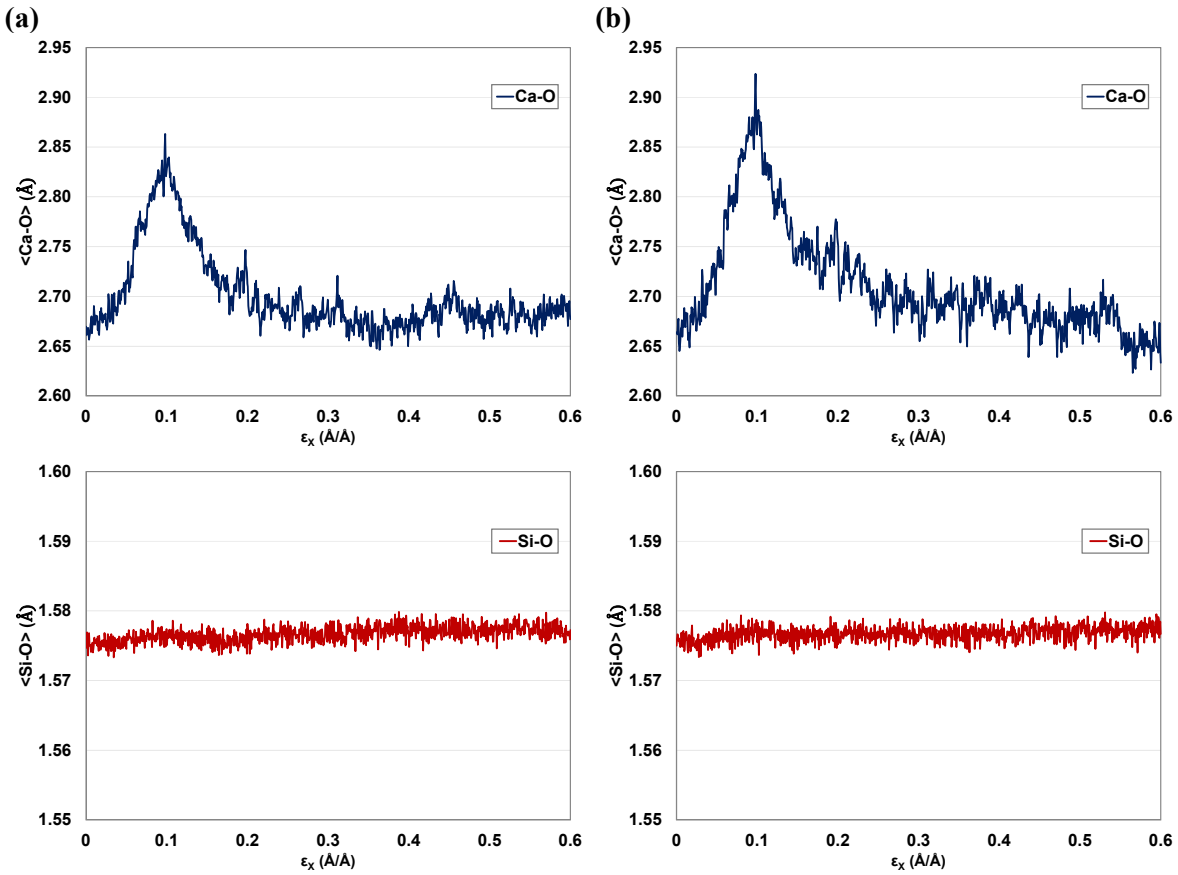

Figure 5-3 Average bond length as a function of strain along the *x* direction of (a) tobermorite 11 Å and (b) tobermorite 14 Å.

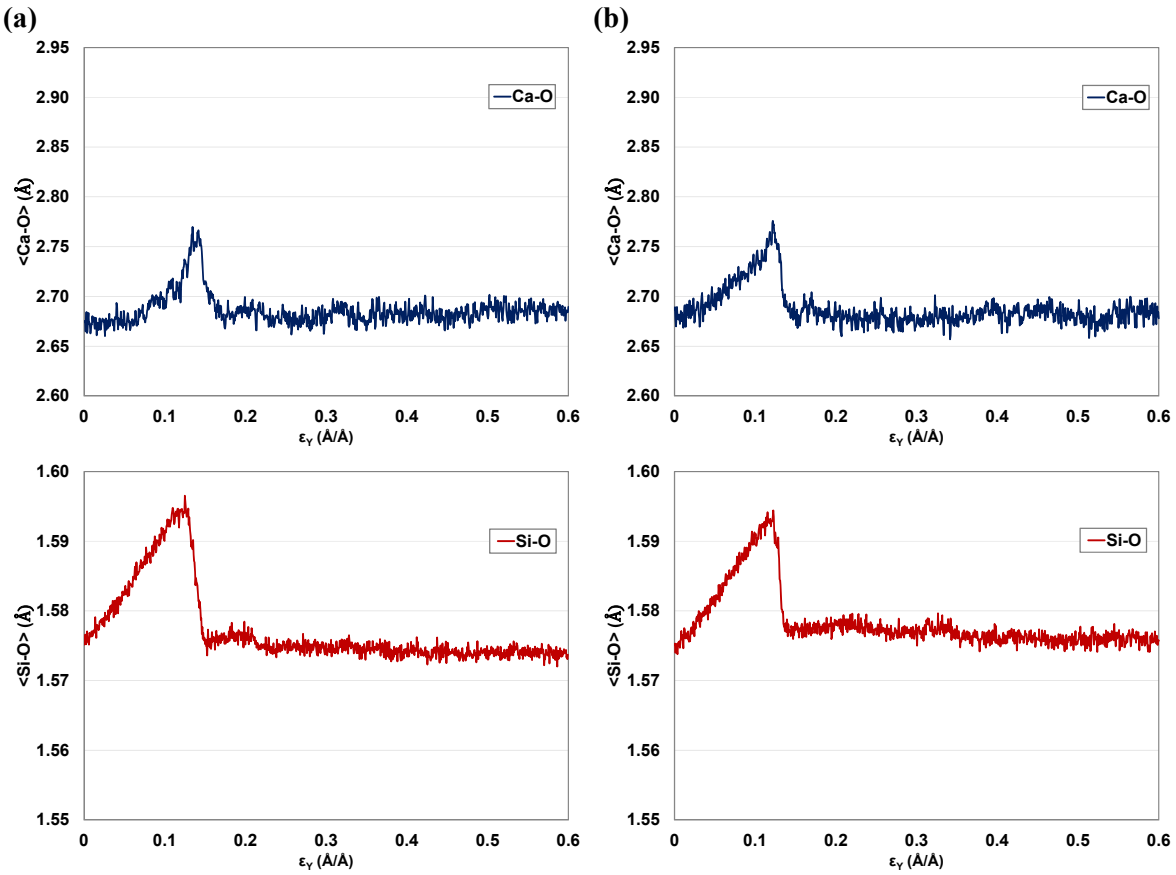

Figure 5-4 Average bond length as a function of strain along the *y* direction of (a) tobermorite 11 Å and (b) tobermorite 14 Å.

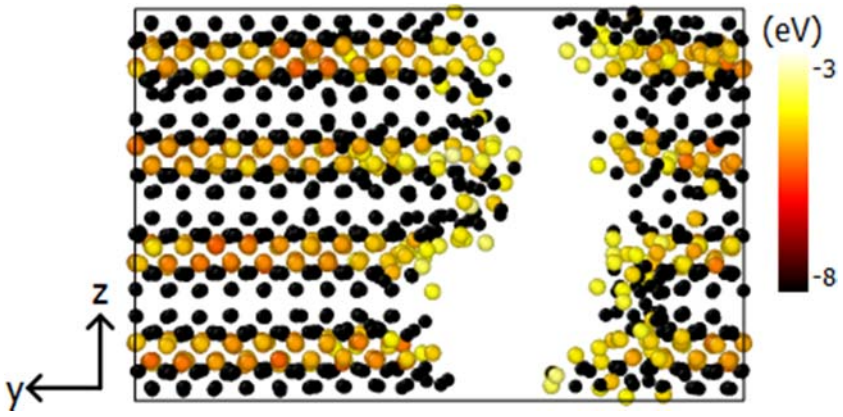

Figure 5-5 Energy of the covalent Ca-O and Si-O bonds in molecular structure of tobermorite 11 Å at the strain of 0.6 Å/Å applied in the *y* direction. (Black: Si; Color: Ca)

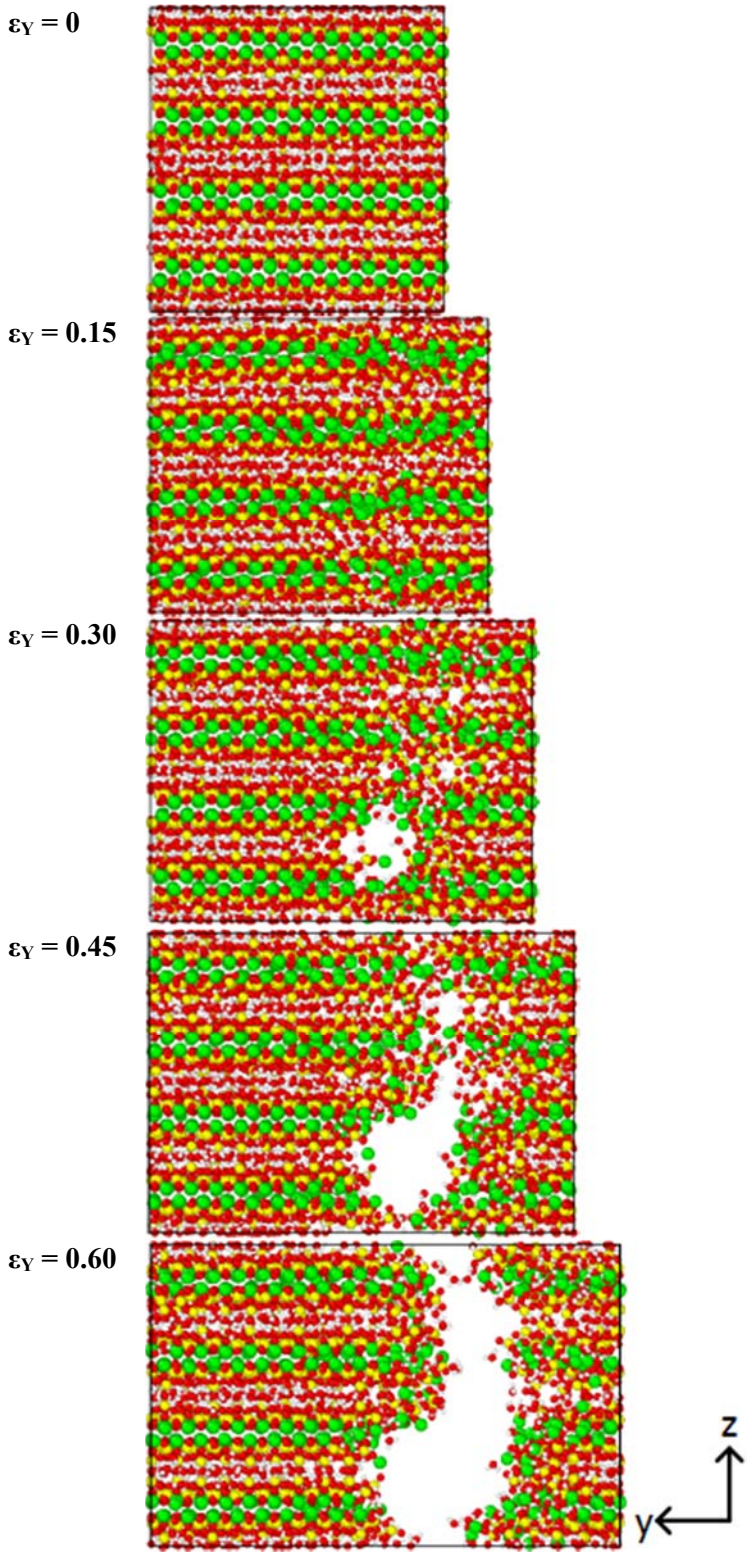

Figure 5-6 Progress of damage to the molecular structure of tobermorite 11 Å, under tensile strains in the *y* direction. (Green: Ca; Yellow: Si; Red: O; White: H)

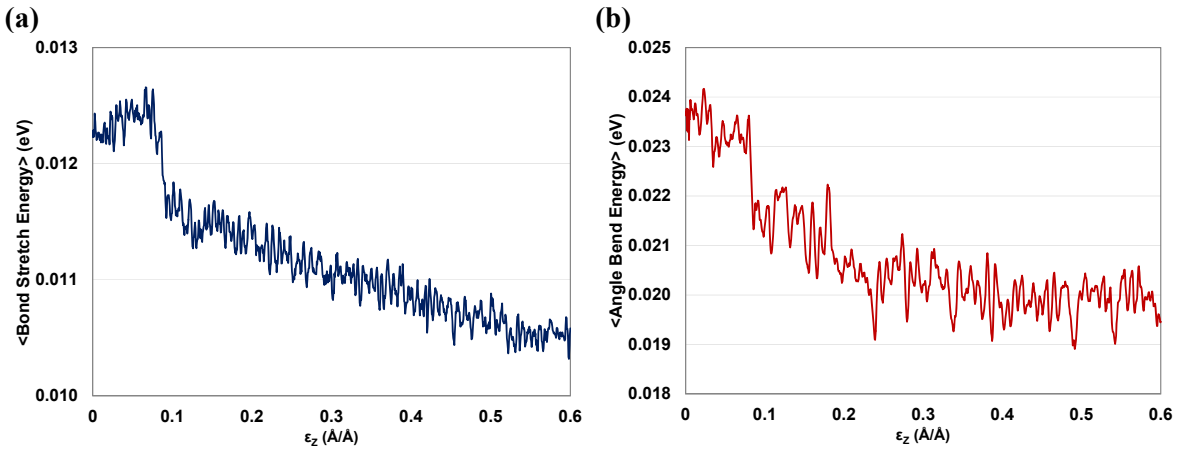

Figure 5-7 Average changes in (a) bond stretch and (b) angle bend energy of water molecules as a function of tensile strain applied in the *z* direction of tobermorite 11 Å.

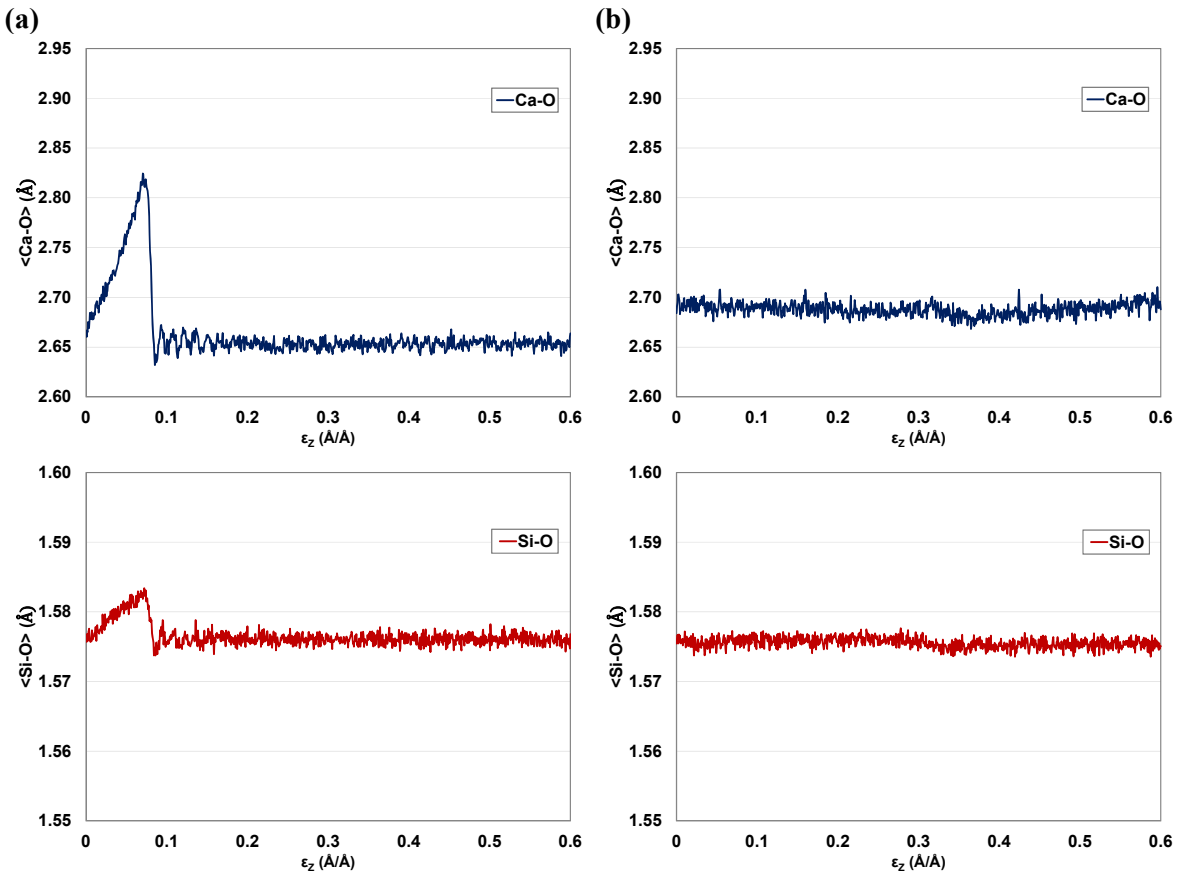

Figure 5-8 Average bond length as a function of strain along the *z* direction of (a) tobermorite 11 Å and (b) tobermorite 14 Å.

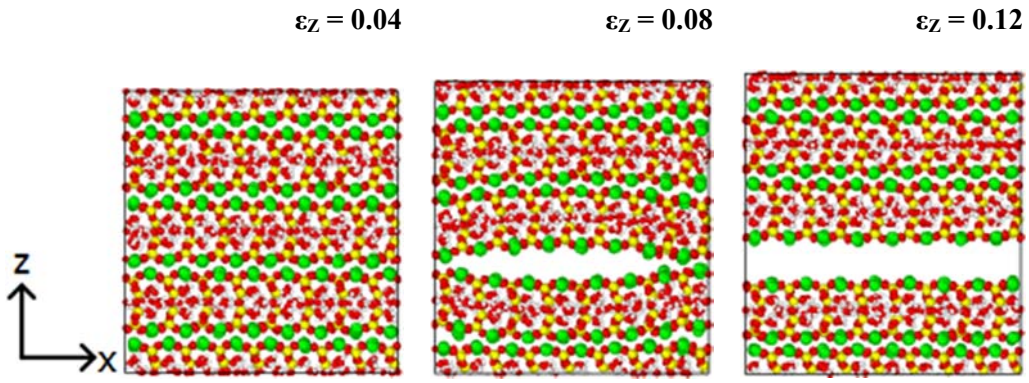

Figure 5-9 Damaged atomic structure of tobermorite 11 Å under tensile strain in the z direction. (Green: Ca; Yellow: Si; Red: O; White: H)

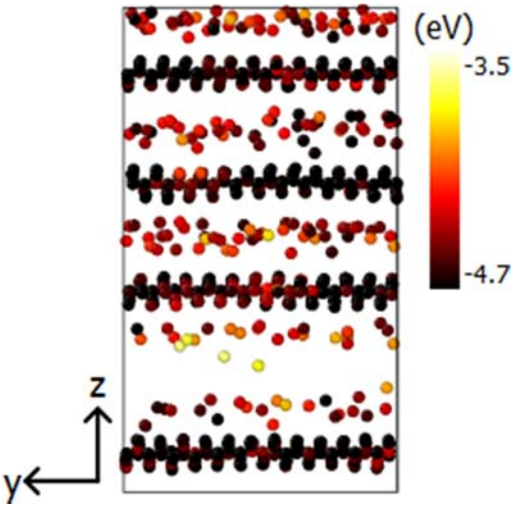

Figure 5-10 Potential energy of layer and interlayer calcium ions that exist in the molecular structure of tobermorite 14 Å at the strain of 0.33 Å/Å applied in the *z* direction.

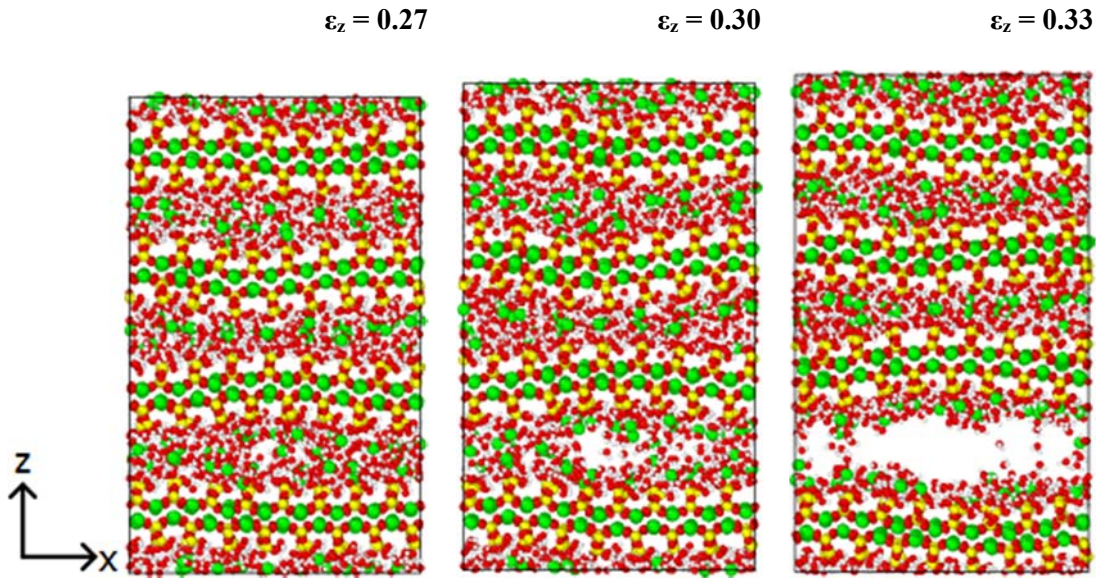

Figure 5-11 Damaged atomic structure of tobermorite 14 Å under tensile strain in the *z* direction. (Green: Ca; Yellow: Si; Red: O; White: H)

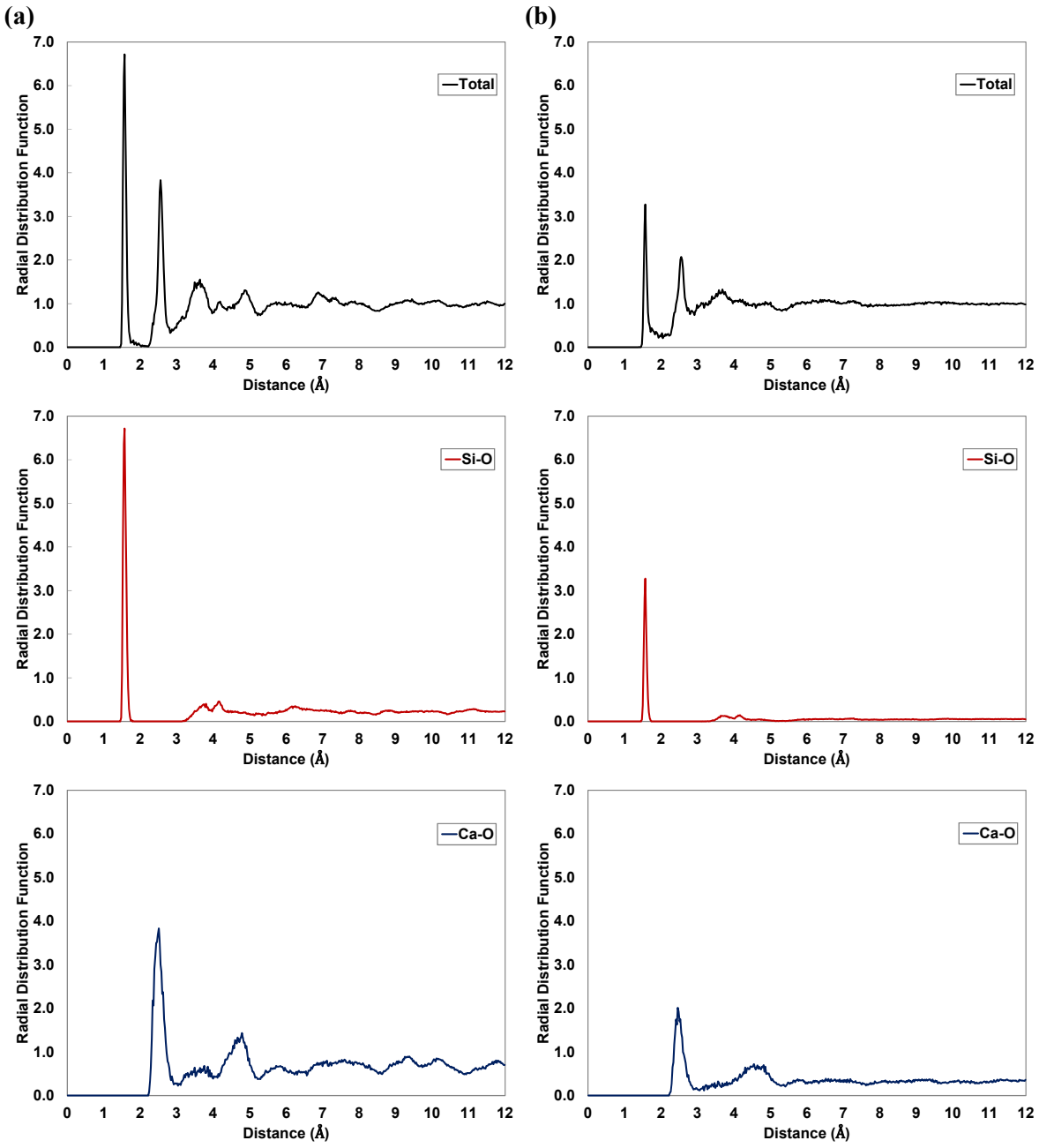

Figure 5-12 Total and partial radial distribution functions of (a) tobermorite 9 Å and (b) jennite.

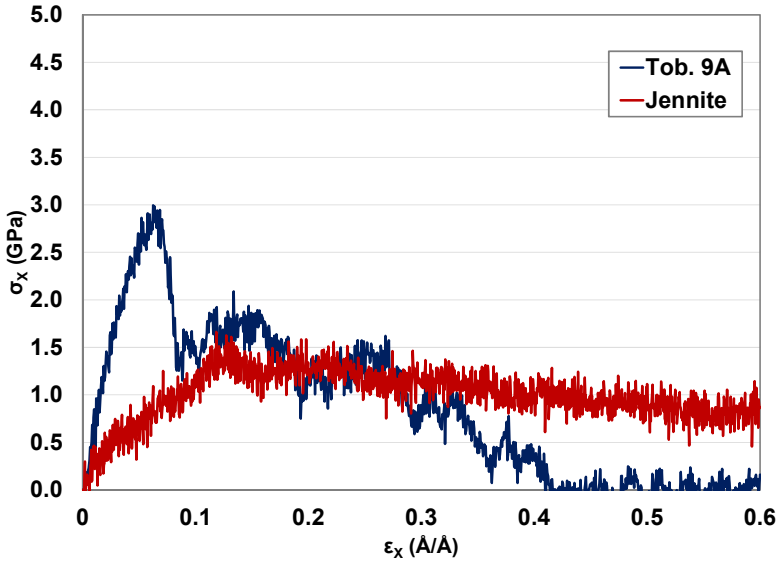

Figure 5-13 Stress-strain curve of tobermorite 9 Å and jennite crystals subjected to uniaxial tensile strain in the *x* direction.

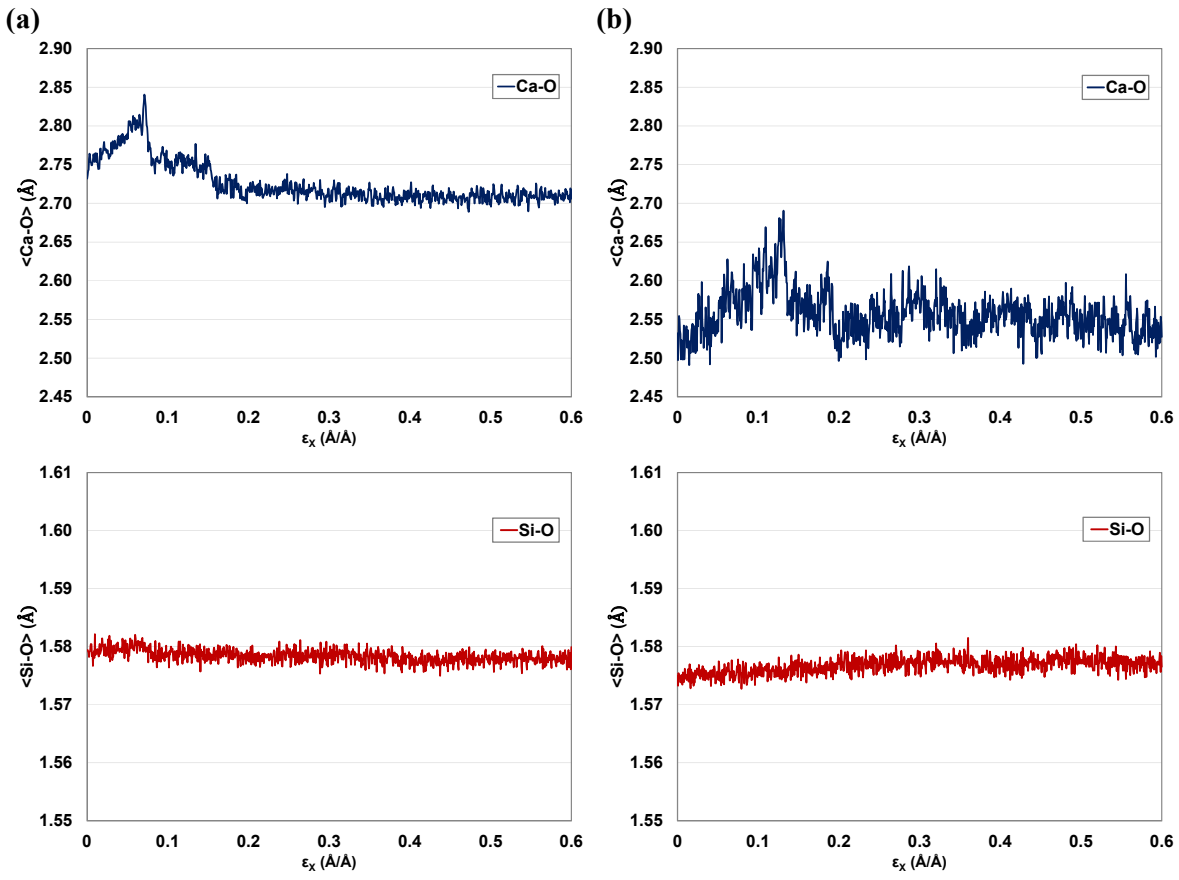

Figure 5-14 Average bond length as a function of strain along the *x* direction of (a) tobermorite 9 Å and (b) jennite.

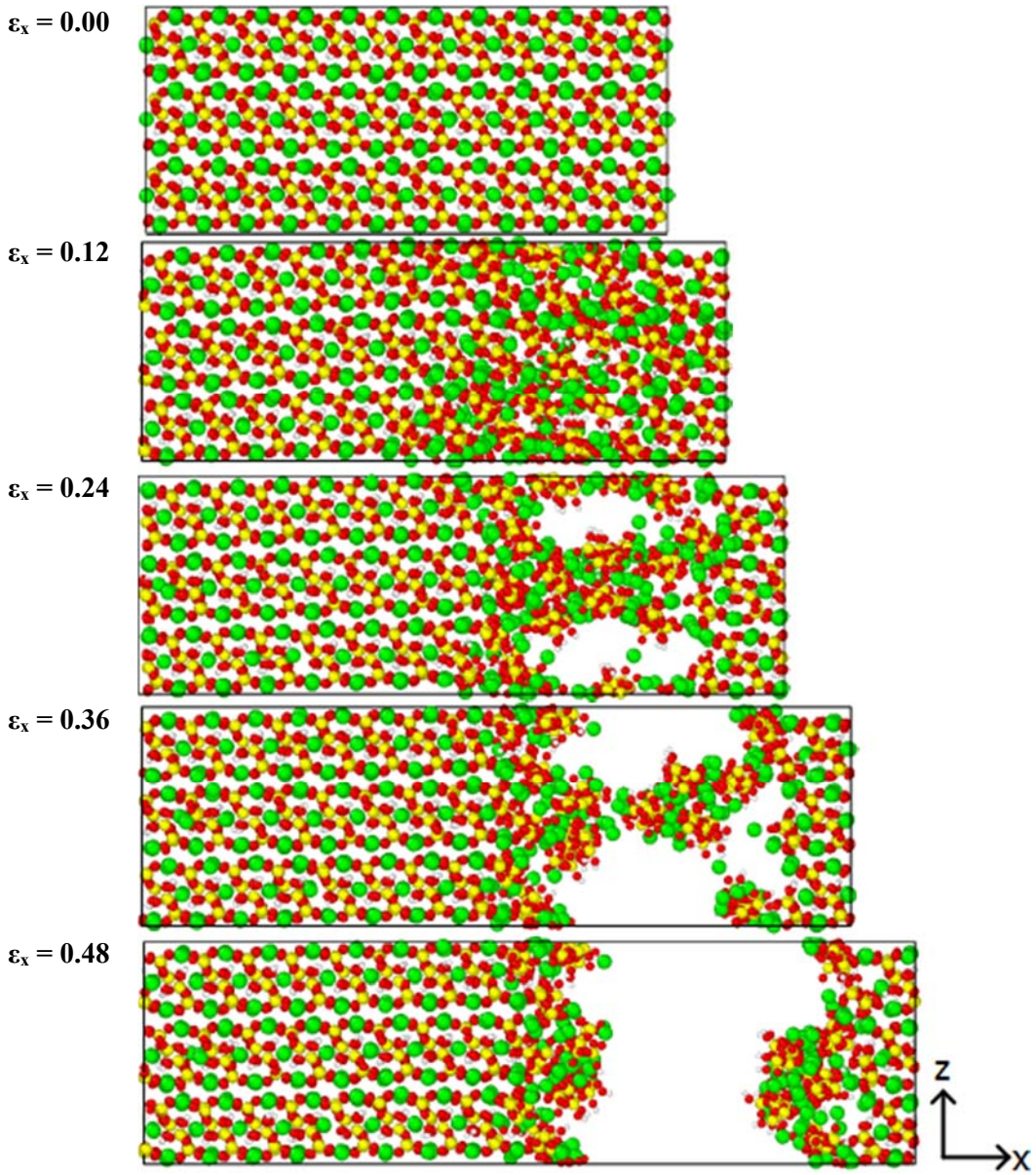

Figure 5-15 Process of damage to the molecular structure of tobermorite 9 Å under tensile strains in the *x* direction. (Green: Ca; Yellow: Si; Red: O; White: H)

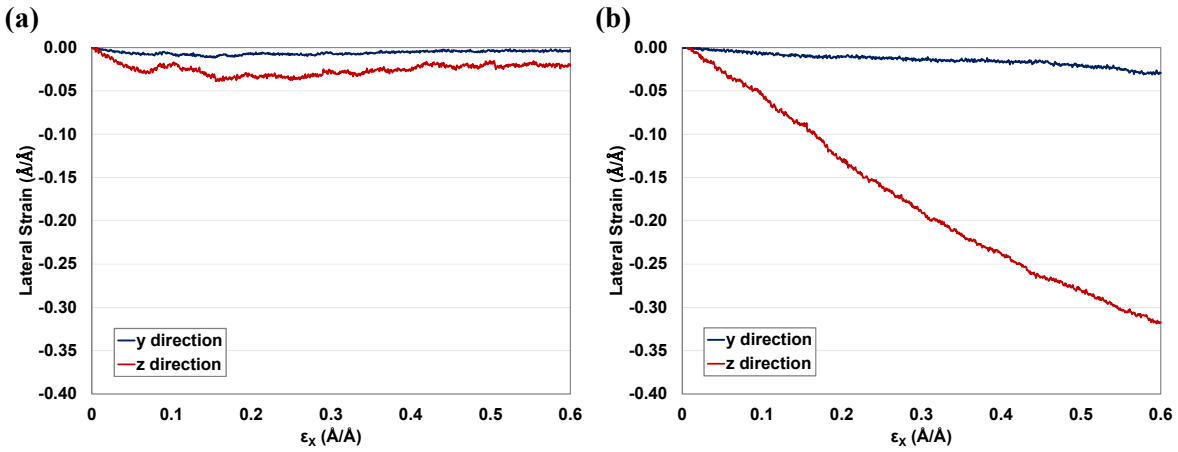

Figure 5-16 Lateral strains as a function of uniaxial strain in the *x* direction for (a) tobermorite 9 Å, and (b) jennite crystals.

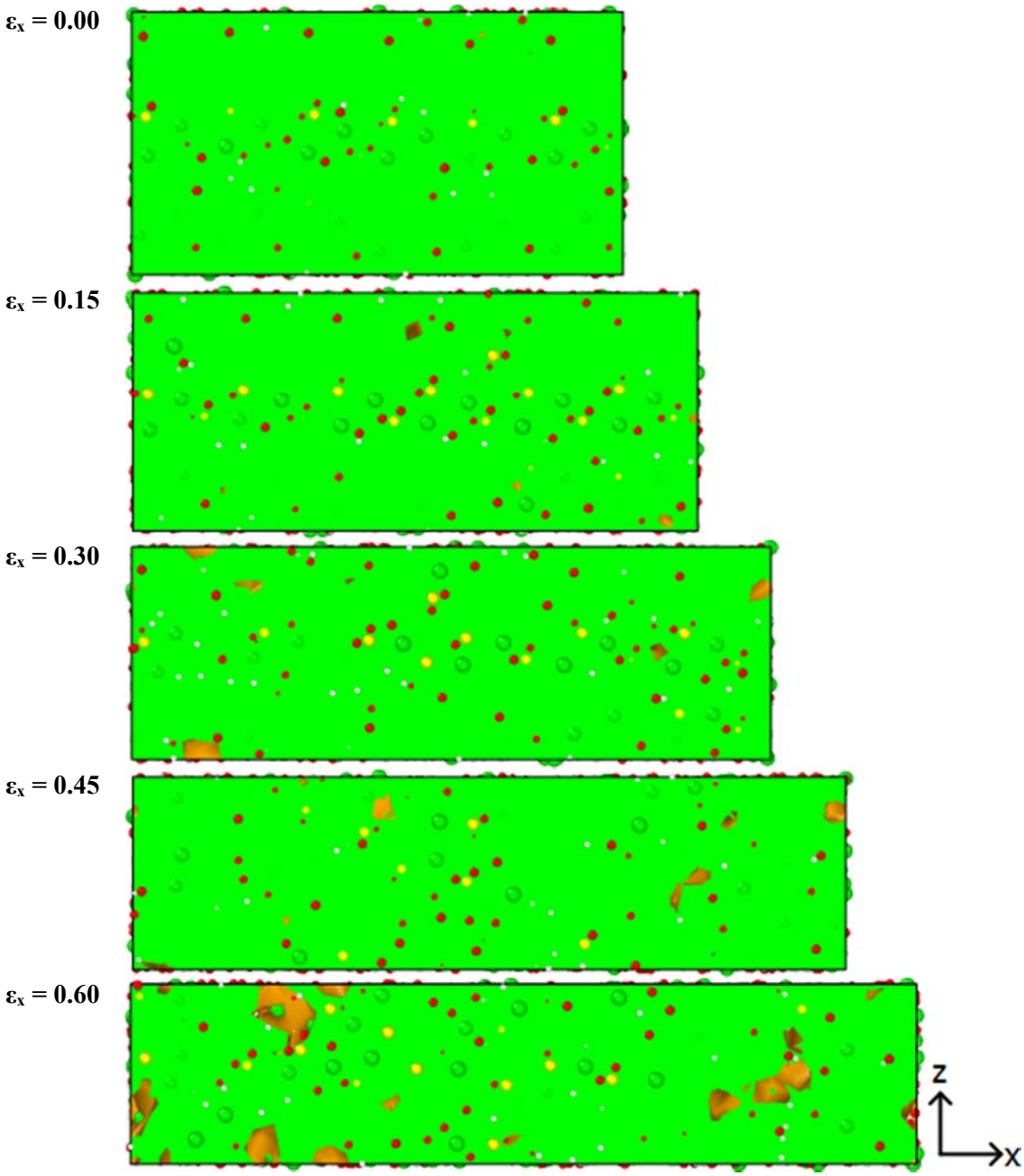

Figure 5-17 The formation and distribution of local voids in the structure of jennite subjected to the uniaxial tensile strain in the *x* direction.
(Orange and green represents the inner and outer surface of solid particles, respectively.)

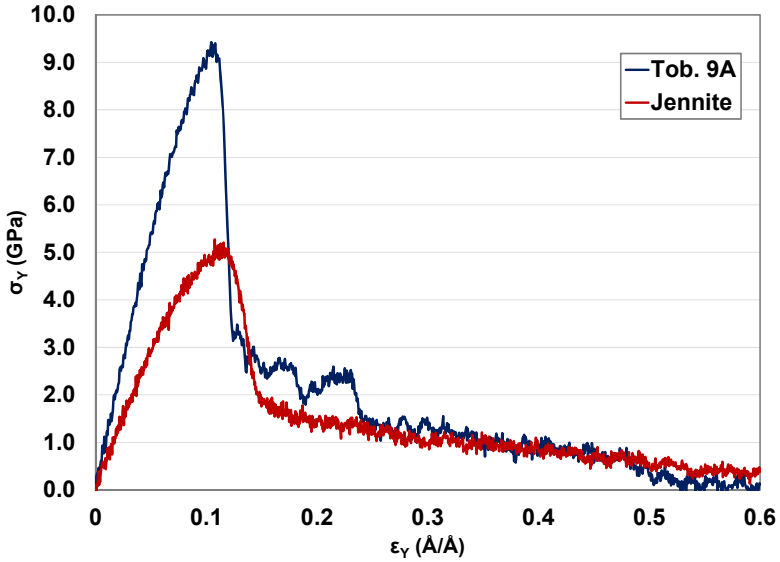

Figure 5-18 Stress-strain curve of tobermorite 9 Å and jennite crystals subjected to uniaxial tensile strain in the *y* direction.

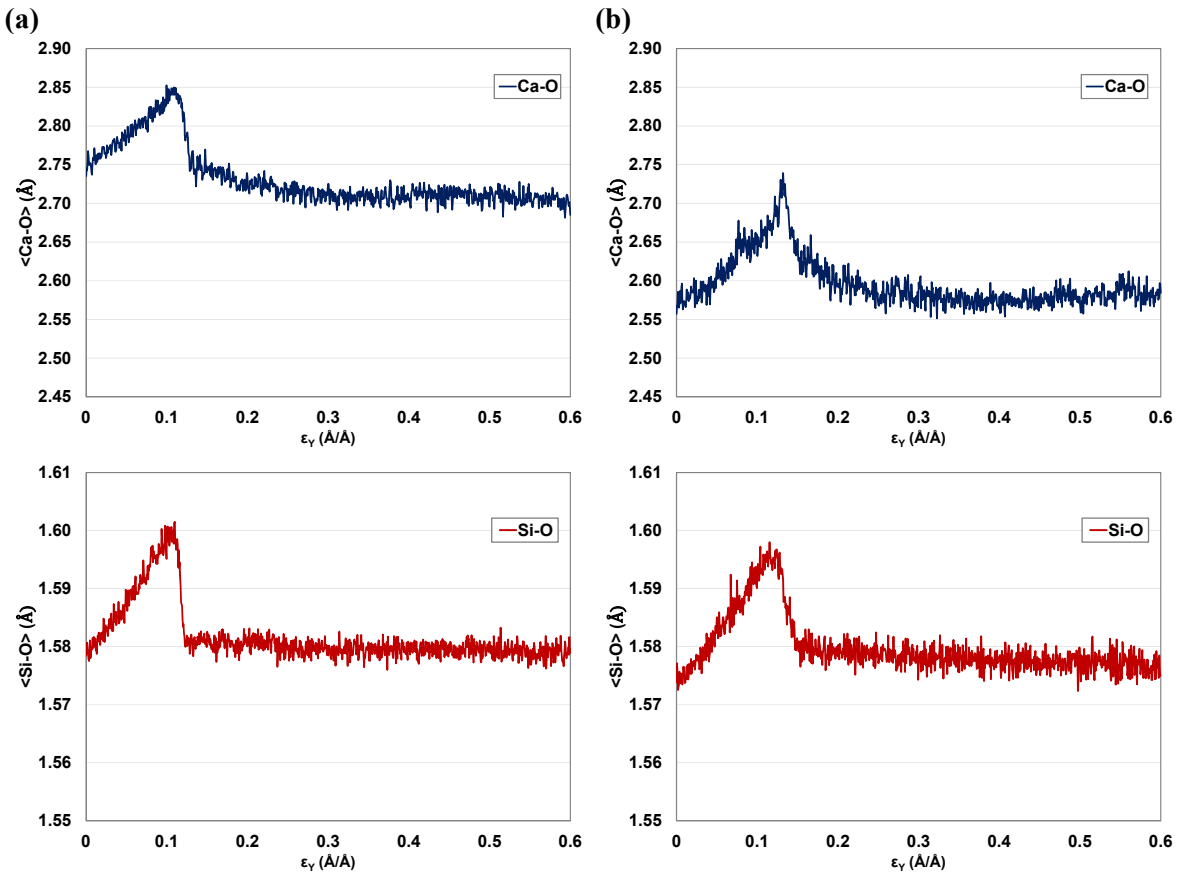

Figure 5-19 Average bond length as a function of strain along the y direction of (a) tobermorite 9 Å and (b) jennite.

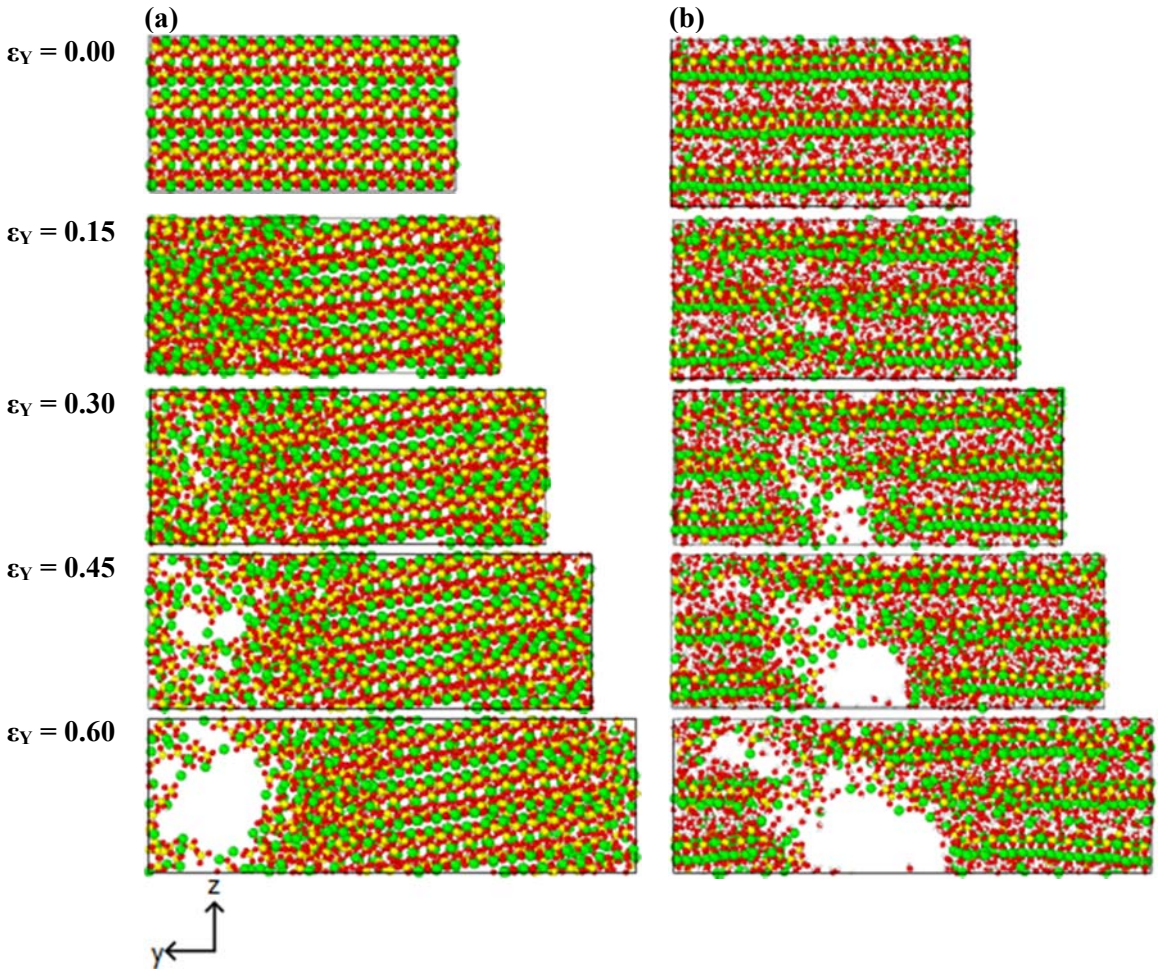

Figure 5-20 Process of damage to the molecular structure of (a) tobermorite 9 Å and (b) jennite under tensile strains in the *y* direction. (Green: Ca; Yellow: Si; Red: O; White: H)

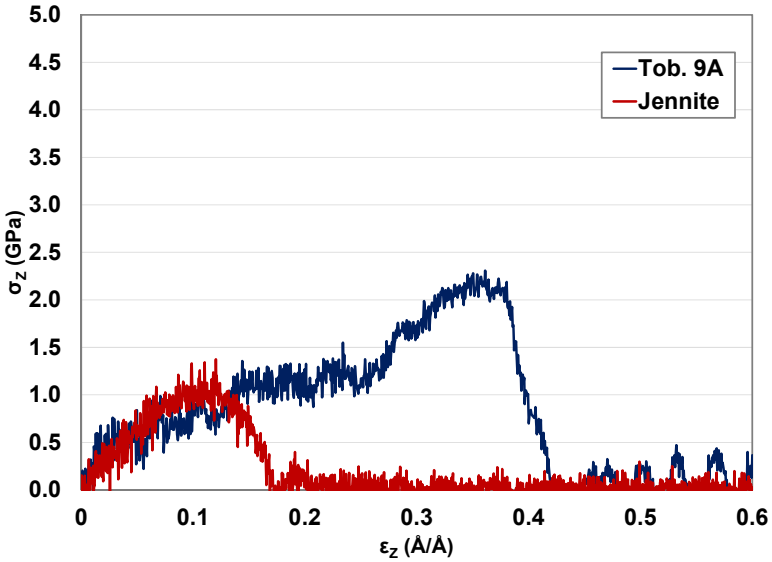

Figure 5-21 Stress-strain curve of tobermorite 9 Å and jennite crystals subjected to uniaxial tensile strain in the *z* direction.

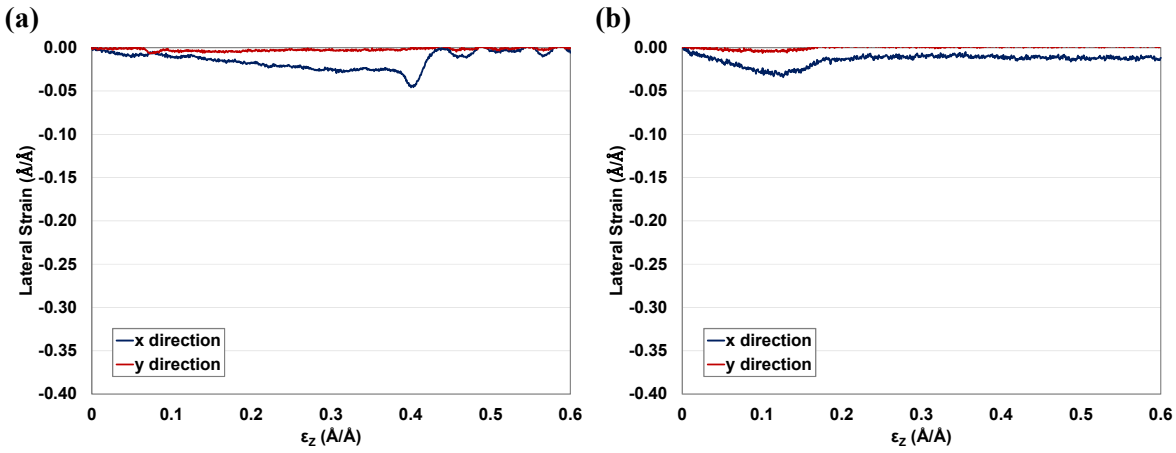

Figure 5-22 Lateral strains as a function of uniaxial strain in the *z* direction for (a) tobermorite 9Å, and (b) jennite crystals.

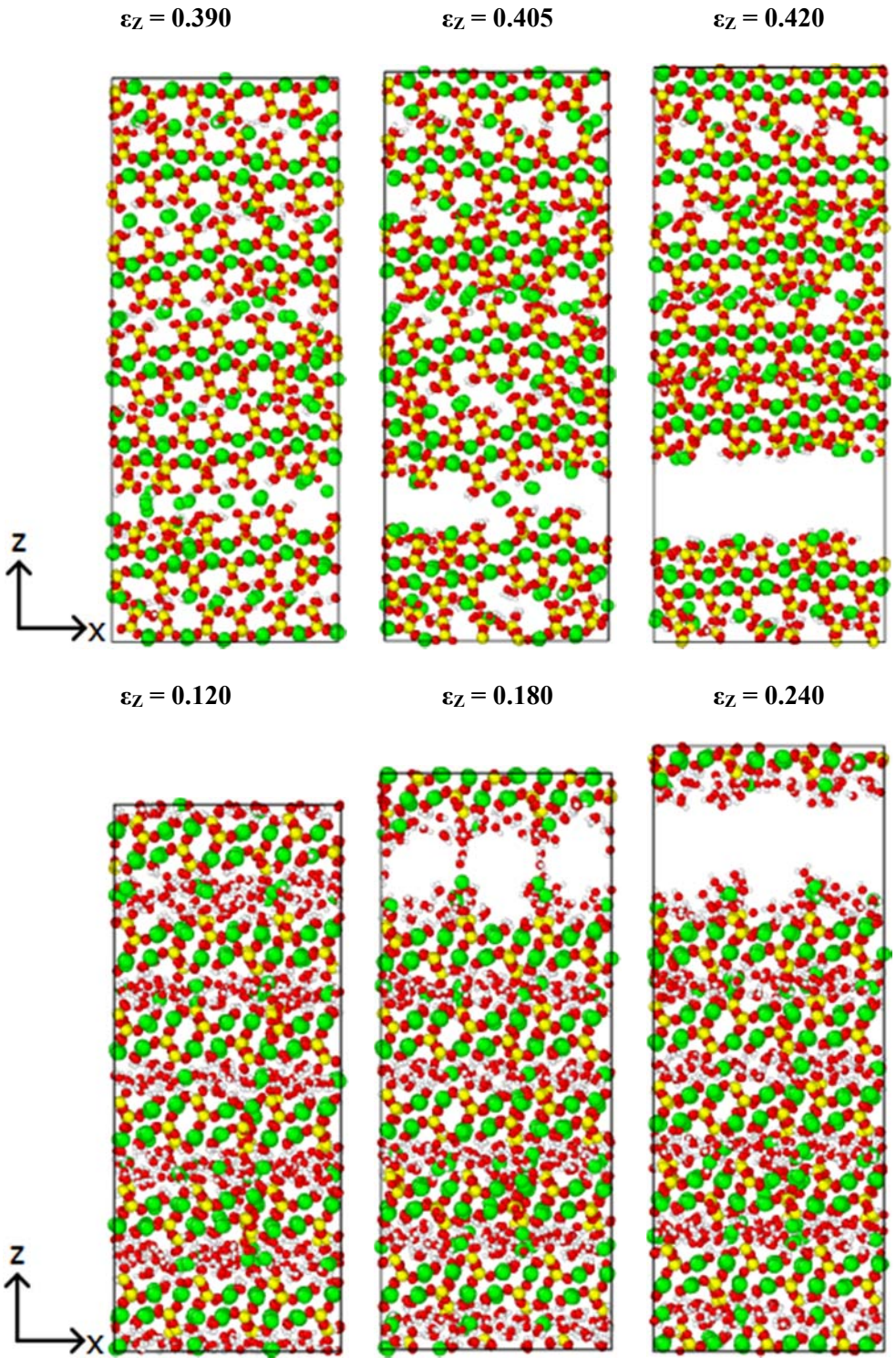

Figure 5-23 Process of damage to the molecular structure of tobermorite 9 Å (top) and jennite (bottom) under tensile strains in the *z* direction. (Green: Ca; Yellow: Si; Red: O; White: H)

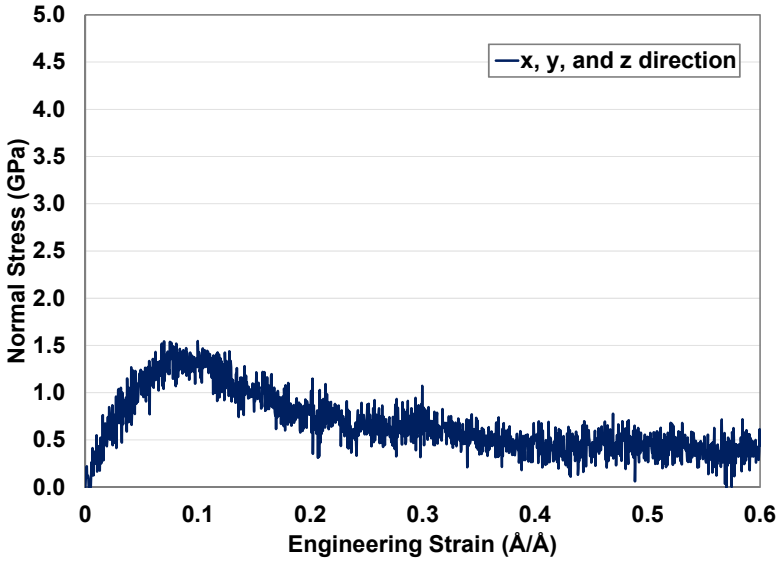

Figure 5-24 Stress-strain curve of hydrogarnet crystals subjected to uniaxial tensile strain.

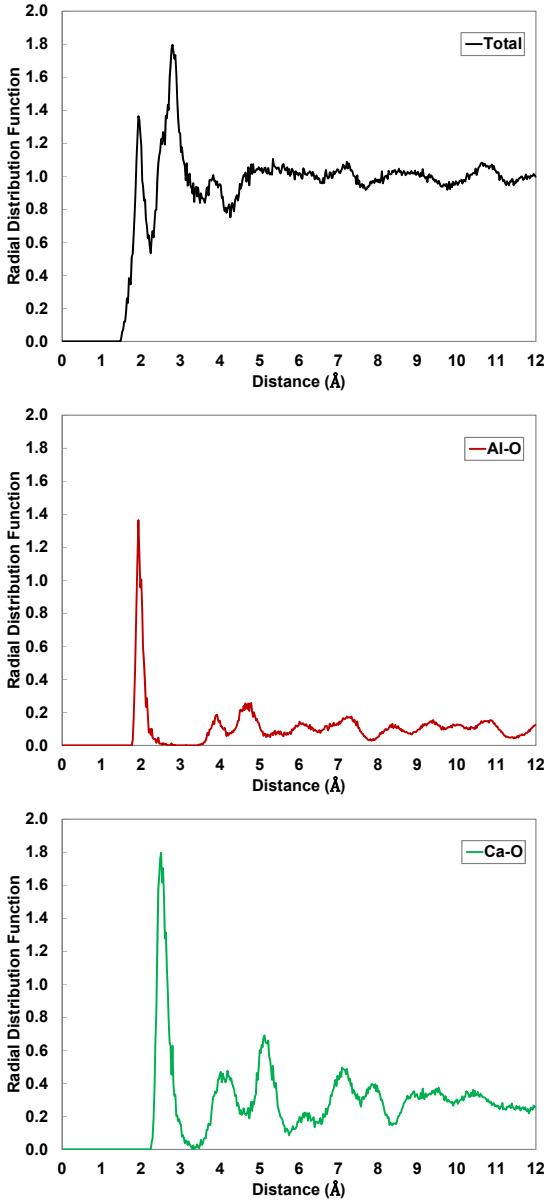

Figure 5-25 Total and partial radial distribution functions of hydrogarnet.

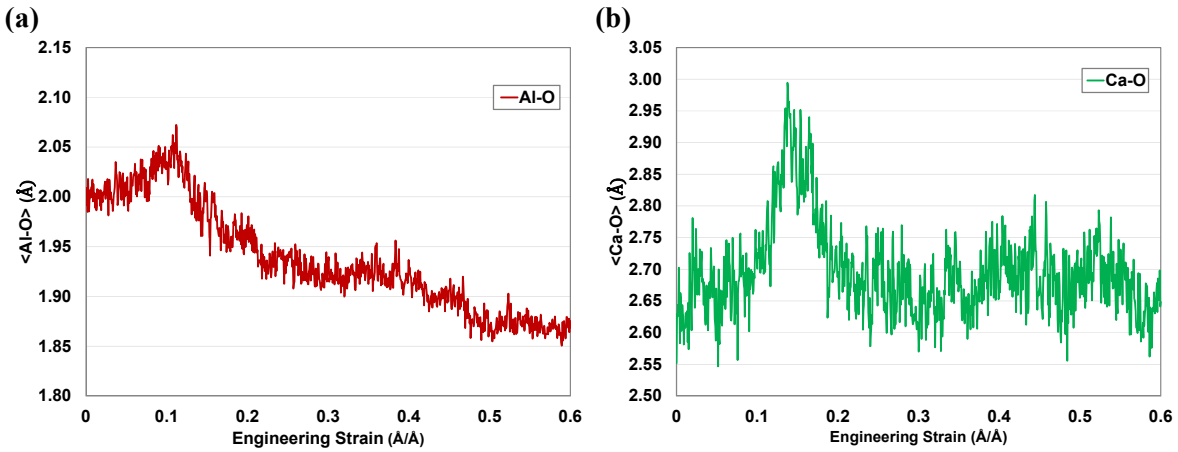

Figure 5-26 Average (a) Al-O, and (b) Ca-O bond length as a function of strain along the *x* direction of hydrogarnet.

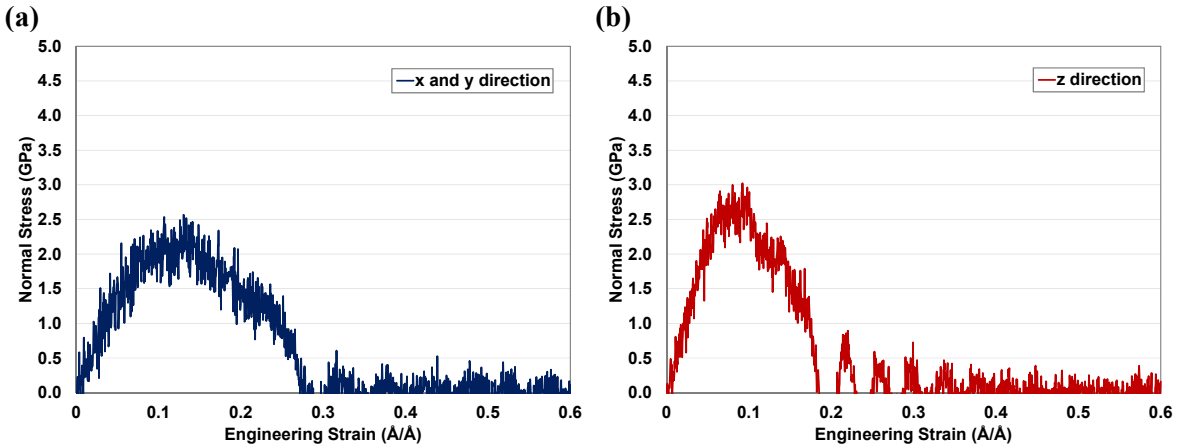

Figure 5-27 Stress-strain curve of the ettringite crystal subjected to uniaxial tensile strains in the (a) *x*/*y* and (b) *z* direction.

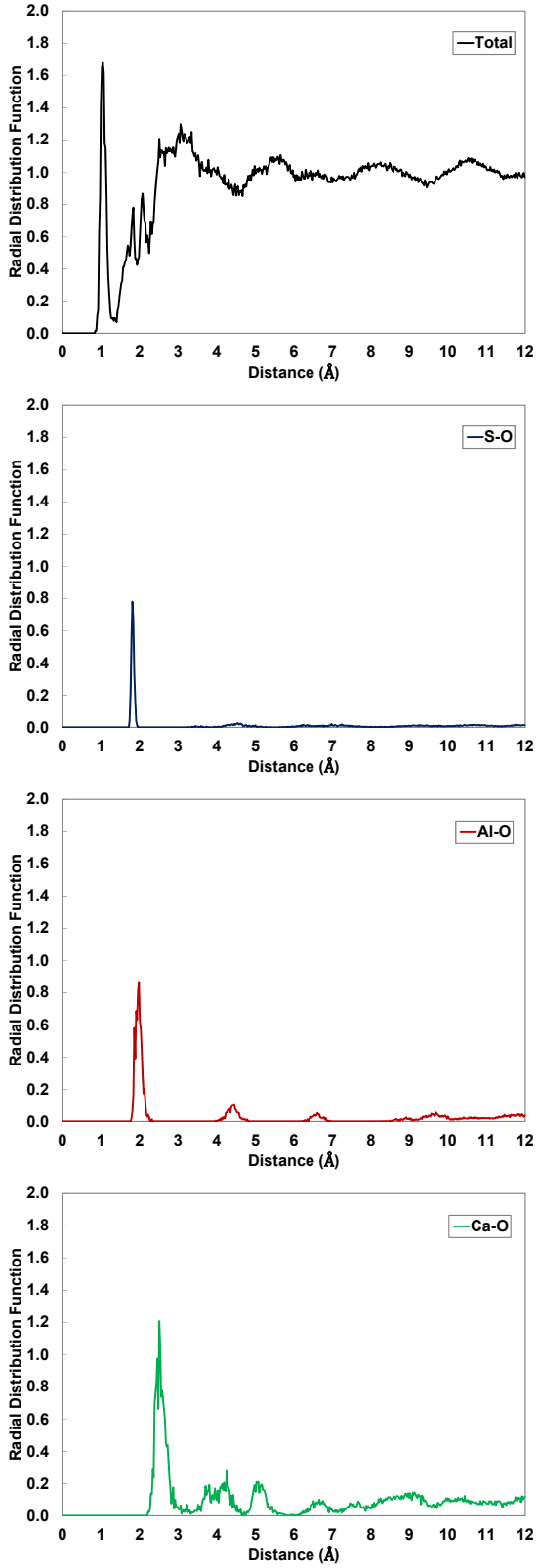

Figure 5-28 Total and partial radial distribution functions of ettringite.

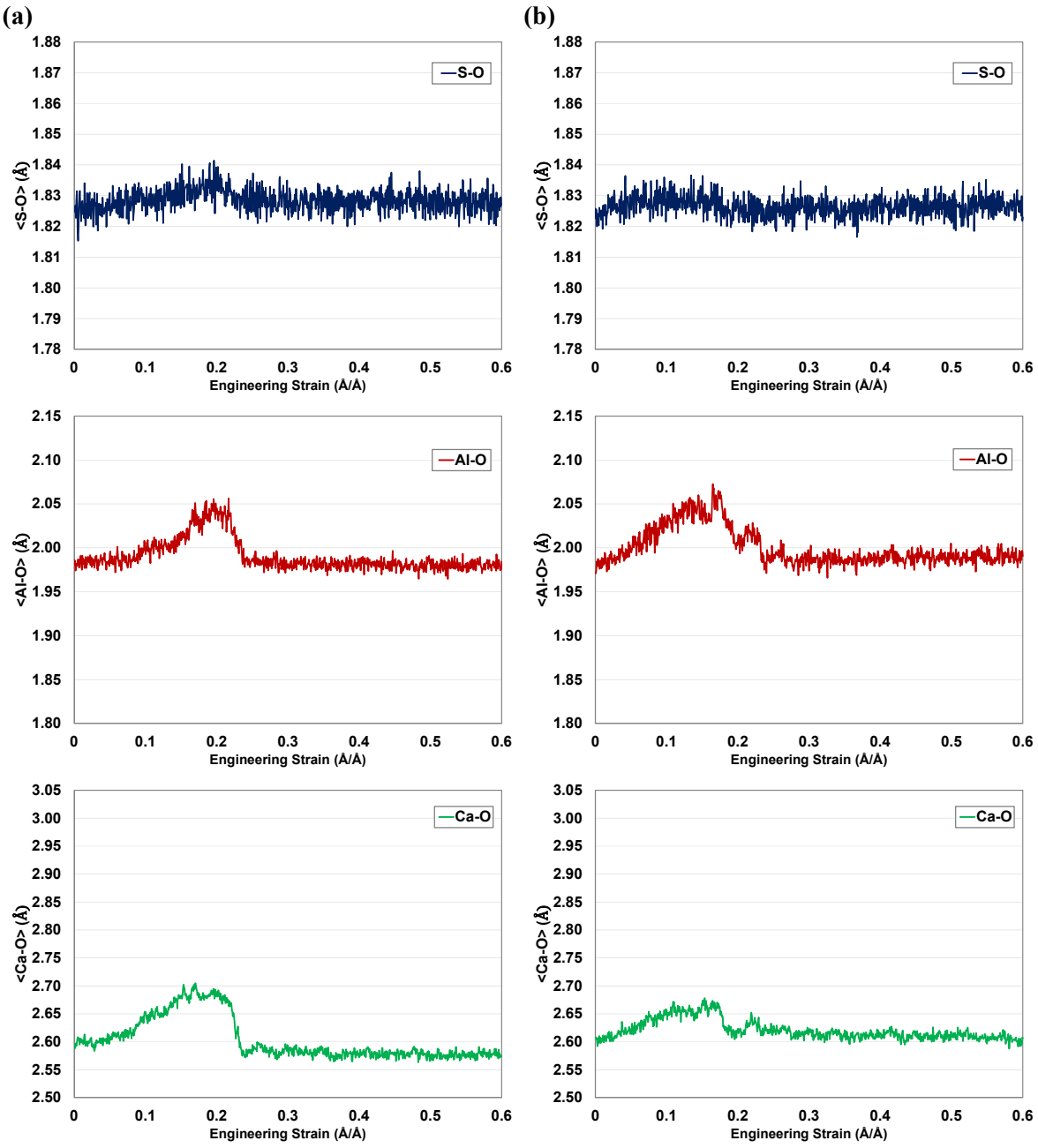

Figure 5-29 Average S-O, Al-O, and Ca-O bond length as a function of strain along the (a) *x*/*y* and (b) *z* direction of ettringite.

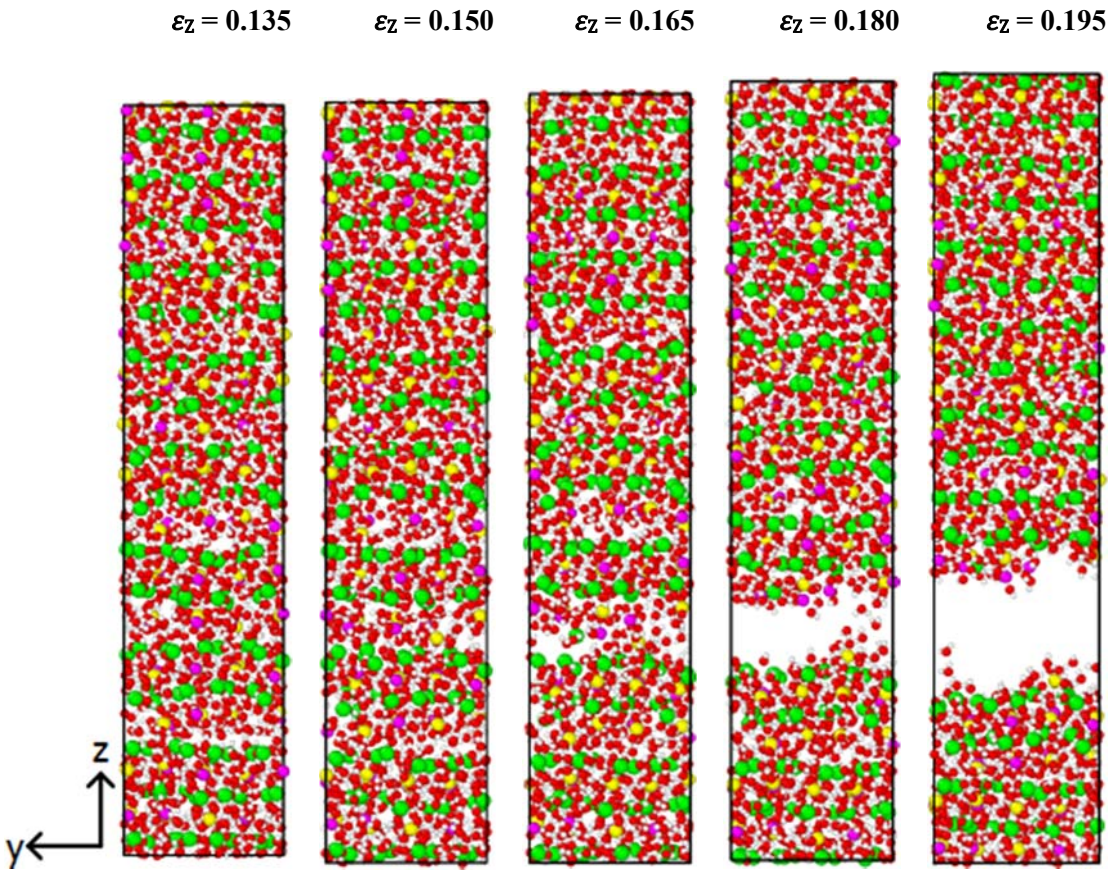

Figure 5-30 Damage to the molecular structure of ettringite under tensile strains in the *z* direction. (Green: Ca; Yellow: S; Pink: Al; Red: O; White: H)

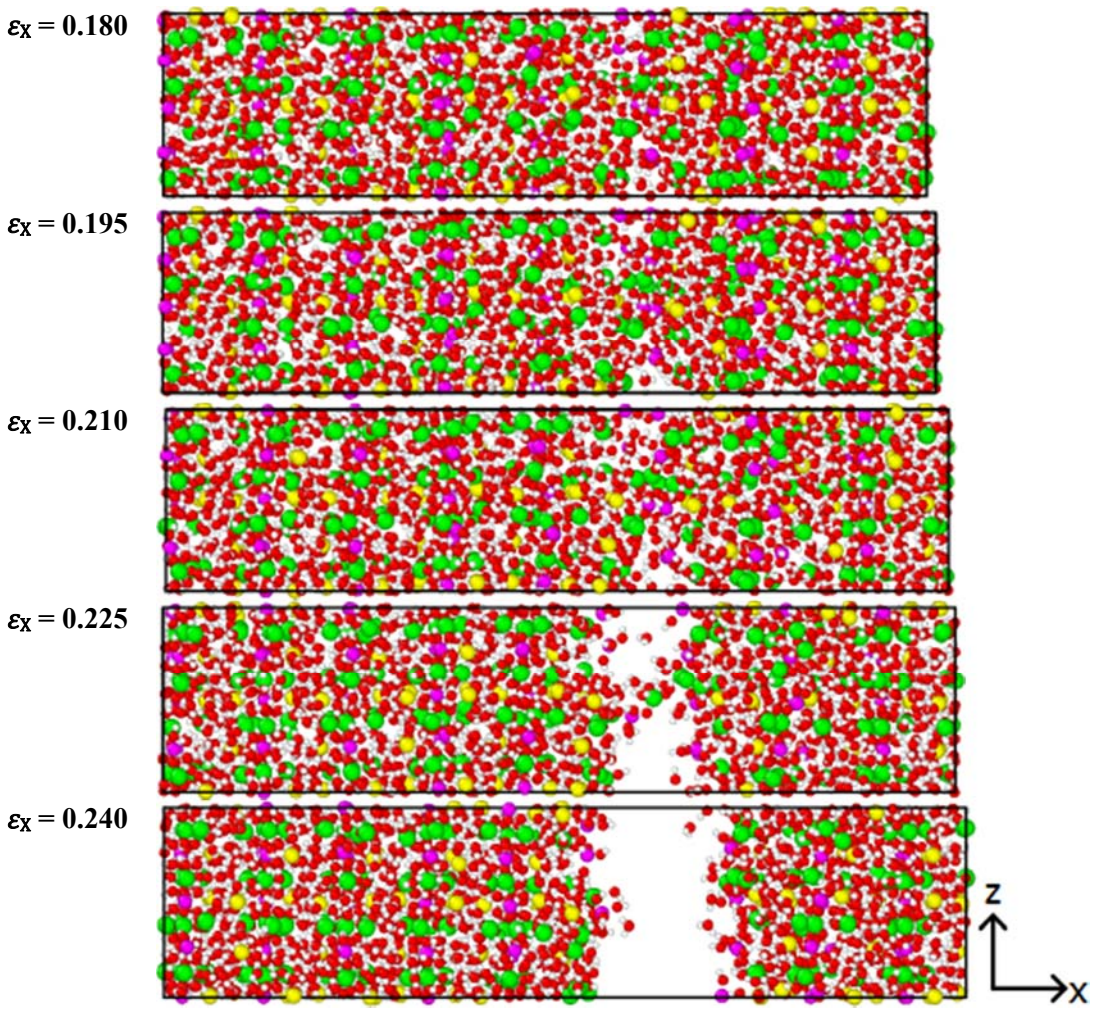

Figure 5-31 Damage to the molecular structure of ettringite under tensile strains in the *x* direction. (Green: Ca; Yellow: S; Pink: Al; Red: O; White: H)

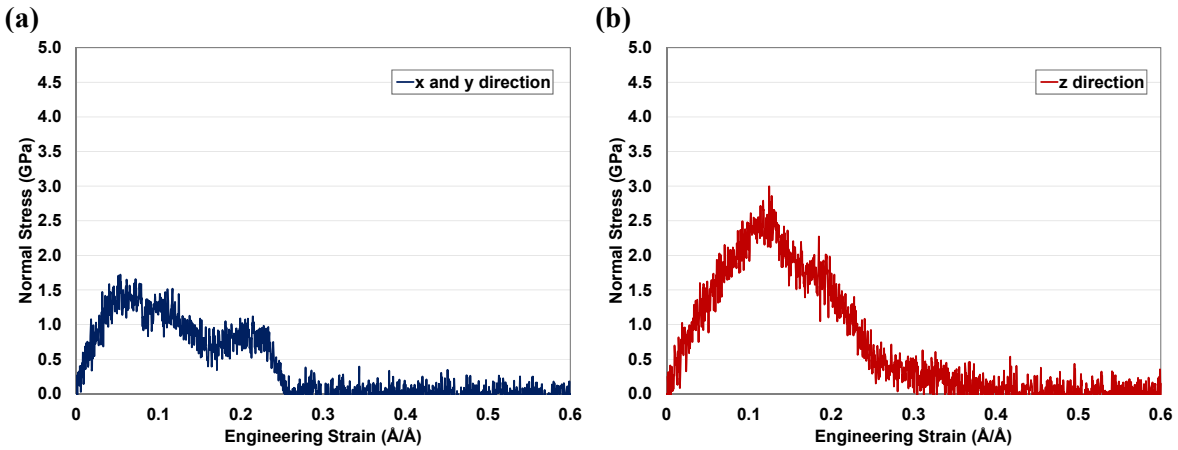

Figure 5-32 Stress-strain curve of the kuzelite crystal subjected to uniaxial tensile strains in the (a) *x*/*y* and (b) *z* direction.

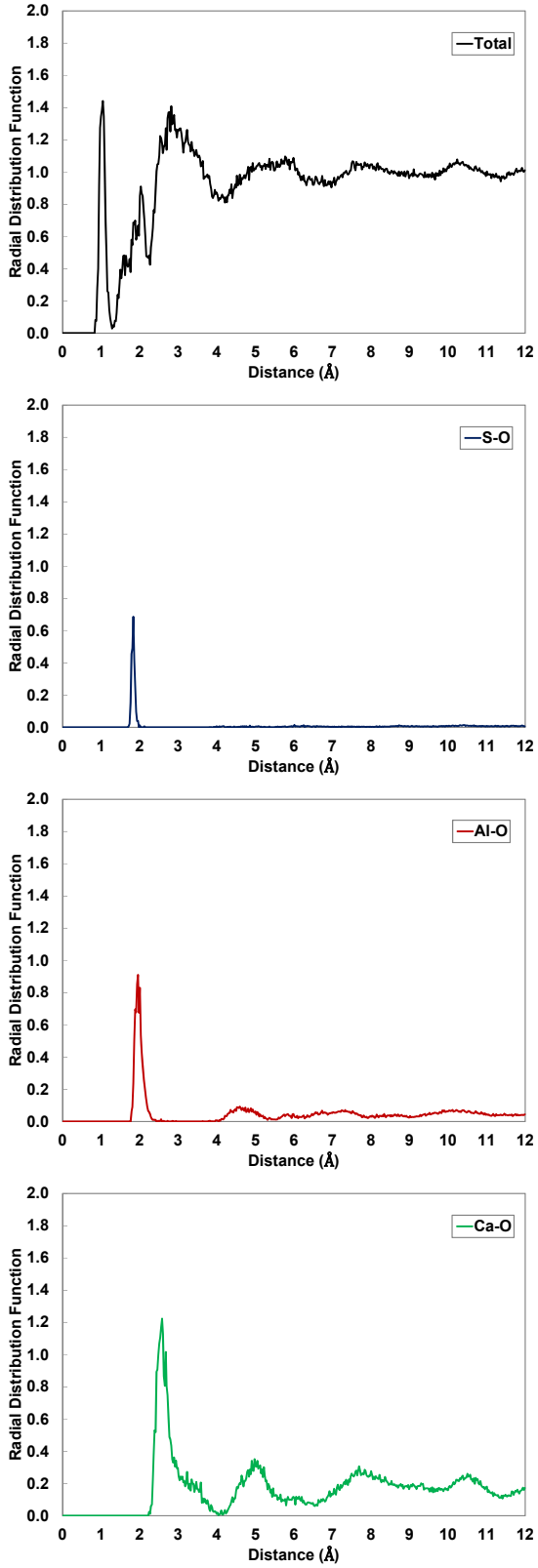

Figure 5-33 Total and partial radial distribution functions of kuzelite.

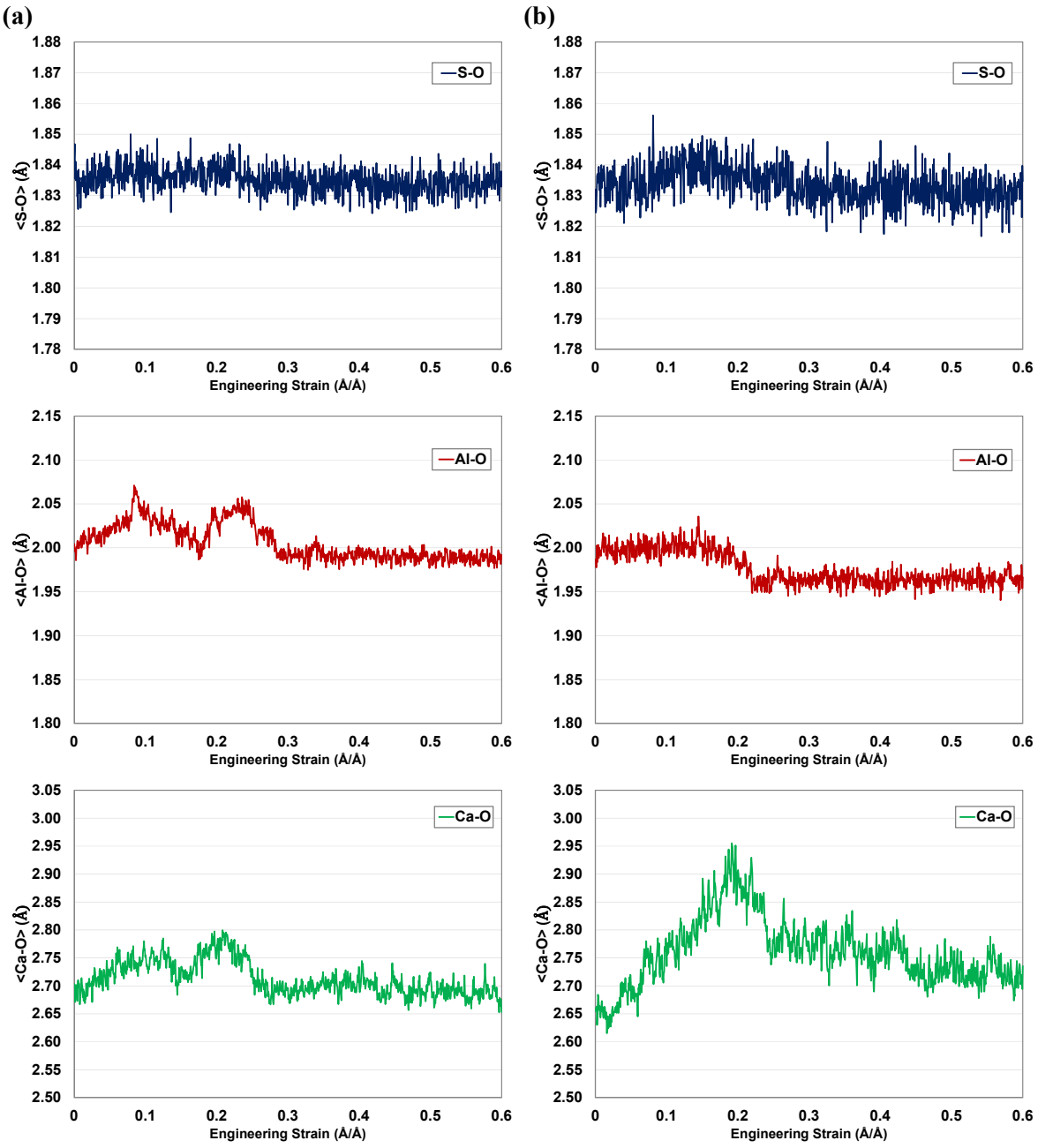

Figure 5-34 Average S-O, Al-O, and Ca-O bond length as a function of strain along the (a) *x*/*y* and (b) *z* direction of kuzelite.

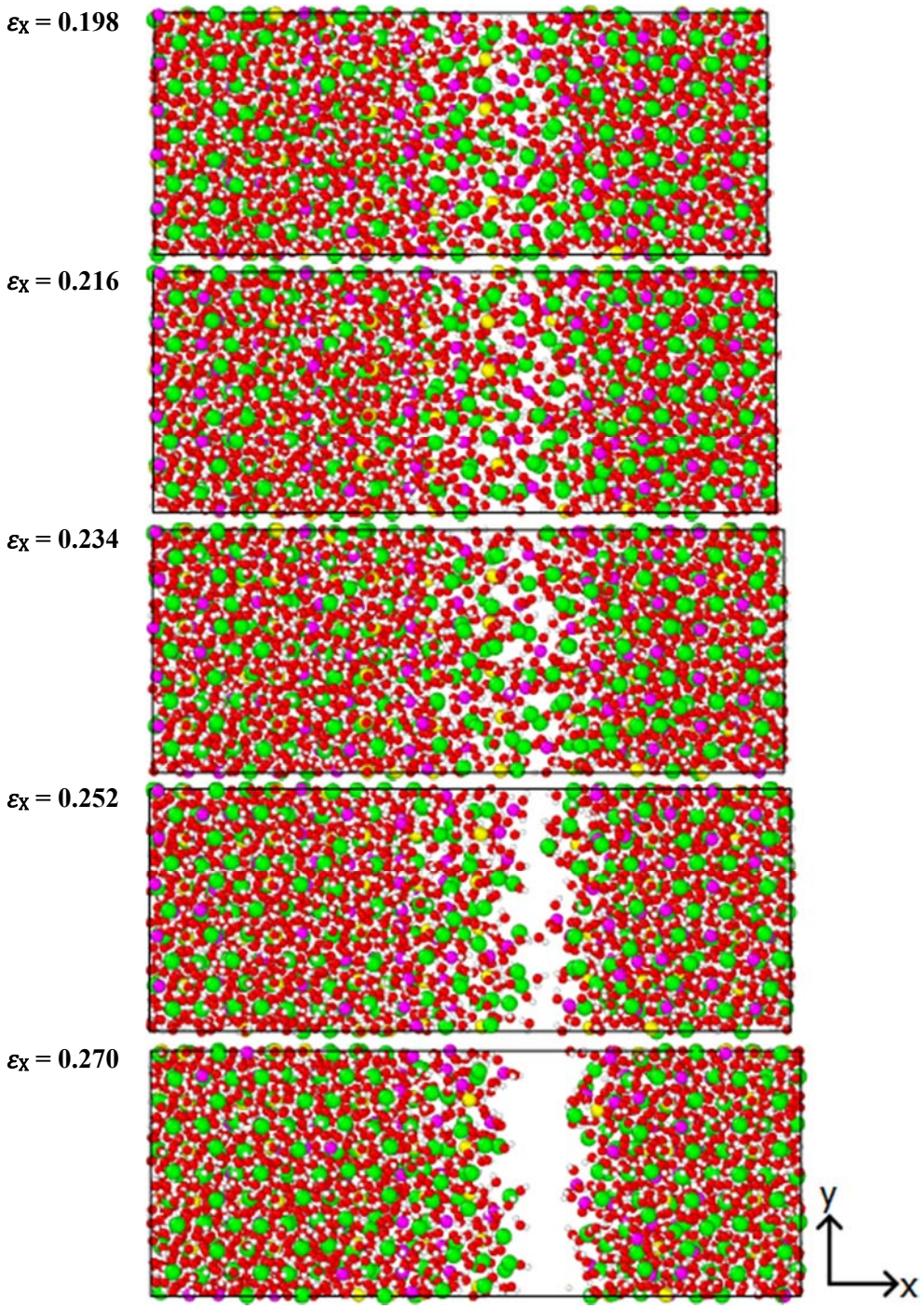

Figure 5-35 Damage to the molecular structure of kuzelite under tensile strains in the *x* direction. (Green: Ca; Yellow: S; Pink: Al; Red: O; White: H)

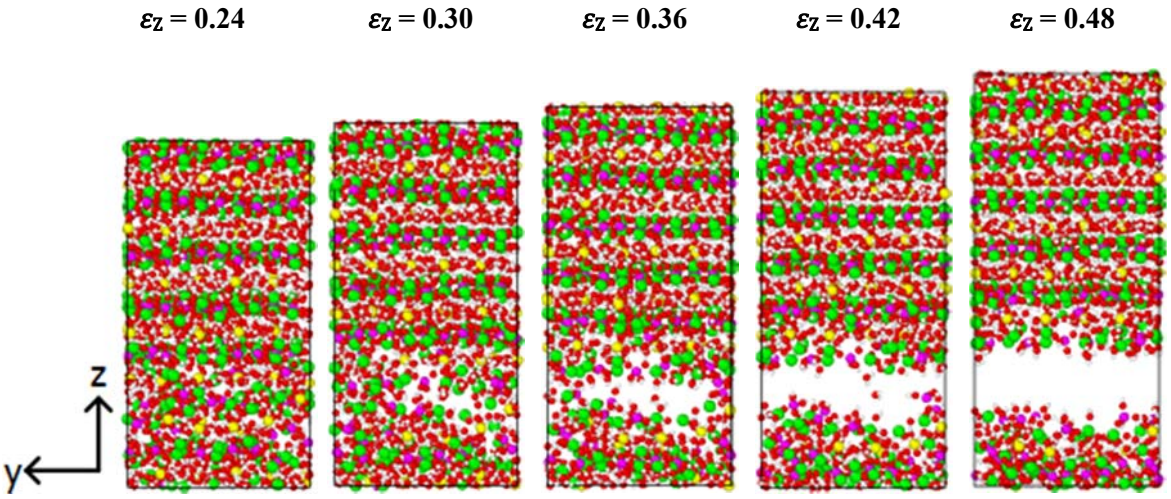

Figure 5-36 Damage to the molecular structure of kuzelite under tensile strains in the *z* direction. (Green: Ca; Yellow: S; Pink: Al; Red: O; White: H)

CONCLUSIONS

There is a growing interest in the identification of the nano-scale properties of cement-based materials, such as concrete and mortar. Since cement-based materials are considered as one of the most widely used construction materials throughout the world, development of time and cost-efficient strategies to examine their nano structures is an important step forward to better understand the associated macroscopic engineering properties. In the case of concrete for example, the outcome of such efforts can be directly utilized to improve the durability and performance of reinforced concrete structures during their service life. Because of the fact that binders plays an important role in the stiffness and strength properties of cement-based materials, investigation of the mechanical characteristics of the nano-structure of binders provides invaluable information on the over-all mechanical behavior of this group of materials.

Portland cement, which is commonly used in reinforced concrete (RC) structures, reacts with water through the hydration process and binds the aggregates by forming a complex material called hydrated cement paste (HCP). Despite several research efforts, some fundamental questions about the stoichiometry and morphology of this essential building block of concrete have remained unanswered. The HCP is a heterogeneous composite material, which can be characterized by its constituent phases, each of which contributes to the strength and stiffness of the net paste.

This thesis provides a comprehensive study on the mechanical characteristics of the HCP constituents at the nano-scale using MD simulations. This was achieved by examining various cement paste hydration products, such as calcium silicate hydrates, calcium hydroxide, calcium aluminate monosulphate hydrates, calcium aluminate trisulphate hydrates, and hydrogarnet. Based on a detailed investigation of the hydration products, a complete set of crystalline

structures was developed, including portlandite, tobermorite 9, 11, and 14 Å, jennite, ettringite, kuzelite, and hydrogarnet.

Contrary to the previous simulations that were based on either MM or ab initio methods, this study utilized the MD method to calculate the elastic properties (e.g., bulk and shear modulus) of the crystals under consideration. Furthermore, appropriate formulas were provided to estimate the corresponding Young's modulus and Poisson's ratio following the VRH equations. The outcome of simulations conducted in this study indicated that the MD method is fully capable of predicting the elastic properties of the HCP constituents. It was also shown that in several cases, the MD method can provide predications that are closer to the experimental tests compared to the ones obtained from the MM and ab initio methods. In addition to the HCP constituents, a separate effort was made to estimate the elastic properties of the C-S-H gel. For this purpose, the MD simulation results obtained for the individual C-S-H components (i.e., tobermorite family and jennite) were rescaled to those of the C-S-H gel by taking advantage of microporomechanics. The elastic properties of each of the tobermorite and jennite crystals were found significantly different from the ones available in the literature for the C-S-H gel. This highlighted the necessity of investigating the effect of pores that naturally exist in the nano-structure of the C-S-H gel. To address this issue, two homogenization models (i.e., SC and MT) were employed to take into account the contribution of pores to the elastic properties of the C-S-H constituents calculated by MD simulations. It was seen that the estimates of the elastic properties updated by the SC and MT models are satisfactory as they fall in the range of values proposed for the C-S-H gel using the nanoindentation tests. This indicates the capabilities of MD simulations in capturing the main elastic properties of cement-based materials at the nano-scale.

In addition to the characterization of elastic properties, the outcome of a separate effort to understand the mechanical response of the HCP phases under uniaxial tensile strains using MD simulations was presented. Except few studies that are only limited to estimate the elastic

properties of the HCP crystals, there are no simulation efforts or experimental studies in the literature to fully characterize the mechanical behavior of this important category of materials. This was the motivation of the present study to evaluate the stress-strain behavior of the HCP crystals under the uniaxial tensile strain. The atomic structures of tobermorite 9, 11 and 14 Å, jennite, hydrogarnet, ettringite, and kuzelite were modeled at the nano-scale and MD simulations were performed to understand the mechanical behavior of the HCP crystalline structures in the *x*, *y*, and *z* directions. It was observed that except for hydrogarnet, the stress-strain behavior of the HCP crystals is substantially dependent on the direction of applied tensile strains. This highlights the existence of strong anisotropy in the mechanical properties of the HCP crystals. Bond analysis was conducted to reveal the correlation between the chemical bond characteristics and the stress-strain curves. It was found that depending on the direction of straining, the breakage of the Ca-O and/or Si-O bonds is responsible for the failure in the tobermorite and jennite structures. Alternatively, the sequential breakage of the Ca-O and Al-O bonds leads to the significant reduction in resistance against tensile strains in hydrogarnet, ettringite, and kuzelite.

A separate structural damage analysis was carried out to identify the failure mechanisms of the HCP crystalline structures under tensile strains. The damaged structures of tobermorite 11 and 14 Å in the *x*, *y*, and *z* directions show two failure modes: breakage of the calcium silicate layers and interlayer segregation. In the *x* and *y* directions, both tobermorite structures demonstrate very similar mechanical behavior. The damage in the mentioned directions mainly results from the breakage of the chemical bonds, which leads to the formation of few large voids. The coalescence of the voids results in the breakage of the calcium silicate layers and failure of the tobermorite structures. In the *z* direction, however, the tobermorite structures show different mechanical response to the applied strain. While the segregation between the calcium clusters is responsible for the failure in tobermorite 11 Å, the interlayer segregation is the main cause of damage to tobermorite 14 Å. For tobermorite 9 Å and jennite, it was found that the breakage of

the calcium silicate layers is the failure mode in the *x* and *y* directions. In the *z* direction, however, the segregation of interlayer calcium polyhedra causes a brittle fracture. In this direction, the presence of water molecules in the interlayer significantly reduced the tensile strength of jennite. Concerning ettringite and kuzelite, the tricalcium aluminate columns in the former and $[Ca_2Al(OH)_6]^+$ layers in the latter mainly contribute to carrying tensile strains. The separation between the tricalcium aluminate columns and the sequential breakage of strong tricalcium aluminate columns is the failure mode of ettringite in the *x*/*y* and *z* directions, respectively. The presence of a weak network of hydrogen bonds in the space between the columns lowers the mechanical strength of ettringite in the *x*/*y* direction. As for kuzelite, the sequential breakage of the Ca-O and Al-O bonds of the $[Ca_2Al(OH)_6]^+$ layers is the main failure mode. The strong coulombic interactions between the SO_4^{2-} groups and the $[Ca_2Al(OH)_6]^+$ layers results in improved mechanical strength in the *z* direction.

Lastly, the mechanical properties, i.e., Young's modulus, Poisson's ratio, and tensile strength, of the HCP were extracted from the stress-strain curves. It was observed that tobermorites and jennite have their largest Young's modulus and ultimate tensile strength in the *y* direction. This is mostly attributed to the presence of strong covalent Si-O bonds running along the *y* direction. On the other hand, kuzelite and ettringite are found stiffest and strongest in the *z* direction. The reason for this situation is the presence of strong tricalcium aluminate columns and $[Ca_2Al(OH)_6]^+$ layers stretched along the *z* direction of ettringite and kuzelite, respectively. Since the algorithm used in this study allowed for the anisotropic relaxation of the directions perpendicular to the direction of straining, the Poisson's effect in the lateral directions was captured. It was shown that the Poisson's ratio of the HCP crystals have a wide range, which indicates the dependency of the results to the direction of applied strains. The outcome of this research provides reliable atomistic models, which are critical to investigate the mechanical behavior of the major constituents of cement-based materials at different scales.

REFERENCES

[1] "Minerals.USGS.gov," United States Geological Survey, 1 June 2007. [Online]. Available: http://minerals.usgs.gov.

[2] E. Sullivan, "Long-term cement consumption outlook, PCA the monitor forecast report," Portland Cement Association, Fall 2013. [Online]. Available: http://www.cement.org.

[3] P. Mehta and D. Manmohan, "Pore size distribution and permeability of hardened cement pastes," in *Proceedings of the seventh international congress on the chemistry of cements*, Paris, 1980.

[4] H. Le Chatelier, Recherches Expérimentales Sur La Constitution Des Mortiers Hydrauliques, 2 ed., Paris: Vve Ch. Dunod, 1904.

[5] K. Fujii and W. Kondo, "Kinetics of the Hydration of Tricalcium Silicate," *Journal of American Ceramic Society,* vol. 57, no. 11, pp. 492-497, 1974.

[6] J. Pommersheim and J. Chang, "Kinetics of hydration of tricalcium aluminate," *Cement and Concrete Research,* vol. 16, no. 3, pp. 403-450, 1986.

[7] V. Peterson, D. Neumann and R. Livingston, "Hydration of cement: The application of quasielastic and inelastic neutron scattering," *Physica B: Condensed Matter,* vol. 1, no. 15, pp. 481-486, 2006.

[8] H. Taylor, Cement Chemistry, 2 ed., London: Thomas Telford Publishing, 1997.

[9] F. Lea and P. Hewlett, Lea's chemistry of cement and concrete, 4 ed., Oxford: Elsevier Butterworth-Heinemann, 1998.

[10] P. Mehta and P. Monteiro, Concrete: Structure, properties, and materials, Englewood Cliffs, N.J.: Prentice Hall, 1993.

[11] H. Taylor, C. Famy and K. Scrivener, "Delayed ettringite formation," *Cement and Concrete Research,* vol. 31, no. 5, pp. 683-693, 2001.

[12] W. Michaelis, The hardening of cement under water, Chicago: Cement and Engineering News, 1909.

[13] T. Powers and T. Brownyard, Studies of the physical properties of hardened Portland cement paste, vol. 22, PCA Bulletin, 1948.

[14] R. Feldman and P. Sereda, "A new model for hydrated Portland cement and its practical implications," *Engineering Journal Canada,* vol. 53, no. 8-9, pp. 53-59, 1970.

[15] H. Jennings, "A model for the microstructure of calcium silicate hydrate in cement paste," *Cement and Concrete Research,* vol. 30, no. 1, pp. 101-116, 2000.

[16] P. Tennis and H. Jennings, "A model for two types of calcium silicate hydrate in the microstructure of Portland cement paste," *Cement and Concrete Research,* vol. 30, no. 6, pp. 855-863, 2000.

[17] H. Jennings, "Refinements to colloidal model of C-S-H in cement: CM-II," *Cement and Concrete Research,* vol. 38, no. 3, pp. 275-289, 2008.

[18] M. Diamon, S. Abo-El-Enein, G. Rosara, S. Goto and R. Kondo, "Pore structure of calcium silicate hydrate in hydrated tricalcium silicate," *Journal of the American Ceramic Society,* vol. 60, no. 3-4, pp. 110-114, 1997.

[19] P. Yu, R. Kirkpatrick, B. Poe, P. McMillan and X. Cong, "Structure of calcium silicate hydrate (C-S-H): Near-, mid-, and far- Infrared Spectroscopy," *Journal of the American Ceramic Society,* vol. 82, no. 3, pp. 742-748, 1999.

[20] A. Allen and J. Thomas, "Analysis of C-S-H gel and cement paste by small-angle neutron scattering," *Cement and Concrete Research,* vol. 37, no. 3, pp. 319-324, 2007.

[21] H. Jennings, J. Thomas, J. Gevrenov, G. Constantinides and F. Ulm, "A multi-technique investigation of the nanoporosity of cement paste," *Cement and Concrete Research,* vol. 73, no. 3, pp. 329-336, 2007.

[22] I. Richardson, "The calcium silicate hydrates," *Cement and Concrete Research,* vol. 38, no. 2, pp. 137-158, 2008.

[23] I. Richardson and G. Groves, "Models for the composition and structure of calcium silicate hydrate (C-S-H) gel in hardened tricalcium silicate pastes," *Cement and Concrete Research,* vol. 22, no. 6, pp. 1001-1010, 1992.

[24] I. Richardson and G. Groves, "The incorporation of minor and trace elements into calcium silicate hydrate (C-S-H) gel in hardened cement pastes," *Cement and Concrete Research,* vol. 23, no. 1, pp. 131-138, 1993.

[25] J. Bernal, J. Jeffery and T. H.F.W., "Crystallographic research on the hydration of Portland cement. A first report on investigation in progress.," *Magazine of Concrete Research ,* vol. 4, no. 11, p. 5, 1952.

[26] H. Kurczyk and H. Schwiete, "Concerning the hydration products of C_3S and β-C_2S," in *Proceedings of the 4th International Symposium on the Chemistry of Cement*, Washington, 1960.

[27] D. Kantro, S. Brunauer and C. Weise, "Developement of surface in the hydration of calcium silicates. II. Extension of investigations to earlier and later stages of hydration," *Journal of Physical Chemistry ,* vol. 66, no. 10, pp. 1804-1809, 1962.

[28] K. Fujii and W. Kondo, "Estimation of thermodynamical data for calcium silicate hydrate (C-S-H)," *Communications of the American Ceramic Society,* vol. 66, no. 12, pp. C220-C221, 1983.

[29] H. Taylor, "Proposed structure for calcium silicate hydrate gel," *Journal of the American Ceramic Society,* vol. 89, no. 6, pp. 464-467, 1986.

[30] I. Richardson, "Tobermorite/jennite- and tobermorite/calcium hydroxide-based models for the structure of C-S-H: applicability to hardened pastes of tricalcium silicate, β-dicalcium silicate, Portland cement, and blends of Portland cement with blast-furnace slag, metakaol," *Cement and Concrete Research,* vol. 34, no. 9, pp. 1733-1777, 2004.

[31] J. Chen, J. Thomas, H. Taylor and H. Jennings, "Solubility and structure of calcium silicate hydrate," *Cement and Concrete Research,* vol. 34, no. 9, pp. 1499-1519, 2004.

[32] S. Merlino, E. Bonaccorsi and T. Armbruster, "Tobermorite: Their real structure and order-disorder (OD) character," *American Mineralogist,* vol. 84, pp. 1613-1621, 1999.

[33] E. Bonaccorsi, S. Merlino and A. Kampf, "The crystal structure of tobermorite 14 Å (Plombierite), a C-S-H phase," *Journal of the American Ceramic Society,* vol. 88, no. 3, pp. 505-512, 2005.

[34] E. Bonaccorsi, S. Merlino and H. Taylor, "The crystal structure of jennite, $Ca_9Si_6O_{18}(OH)_6.8H_2O$," *Cement and Concrete Research,* vol. 34, no. 9, pp. 1481-1488, 2004.

[35] H. Petch, "The hydrogen positions in portlandite, $Ca(OH)_2$, as indicated by the electron distribution," *Acta Crystallographica,* vol. 14, pp. 950-957, 1961.

[36] L. Desgranges, D. Grebille, G. Calvarin, G. Chevrier, N. Floquest and J. Niepce, "Hydrogen thermal motion in calcium hydroxide: Ca(OH)2," *Acta Crystallograpica ,* vol. 49, pp. 812-817, 1993.

[37] A. Moore and H. Taylor, "Crystal structure of ettringite," *Nature,* vol. 218, no. 5146, pp. 1048-1049, 1968.

[38] M. Hartman and R. Berliner, "Investigation of the structure of ettringite by time-of-flight neutron powder diffraction techniques," *Cement and Concrete Research,* vol. 36, no. 2, pp. 364-370, 2006.

[39] R. Allmann, "Refinement of the hybrid layer structure $[Ca_2Al(OH)_6]^+.[1/2SO_4.3H_2O]^-$," *Neus Jahrbuch fur Mineralogie Monatshefte,* vol. 4, pp. 136-144, 1997.

[40] M. Paul and F. Glasser, "Impact of prolonged warm (85˚C) moist cure on Portland cement paste," *Cement and Concrete Research,* vol. 30, no. 12, pp. 1869-1877, 2000.

[41] G. Lager, T. Armbruster and J. Faber, "Neutron and X-ray diffraction of hydrogarnet Ca3Al2(O4H4)3," *American Mineralogist,* vol. 72, pp. 756-765, 1987.

[42] N. Metropolis, A. Rosenbluth, M. Rosenbluth, A. Teller and E. Teller, "Equations of state calculations by fast computing mechanics," *Journal of Chemical Physics ,* vol. 21, no. 6, pp. 1087-1092, 1953.

[43] B. Alder and T. Wainwright, "Studies in Molecular Dynamics. I. General Method," *Journal of Chemical Physics,* vol. 31, no. 2, p. 459, 1959.

[44] A. Rahman, "Correlations in the Motion of Atoms in Liquid Argon," *Physical Review Letters,* vol. 136, no. 2A, pp. 405-411, 1964.

[45] R. Tolman, The Principles of Statistical Mechanics, New York: Dover Publications, 1938.

[46] T. Hill, An introduction to statistical thermodynamics, New York: Dover Publications, 1960.

[47] M. Buehler, Atomistic modeling of materials failure, New York: Springer, 2008.

[48] W. Hastings, "Monte Carlo Sampling Methods Using Markov Chains and Their Applications," *Biometrika,* vol. 57, no. 1, pp. 97-109, 1970.

[49] H. Sun, "COMPASS: An ab initio force-field optimized for condensed-phase applications-overview with details on alkane and benzene compounds," *The Journal of Physical Chemistry B,* vol. 102, no. 38, pp. 7338-7364, 1998.

[50] A. Rappe, C. Casewit, K. Colwell, W. Goddard and W. Skiff, "UFF, A Full Periodic Table Force Field for Molecular Mechanics and Molecular Dynamics Simula-tions," *Journal of American Chemical Society,* vol. 114, no. 25, pp. 1024-1003, 1992.

[51] S. Mayo, B. Olafson and W. Goddard III, "Dreiding: A generic force field for molecular simulations," *Journal of Physical chemistry ,* vol. 94, pp. 8897-8909, 1990.

[52] R. Cygan, J. Liang and A. Kalinichev, "Molecular models of hydroxide, oxyhydroxide, and clay phases and developement of a general force field," *The Journal of Physical Chemistry B,* vol. 108, no. 4, pp. 1255-1266, 2004.

[53] L. Verlet, "Computer "Experiments" on Classical Fluids. I. Thermodynamical Properties of Lennard−Jones Molecules," *Physical Review 159,* vol. 159, p. 98–103, 1967.

[54] D. Theodorou and U. Suter, "Atomistic modeling of mechanical properties of polymeric glasses," *Macromolecules,* vol. 19, no. 1, pp. 139-154, 1986.

[55] W. Kreher and A. Molinari, "Residual stresses in polycrystals as influenced by grain shape and texture," *Journal of Mechanics and Physics of Solids,* vol. 41, pp. 1955-1977, 1993.

[56] W. Voigt, Lehrbuch der kristallphysic, Leibzig: Teubner, 1928.

[57] A. Reuss, "Berechnung der Fließgrenze von Mischkristallen auf Grund der Plastizitätsbedingung für Einkristalle, ZAMM," *Journal of Applied Mathematics and Mechanics / Zeitschrift für Angewandte Mathematik und Mechanik,* vol. 9, no. 1, pp. 49-58, 1929.

[58] T. Hill, "The elastic behavior of crystalline aggregate," in *Proceedings of the Physical Society, Section A, 65: 337-347.* , London, 1952.

[59] M. Allen and D. Tildesley, Computer simulation of liquids, New York: Oxford University Press, 1987.

[60] J. Laugesen, "Density functional calculations of elastic properties of portlandite, $Ca(OH)_2$," *Cement and Concrete Research,* vol. 35, no. 2, pp. 199-202, 2005.

[61] H. Manzano, J. Dolado and A. Ayuela, "Elastic properties of the main species present in Portland cement pastes," *Acta Materialia,* vol. 57, no. 4, pp. 1666-1674, 2009.

[62] F. Holuj, M. Drozdowski and M. Czajkowski, "Brillouin spectrum of $Ca(OH)_2$," *Solid State Communications,* vol. 56, no. 12, pp. 1019-1021, 1985.

[63] S. Speziale, H. Richmann, F. Schilling, H. Wenk and P. Monteiro, "Determination of the elastic constants of portlandite by Brillouin spectroscopy," *Cement and Concrete Research,* vol. 38, no. 10, pp. 1148-1153, 2008.

[64] C. Meade and R. Jeanloz, "Static compression of $Ca(OH)_2$ at room temperature:observation of amorphization and equation of state measurements to 10.7 GPa," *Geophysical Research Letters,* vol. 17, no. 8, pp. 1157-1160, 1990.

[65] J. Beaudoin, "Comparison of mechanical properties of compacted calcium hydroxide and portland cement pastes systems," *Cement and Concrete Research,* vol. 13, no. 3, pp. 319-324, 1983.

[66] F. Wittmann, "Estimation of the modulus of elasticity of Calcium Hydroxide," *Cement and Concrete Research,* vol. 16, no. 6, pp. 971-972, 1986.

[67] P. Monteiro and C. Chang, "The elastic moduli of calcium hydroxide," *Cement and Concrete Research,* vol. 25, no. 8, pp. 1605-1609, 1995.

[68] H. Manzano, Atomistic simulation studies of the cement paste components, Guipúzcoa, Spain: PhD thesis, Universidad del Pais Vasco, 2009.

[69] R. Shahsavari, M. Buehler, R. Pellenq and F. Ulm, "First-principle study of elastic constants and interlayer interactions of complex hydrated oxides: Case study of tobermorite and jennite," *Journal of American Ceramic Society ,* vol. 92, no. 10, pp. 2323-2330, 2009.

[70] C. Dharmawardhana, A. Misra, S. Aryal, P. Rulis and W. Ching, "Role of interatomic bonding in the mechanical anisotropy and interlayer cohesion of CSH crystals," *Cement and Concrete Research,* vol. 52, pp. 123-130, 2013.

[71] R. Pellenq, N. Lequeux and H. van Damme, "Engineering the bonding scheme in C-S-H: The iono-covalent framework," *Cement and Concrete Research,* vol. 38, pp. 159-174, 2008.

[72] J. Oh, S. Clark, H. Wenk and P. Monteiro, "Experimental determination of bulk modulus of 14 Å tobermorite using high pressure synchrotron X-ray diffraction," *Cement and Concrete Research,* vol. 44, no. 2, pp. 397-403 , 2012.

[73] S. Speziale, F. Jiang, Z. Mao, P. Monteiro, H. Wenk, T. Duffy and F. Schilling, "Single-crystal elastic constants of natural ettringite," *Cement and Concrete Research,* vol. 38, no. 7, pp. 885-889, 2008.

[74] C. Haecker, E. Garboczi, J. Bullard, R. Bohn, Z. Sun, S. Shah and T. Voigt, "Modeling of linear elastic properties of Portland cement paste," *Cement and Concrete Research,* vol. 35, no. 10, pp. 1948-1960, 2005.

[75] A. Hershey, "The elasticity of an isotropic aggregate of anisotropic cubic crystals," *Journal of Applied Mechanics,* vol. 21, pp. 236-240, 1954.

[76] E. Kröner, "Statistical continuum mechanics," CISM courses and letters, Springer-Verlag. , 1972.

[77] T. Hill, "A self-consistent mechanics of composite materials," *Journal of the Mechanics and Physics of Solids,* vol. 13, no. 4, pp. 213-222, 1965.

[78] T. Mori and K. Tanaka, "Average stress in matrix and average elastic energy of materials with misfitting inclusions," *Acta Metallurgica,* vol. 21, no. 5, pp. 571-574, 1973.

[79] Y. Benvensite, "A new approach to the application of Mori-Tanaka's theory in composite materials," *Mechanics of Materials,* vol. 6, no. 2, pp. 147-157, 1987.

[80] M. Vandamme, F. Ulm and P. Fonollosa, "Nanogranular packing of C-S-H at substochiometric conditions," *Cement and Concrete Research,* vol. 40, no. 1, pp. 14-26, 2010.

[81] G. Constantinides and F. Ulm, "The nanogranular nature of C-S-H," *Journal of the Mechanics and Physics of Solids,* vol. 55, no. 1, pp. 64-90, 2007.

[82] J. Hughes and P. Trtik, "Micro-mechanical properties of cement paste measured by depth-sensing nano-indentation: a preliminary correlation of physical properties with phase type," *Materials Characterization,* vol. 53, no. 2-4, pp. 223-231, 2004.

[83] G. Constantinides and F. Ulm, "The effect of two types of C-S-H on the elasticity of cement-based materials: results from nanoindentation and micromechanical modeling," *Cement and Concrete Research,* vol. 34, no. 1, pp. 67-80, 2004.

[84] W. Zhu, J. Hughes, N. Bicanic and C. Pearce, "Nanoindentation mapping of mechanical properties of cement paste and natural rocks," *Materials Characterization,* vol. 58, no. 11-12, pp. 1189-1198, 2007.

[85] P. Mondal, S. Shah and L. Marks, "A reliable technique to determine the local mechanical properties at the nanoscale for cementitious materials," *Cement and Concrete Research,* vol. 37, no. 10, pp. 1440-1444, 2007.

[86] P. Acker, "Micromechanical analysis of creep and shrinkage mechanisms," in *Procedeeings of Creep, shrinkage and durability mechanics of concrete and other quasi-brittle materials*, London, 2001.

[87] J. Thomas and H. Jennings, "A colloidal interpretation of chemical aging of the C-S-H gel and its effects on the properties of cement paste," *Cement and Concrete Research,* vol. 36, no. 1, pp. 30-38, 2006.

[88] M. Vandamme and F. Ulm, "Nanogranular origin of concrete creep," in *Proceedings of National Academy of Sciences of the United States of America*, 2009.

[89] A. Gouldstone, N. Chollacoop, M. Dao, J. Li, A. Minor and Y. Shen, "Indentation across size scales and disciplines: Recent developments in experimentation and modeling," *Acta Materialia ,* vol. 55, pp. 4015-4039, 2007.

[90] J. Schiøtz, F. Di Tolla and K. Jacobsen, "Softening of nanocrystalline metals at very small grain sizes," *Letters to Nature,* vol. 391, pp. 561-563, 1998.

[91] M. Horstemeyer, M. Baskes, A. Godfrey and D. Hughes, "A large deformation atomistic study examining crystal orientation effects on the stress–strain relationship," *International Journal of Plasticity,* vol. 18, no. 2, pp. 203-229, 2002.

[92] S. Ogata, F. Shimizu, J. Li, M. Wakeda and Y. Shibutani, "Atomistic simulation of shear localization in Cu–Zr bulk metallic glass," *Intermetallics,* vol. 14, no. 8-9, pp. 1033-1037, 2006.

[93] A. Pedone, G. Malavasi, M. Menziani, U. Segre and A. Cormack, "Molecular Dynamics Studies of Stress-Strain Behavior of Silica Glass under a Tensile Load," *Chemistry of Materials,* vol. 20, no. 13, pp. 4356-4366, 2008.

[94] W. Ching, P. Rulis and A. Misra, "Ab initio elastic properties and tensile strength of crystalline hydroxyapatite," *Acta Biomaterialia,* vol. 5, no. 8, pp. 3067-3075, 2009.

[95] A. Misra and W. Ching, "Theoretical nonlinear response of complex single crystal under multi-axial tensile loading," *Scientific Reports,* vol. 3, 2013.

[96] X. Wu, R. Moon and A. Martini, "Tensile strength of Iβ crystalline cellulose predicted by molecular dynamics simulation," *Cellulose,* vol. 21, no. 4, pp. 2233-2245, 2014.

[97] T. Belytschko, S. P. Xiao, G. C. Schatz and R. S. Ruoff, "Atomistic simulations of nanotube fracture," *Physical Review B,* vol. 65, no. 23, 2002.

[98] S. Zhang, S. Mielke, R. Khare, D. Troya, R. Ruoff, G. Schatz and T. Belytschko, "Mechanics of defects in carbon nanotubes: Atomistic and multiscale simulations," *Physical Review B,* vol. 71, no. 11, 2005.

[99] L. Liu, A. Jaramillo-Botero, W. Goddard III and H. Sun, "Development of a ReaxFF Reactive Force Field for Ettringite and Study of its Mechanical Failure Modes from Reactive Dynamics Simulations," *The Journal of Physical Chemistry A,* vol. 116, no. 15, pp. 3918-3925, 2012.

[100] H. Manzano, E. Masoero, I. Lopez-Arbeloa and H. Jennings, "Shear deformations in calcium silicate hydrates," *Soft Matter,* vol. 9, no. 30, pp. 7333-7341, 2013.

[101] J. Stowe, P. Predecki, P. Laz, B. Burks and M. Kumosa, "Probabilistic molecular dynamics evaluation of the stress-strain behavior of polyethylene," *Acta Materialia ,* vol. 57, no. 12, pp. 3615-3622, 2009.

[102] S. Plimpton, "Fast parallel algorithms for short-range molecular dynamics," *Journal of Computational Physics ,* vol. 117, no. 1, pp. 1-19, 1995.

[103] A. Stukowski, "Visualization and analyis of atomistic simulation data with OVITO-the open visualization tool," *Modeling and Simulation in Materials Science and Engineering,* vol. 18, p. 015012, 2010.

[104] A. Stukowski, "Computational analysis methods in atomistic modeling of crystals," *The Minerals, Metals and Materials Society,* vol. 66, no. 3, pp. 399-407, 2013.

[105] S. Hajilar and B. Shafei, "Molecular dynamics simulation of elastic properties of tobermorite family," in *The 4th RILEM International Symposium on Concrete Modeling*, Beijing, China, 2014.

[106] S. Hajilar and B. Shafei, "Nano-scale characterization of elastic properties of AFt and AFm phases of hydrated cement paste," in *Computational Modeling of Concrete Structures*, St. Anton am Arlberg, Austria, 2014.

[107] S. Hajilar and B. Shafei, "Nano-scale investigation of elastic properties of hydrated cement paste constituents using molecular dynamics simulations," *Computational Materials Science,* DOI: 10.1016/j.commatsci.2014.12.006, 2015.